Radio Wave Diffraction and Scattering Models For Wireless Channel Simulation

by

Mark D. Casciato

A dissertation submitted in partial fulfillment
of the requirements for the degree of
Doctor of Philosophy
(Electrical Engineering)
in The University of Michigan
2001

Doctoral Committee:

Associate Professor Kamal Sarabandi, Chair
Associate Professor Brian Gilchrist
Professor Linda P.B. Katehi
Professor Thomas B.A. Senior
Professor Wayne E. Stark

ACKNOWLEDGEMENTS

First I would like to acknowledge my parents, Rose and Dan Casciato for their support throughout these last 5 years, without which attending graduate school would have been much more difficult. I would also like to acknowledge all of my committee members, but most especially my thesis advisor, Professor Kamal Sarabandi for his guidance and mentorship, both academically and personally. I would also like to thank Professor Thomas Senior for the interesting and enlightening discussions on diffraction theory. The students and colleagues at the University of Michigan Radiation Laboratory, where to begin. I would like to thank and acknowledge all of the students, faculty, and staff for your help and support over my stay here at Michigan, I consider all of you good friends. I would most especially like to thank my very close friends here, Stéphane Legault, Lee Harle, J.D. Shumpert, Dejan Filipovich, Olgica Milenkovic, Leland Pierce, Katherine Herrick, Mark Fischman, Dan Lawrence, Sergio Pacheco, Dimitris Peroulis, Ron Reano, Helena Chan, Mohamed Abdelmoneum, and of course Bettina Köthner for all the good company. I apologize in advance for anyone that I may have missed. Finally I would like to thank the Army Research Office for their support, without which this project would not have been possible (contract DAAH04-96-1-037).

TABLE OF CONTENTS

LIST OF TABLES

LIST OF FIGURES

LIST OF APPENDICES

Appendix

CHAPTER 1

Introduction

The propagation of a radio wave through some physical environment is effected by various mechanisms which affect the fidelity of the received signal. Accurate prediction of these effects is essential in the design and development of a communications system. These effects can include shadowing and diffraction caused by obstacles along the propagation path, such as hills or mountains in a rural area, or buildings in a more urban environment. Reflections off obstacles or the ground cause multi-path effects and the radio signal can be significantly attenuated by various environmental factors such as ionospheric effects, propagation through vegetation, such as in a forest environment, or reflection from an impedance transition such as a river or land/sea interface. When line-of-sight (LOS) propagation is not present these environmental mechanisms have the dominate effect on the fidelity of the received signal through dispersive effects, fading, and signal attenuation.

Accurate prediction of these propagation effects allow the communications system engineer to address the trade-off between radiated power and signal processing by developing an optimum system configuration in terms of modulation schemes, coding, frequency band and bandwidth, antenna design, and power. Current techniques commonly applied to characterizing the communications channel are highly heuristic in nature and not generally applicable. It is the intent of this work to define a methodology for the accurate and general prediction of radio wave propagation by application of electromagnetic wave theory, and

within this framework to develop electromagnetic models of canonical geometries which represent various scattering and diffraction mechanisms in the propagation environment. The scope of the problem should not be underestimated and once a basic methodology is defined initial research must be narrowed to a specific region of investigation, i.e., frequency band, domain type (rural, urban, satellite-based, ground-based, etc). These initial electromagnetic models can then be built upon as a bases for expansion of the overall model to include a wider range of propagation scenarios.

In the sections that follow the previous discussion will be expanded upon. The motivation behind this work is first discussed. Next the research approach is detailed, with a basic methodology for the prediction of radio wave propagation defined. The specific focus of this thesis within the broader scope of the propagation problem is then given, including a description of two canonical diffraction models developed. The next section contains relevant conventions, definitions and assumptions, used throughout this thesis, followed by a brief introduction and outline of the chapters that follow.

1.1 Motivation

The basic motivating factor behind this work is the need for development of an accurate and general propagation model. As mentioned previously the ability to accurately predict the effects of the propagation environment on a communications channel is essential in the development and optimal design of a communications system. Current methods of channel characterization, while having the advantage of simplicity, do not adequately address the issue and there is a need for significant improvement in the prediction of radio wave propagation. Commonly used methods of channel characterization can be broken down into two areas, empirical models, which are highly heuristic in nature, and simplified analytic models. The empirical models are constructed from measured data and are not directly connected to the physical processes involved. This limits them to very specific environ-

mental conditions at the time the measurements were made as well as measurement system attributes (band, bandwidth, and polarization). An example of a commonly used empirical model for urban environments is the Okumura model [2]. This model uses simple algebraic equations to calculate mean path-loss for fixed frequency, observation distance, and transmitter/receiver height. It does not account for coherence bandwidth, fading, or depolarization effects. In addition it fails if the antenna heights or orientations are changed. Analytic models, while attempting to account for the interaction of the various mechanisms which effect propagation, are simplified to a degree as to make them invalid for most practical applications. An example of this is the Longley-Rice irregular terrain model [3]. It uses Geometrical Optics (GO) and ray-tracing to account for reflected fields and knife-edge or Kirchhoff diffraction to account for path obstacles. The GO approximation does not account for shadowing and the knife-edge approximation is invalid in the transition region between light and shadow and in the shadow region.

Due to the discussed shortcomings in existing methods of propagation prediction a more rigorous approach, based on the application of electromagnetic wave theory, must be applied to the problem at hand. The approach to be defined is directly connected to the physical processes at work in the propagation environment and will result in propagation models which are both accurate and more generally applicable.

1.2   Research Approach

As stated the prediction of radio wave propagation for general environments and in an accurate manner is a complex problem with many avenues of research to pursue. In this section a general approach or methodology for developing a complete propagation model is defined. Within this framework the canonical models developed in this thesis are described.

1.2.1 Methodology

The development of a more accurate and general model to predict radio wave propagation requires that a basic methodology or approach to the problem be defined. The flowchart in Figure 1.1 outlines this basic approach. Referring to Figure 1.1, the problem is first defined in terms of regions or domains, each of which have their own unique environmental characteristics, thus requiring a somewhat different (although sometimes overlapping) approach to solving the subsequent electromagnetic problem. These regions can be defined in terms of urban/rural domains or ground-based/satellite-based scenarios. The basic methodology within these domains is to develop a set of canonical diffraction and scattering models which represent various environmental features. These models are developed using the technique most appropriate for the given electromagnetic problem, i.e., analytic, numeric or some type of hybrid technique. Approximations are made which allow for efficient application of the model, while retaining the accuracy required. The individual models are then merged into a complete propagation scenario. Monte Carlo simulation accounts for the statistical nature of the propagation channel. Eventually remote sensing information obtained from available databases can be used to define the propagation environment. The complete model will allow for a simulation which is directly based on the physical environment and therefore accurate and generally applicable.

1.2.2 Initial Concentration

Having defined the basic methodology to developing an overall propagation model an area of concentration is now defined for this initial research. In this work the investigation is focused on the rural domain or environment and ground-based (point to point) or ground to/from unmanned aerial vehicle (UAV) communication at frequencies from HF through L-Band. Figure 1.2 shows a typical propagation environment in a rural area. The radio wave can be diffracted by obstacles such as hills, or mountains or an impedance transition

Hybrid Analytical/Numerical Diffraction Models RepresentingVarious Rural, Urban & Atmospheric Features

Analytical Models, Canonical Shapes Only

Numerical Solutions, Computationally Intensive

Physics Based Approximations, Improve Computational Efficiency, Retain Accuracy

Integrate Diffraction Models to Predict Relevant Interactions

Satellite Geographical / Environmental Database

Geographical Database

Environmental Features and Statistics, Rural, Urban and Atmospheric

Incorporate into Physical Model of Propagation Environment for EM Simulation

Merge Environmental Model and Integrated Diffraction Model into Accurate EM Propagation Model

Accurate Mean-field, Coherency, Variance, Polarization Effects, Multi-path & Dispersion (Delay) Effects

Figure 1.1: Flowchart - Physics-based Methodology

such as a river or land/sea interface. Along the propagation path the signal may be perturbed by a highly scattering medium such as a forest. In this work two diffraction models are developed, based on canonical geometries, and applicable to a rural environment, for eventual integration into the overall propagation model. The first represents the effects of a flat earth on the radio signal, which can contain a one-dimensional impedance variation, representative of a river or land/sea interface. The second calculates the effects on the radio signal of singly curved, convex obstacles with a large, slowly varying radius of curvature, and which can represent terrain features such as hills or mountains.
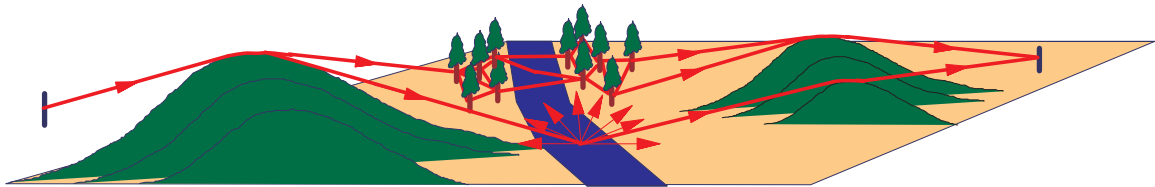
Figure 1.2: Rural Terrain Scenario

1.3   Relevant Assumptions & Definitions

In this section relevant assumptions, definitions, and conventions are given. Unless otherwise indicated they are valid throughout the thesis.

The time convention $e^{-i\omega t}$ is assumed throughout this thesis and suppressed.

It is assumed throughout that the effects of the Earth can be modeled as a highly conductive, non-magnetic impedance surface ($\varepsilon_r \to \infty$, $\mu_r = 1$), which is essentially impenetrable and the Standard Impedance Boundary Condition (SIBC), namely, $(\hat{n} \times \hat{n} \times \mathbf{E}) = -Z(\hat{n} \times \mathbf{H})$, with Z being the impedance of the Earth, is applied throughout. This assumption is valid for a lossy Earth where the penetration depth, d, is small ($d \ll \lambda$), and is applicable at the frequencies of interest in this work. Interested readers are referred to [4] for a discussion on the SIBC as well as techniques to improve on the accuracy of this assumption.

As the intent is to represent a lossy Earth in a realistic fashion, impedance values are chosen which are representative of moist earth, or in the case of propagation over water, saline water. The impedance values of the soil are derived from the values of permittivity and conductivity given by Hipp [1] for San Antonio Gray Loam with a density of $1.4\, g/cm^3$ and a varying moisture content (given as percent moisture in terms of gravimetric moisture content). The impedance values of the water are derived from the equations for complex permittivity given by Ulaby, et al., for saline water, with a salt content defined as as parts per 1000 on a weight basis (pp/1000) [5]. Table 1.1 shows the complex permittivity and conductivity calculated from the tables in [1] for San Antonio gray loam with moisture content varying from 0 to 20%. Many of the examples to be shown are in the HF to VHF frequency range, and as the permittivity and conductivity values in Table 1.1 are essentially unvarying over this range the values given are assumed to be constant across this frequency band.

It should also be noted that all simulation results provided in this thesis were run on a Sun Microsystems Ultra2, with a 300MHz Sun microprocessor.

Table 1.1: Soil parameters for San Antonio gray loam with a density of 1.4 g/cm^3, for varying gravimetric moisture content at 30MHz (from Hipp [1]).

% Moisture	ε'_r	σ
0.0	3.5	$\ll 10^{-4}$
2.5	5.8	5.0×10^{-3}
5.0	8.2	1.0×10^{-2}
10.0	14.0	5.0×10^{-2}
20.0	24.0	8.0×10^{-2}

1.4   Chapter Outline & Introduction

In the chapters that follow the development of the aforementioned diffraction models along with relevant results and applications are presented. Each of these models represents an independent electromagnetic problem and therefore each chapter, or a group of chapters for each model is somewhat self-contained. The basic format is as follows. Each chapter will contain brief paragraphs at the beginning and end to maintain a continuity or flow from chapter to chapter. Each chapter will begin with an introductory section. This section will include a detailed history and background of the problem at hand, the most current techniques being applied, and the motivation for further research into improving on these, or developing new techniques. Following this introduction will be a section containing the specifics of the diffraction model being developed, including formulations and appropriate derivations. A section containing validation and results follows. The final section in each chapter will summarize the chapter and draw conclusions.

A problem of significant interest is the propagation of radio waves over a lossy Earth. The surface of the Earth can be modeled locally as a flat, impedance half-space which can also contain some type of transition in the surface impedance such as caused by a river or seashore. In Chapters 2 and 3 a diffraction model for an impedance half-space, with one-dimensional impedance variation, when excited by an infinitesimal dipole, is developed. In Chapter 2 the effects of the homogeneous surface, without the transition is accounted for.

This is a form of the classic Sommerfeld problem of the fields of an infinitesimal dipole radiating above an lossy half-space. Resulting field expressions contain Sommerfeld type integrals, which are highly oscillatory, and difficult to evaluate numerically. In Chapter 2 a method is developed to transform the Sommerfeld integrals into a form more conducive to numerical evaluation, while retaining the rigor of the original expressions. Beginning with an alternate spectral domain representation of the dipole fields, an integral transform technique known as exact image theory is applied. Resulting field expressions are exact, and contain integrands which converge extremely rapidly, up to several orders of magnitude faster than the original Sommerfeld expressions. To complete the model for propagation above an impedance half-space, Chapter 3 addresses the effect of an impedance transition in the surface. Current methods such as the Geometrical Theory of Diffraction (GTD) can only account for the effect of an abrupt discontinuity in the surface impedance. In Chapter 3 a method is developed which is valid for any arbitrary one dimensional impedance transition in the surface, provided the Fourier transform of the surface impedance function is known. By application of a perturbation technique, an integral equation is solved for unknown surface currents. Resulting expressions for the surface currents are recursive in orders of perturbation in terms of multi-fold convolution. Far-field expressions are algebraic to first order. Also in Chapter 3 the combined effects of both the homogeneous surface and the impedance transition are analyzed. Analysis of a land/sea transition shows that the effects of the transition on the total fields is significant when both source and observation are near the surface and insensitive to the gradient of the transition.

Another problem of significant interest is that of the propagation of radio waves over convex obstacles encountered in the propagation environment such as hills, mountains, or ridgelines. Current methods applied to this problem include Kirchhoff (knife-edge) diffraction, whose shortcomings have already been discussed, and GTD methods for both wedge and convex surfaces. Solutions for wedge diffraction require a local radius of curvature smaller than 1/100 of a wavelength which does not occur in nature, even at HF frequencies.

GTD methods for convex surfaces tend to be mathematically and numerically cumbersome and no one GTD method is valid in all regions around the surface (near-field, far-field, deep shadow, deep lit, transition regions between light and shadow). In Chapters 4 and 5 a model is developed which calculates the scattering and diffraction from a singly-curved convex surface, with large slowly varying radius of curvature. The initial model is developed for a perfect electric conducting (PEC) surface and determines induced surface currents in a highly accurate fashion. Unlike GTD techniques for convex surfaces the technique requires no numerical integration or complex mathematical analysis to determine these currents. For a convex surface with large, slowly varying radius of curvature, the induced surface currents can be approximated locally by those of a circular cylinder and the solution of this canonical problem is the first step in developing a model of the induced surface currents on a general convex surface. In Chapter 4, a macromodel for the induced surface currents on a circular PEC cylinder, when excited by a plane wave at oblique incidence, is first developed. This macromodel of the surface currents is based on the definitions of the Physical Theory of Diffraction (PTD) [6] in which the total surface currents are decomposed into a uniform, or physical optics (PO) component and a non-uniform or diffraction component, which is a correction to the PO solution. Application of this macromodel produces highly accurate surface currents for cylinders of any radius above one wavelength. This current is generated by a simple scaling and interpolation of the exact currents on a reference cylinder of moderate radius. In Chapter 5, the method is extended to general, singly-curved, convex surfaces using existing methods found in the literature. The model is first applied to an elliptical cylinder and compared with results from a Method of Moments (MoM) numerical code. The model is then applied to a parabolic surface and results are compared to those generated by applying Kirchhoff (knife-edge) diffraction techniques.

In Chapter 6 this thesis work is summarized and conclusions drawn as well as suggestions for future work.

CHAPTER 2

Fields of an Infinitesimal Dipole Above an Impedance Surface: Effect of the Homogeneous Surface

In this chapter and the next the effects of a lossy earth on the fields of an infinitesimal dipole are examined. These effects can be modeled locally as a flat, planar, impedance surface and the surface can contain an impedance transition such as a river or sea/land interface. The problem can be decomposed into the effect of the homogeneous surface and the effect caused by some impedance transition in the surface such as would be caused by a river, sea/land interface, or swamp/dry land transition. In this chapter the effect of the homogeneous surface on the dipole fields is first discussed, with the effect of the impedance transition as well as the combined effect of the homogeneous surface and impedance transition analyzed in the next. In order to avoid confusion, in the next two chapters the following terminologies are adopted: The effect of the homogeneous surface on the total dipole fields will be referred to as the diffracted fields, while the effect of the impedance transition is defined as the scattered fields.

Calculation of the fields of an infinitesimal dipole radiating above a homogeneous impedance half-space is a form of the classic Sommerfeld problem of calculating the fields of an infinitesimal dipole above a lossy half-space. A solution to this problem was first formulated by Arnold Sommerfeld in 1909 [7] and the resulting expressions for the tra-

ditional solution consist of integrals of the Sommerfeld type which cannot be evaluated in closed form and due to their highly oscillatory nature are difficult to evaluate numerically. A form of these integrals is thus sought, which retains the rigor and generality of the original formulation, while making them more conducive to numerical computation. By application of an integral transform method known as exact image theory explicit expressions are derived for a dipole of arbitrary orientation, above an impedance surface. A spectral domain representation of the dipole fields, of a form not previously seen in the literature, is first given. To apply exact image theory the reflection coefficients of the spectral domain representation are cast in the form of the Laplace transform of an exponential function. By exchanging the order of integration, the spectral domain integration is performed analytically and field expressions are obtained which consist of rapidly converging integrals in the Laplace domain. As no approximations are made, these expressions are exact, and valid for any arbitrary source alignment or observation position. It is shown that the formulation for a horizontal dipole contains an image in the conjugate complex plane resulting in a diverging exponential term not previously discussed in the literature. Comparison of numerical results from exact image theory and the original Sommerfeld type expressions shows good agreement as well as a speed-up in computation time of several orders of magnitude, which depends on the distance between the transmitter and the receiver. This formulation can effectively replace the approximate asymptotic expressions used for predicting wave propagation over a smooth planar ground (having different regions of validity) and in conjunction with the techniques of Chapter 3 (diffraction from an impedance surface with one-dimensional impedance transition) provides a complete methodology for the analysis of radio wave propagation over a smooth planar ground which can contain a general, one-dimensional impedance transition.

2.1 Introduction: The Sommerfeld Problem

The problem of a infinitesimal electric dipole radiating above a lossy half-space was originally formulated by Arnold Sommerfeld in his classic work published in 1909 [7]. Since then it is an understatement to say that this problem has received a significant amount of attention in the literature, with literally hundreds of papers published on the subject. The inclusion of a sign error in the original work prompted much debate, over several decades, on the existence of a Zenneck type surface wave and its significance in the fields generated by a vertical electric dipole. The complete history of the problem is beyond the scope of this thesis, but suffice to say that independent derivations by Weyl [8], Sommerfeld [9], van der Pol and Niessen, [10] and Wise [11] confirmed the sign error, although Sommerfeld himself never admitted to any error in the original 1909 work. The corrected formulation confirmed the existence of a surface wave for certain values of impedance and observation angles, but showed its contribution to the total field only significant within a certain range of distances, dependent on the impedance of the half-space (Sommerfeld numerical distance). Readers are referred to the work of Norton [12, 13] for a concise formulation of the problem, with correct sign, and Baños [14] for a complete perspective of the historical development of the mathematics of the problem.

The Sommerfeld solution is expressed in terms of integrals which cannot be evaluated in closed form and due to their highly oscillatory nature are difficult to evaluate numerically. Numerous techniques, both analytic and numeric, have been applied to evaluate the Sommerfeld integrals in an approximate fashion. To evaluate the Sommerfeld integrals analytically standard asymptotic techniques, such as the method of steepest descent (Saddle Point method), are typically applied [15, 16]. These techniques are valid when distance between source and observation is large and contributions from poles (surface wave) and branch cuts (lateral wave) must be accounted for when deforming the contour. For source and observation near the surface the direct and reflected waves (geometrical optics (GO) term, first order Saddle point) tend to cancel and higher order terms in the asymptotic ex-

pansion are dominate. Norton interpreted this effect as a type of surface wave and thus these higher order terms are typically referred to in the literature as a Norton Surface Wave [12, 13]. For a highly lossy surface (small normalized impedance) the pole approaches the saddle point and their contributions cannot be separated. In this case standard saddle point techniques cannot be applied and an alternate asymptotic technique is necessary [15, 16]. To evaluate the Sommerfeld type integrals numerically, in an approximate fashion, several techniques have been proposed. Parhami *et. al* [17] proposed a method, valid for a vertical electric dipole, in which the integration contour is deformed to the steepest descent path. The integral is then solved asymptotically when distance between image and observation is large, and numerically when this distance is small. Again poles and branch cuts must be accounted for when the contour deformation encounters them and the technique requires evaluation of Hankel functions of complex argument. Michalski [18] improved on this method by proposing a variation in the way a branch cut is handled. Johnson and Dudley [19] proposed a method, valid for small distances between image and observation, in which an analytic technique is applied to reduce the oscillatory nature of the Sommerfeld integrand. While these techniques improve the convergence properties of the Sommerfeld type integrals they require transformations which increase the complexity of the formulation and, as in the case of the asymptotic solutions, are not valid for all source and observation positions, and electrical parameters.

As none of these analytical/numerical techniques are valid for general source orientation and observation location, or arbitrary impedance values, a solution is sought which transforms the Sommerfeld type expressions into a form which retains the rigor and generality of the original formulation, while improving the computational efficiency to a degree which makes evaluation of the resulting exact expressions practical from a numerical standpoint. In order to improve the convergence properties of the Sommerfeld type integrals, an integral transform technique known as exact image theory is applied. In this method an integral transform, in the form of the Laplace transform of an exponential function, is applied

to the reflection coefficients of the Sommerfeld type integrals, resulting in expressions now consisting of a double integral, one in the original spectral domain and one in the Laplace domain. Application of appropriate identities allows for analytical evaluation of the integral in the spectral domain and the remaining integral expressions in the Laplace domain are dominated by a rapidly decaying exponential. These integral expressions are exact, with no approximations made and the decaying exponential in the integrand results in significantly improved convergence properties over the original formulation. The form of these integral expressions can be interpreted as a distributed line source, located at the image point of the dipole source, and extending into the complex plane.

Evaluating the Sommerfeld expressions as a type of distributed image was first proposed by Booker and Clemmow [20]. They recognized that the first order term in the asymptotic expansion of the field expressions in the upper half-space for a vertical dipole was equivalent to straight edge (Kirchhoff) diffraction around a half-screen, if the screen extended from the physical image point, vertically to infinity (in the upper half-space). The field distribution in the lower half-space was in the form of a Fresnel type integral and could be interpreted as a distributed line source beginning at the same physical image point and extending to infinity in the lower half space. Representation of the reflection coefficients in the Sommerfeld formulation in terms of the Laplace transform of an exponential function, for a vertical electric dipole, was apparently first introduced by van der Pol [21] and can also be seen in the work of Norton and Furutsu [13, 22]. Their intent in applying this type of integral transformation was to simplify the asymptotic evaluation of the Sommerfeld formulation by modifying the integrand into a more well behaved form. Interpretation of this modified form of the integrand, for a vertical electric dipole, as a distributed image source located in the complex plane was apparently first proposed by Felsen and Marcuvitz [15], who recognized the improved convergence properties of the integrand for numerical computation. Lindell and Alanen extended the technique to that of electric and magnetic dipoles of arbitrary orientation radiating above a dielectric half-space [23, 24, 25]. For the

dielectric case there is no exact transform for the reflection coefficient and the formulation by Lindell and Alanen for the vertical electric dipole involves a decomposition of the kernel function of the Laplace transform. For the case of a horizontal electric dipole only a formal solution is presented, with no explicit expressions or detailed interpretation of image behavior. This might have been due to the fact that for a general half-space dielectric medium exact analytical expressions for the image currents do not exist. However, such expressions can be obtained for impedance surfaces and the behavior of the image currents for arbitrary dipole orientation can be studied.

In this chapter exact image theory is applied to the problem of an electric dipole, of arbitrary orientation, radiating above an impedance half-space. In Section 2.2 a spectral domain representation of a form not previously seen in the literature, is given for the dipole electric fields. For interested readers the derivation of this spectral form can be found in Appendix A. This representation of the dipole fields, which consists of integrals of the Sommerfeld type, is the starting point for all derivations that follow. Appropriate Bessel identities are then given which are needed to transform the spectral domain representation into a form which contains Bessel functions of the first kind, of order zero only, an initial step in the derivation. The case of a vertical electric dipole is first examined, in a manner similar to that of Felsen and Marcuvitz [15]. The methodology is then extended to the case of a horizontal electric dipole, where it is noted that duality cannot be applied to solve the equivalent problem of a vertical magnetic dipole radiating above a impedance surface. As mentioned, integral expressions for the horizontal dipole show a diverging exponential term which is not apparent in the formulation by Lindell and Alanen for a dielectric half-space [25]. In Section 2.3 results are given including a comparison of field quantities generated by evaluation of the exact image integrals, and the original Sommerfeld type expressions. In addition a timing comparison shows numerical evaluation of the exact image formulation to be several orders of magnitude faster than numerical evaluation of the corresponding Sommerfeld type integrals. In Section 2.4 the chapter is summarized.

2.2 Exact Image Formulation

Consider the problem geometry shown in Figure 2.1. A small dipole of length l, car-
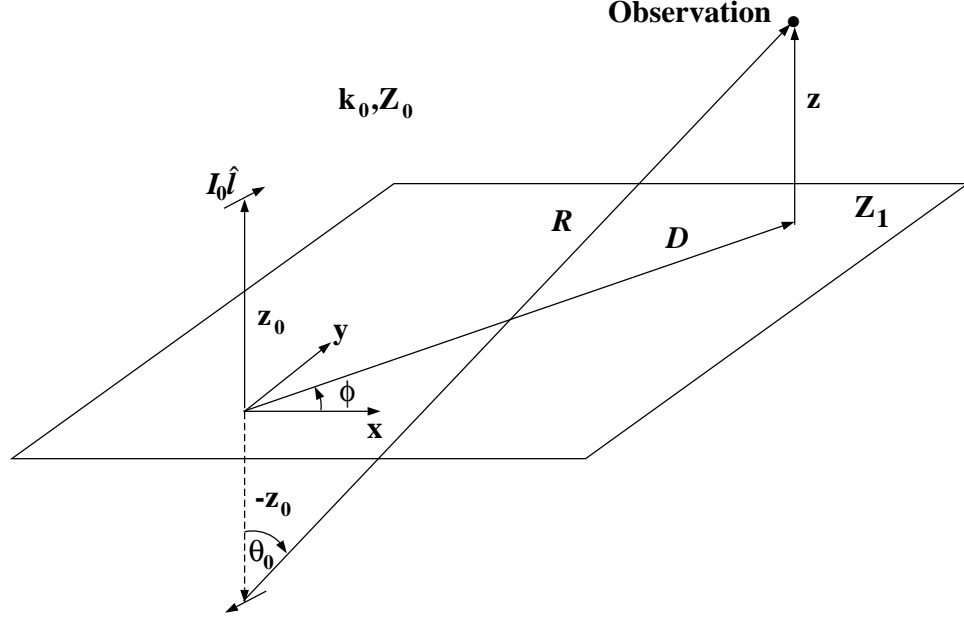
Figure 2.1: Problem geometry, dipole above an impedance plane

rying current I_0 and with orientation $\hat{l}$ is radiating in free space above an infinite, homo-

geneous impedance plane, representative of a lossy Earth. The characteristic impedance

of free space and of the impedance plane are defined as Z_0 and Z_1, respectively. The total

fields above the impedance plane propagate with the propagation constant of free space k_0,

and can be decomposed into a direct wave and diffracted wave given by

$$\mathbf{E}^T(\mathbf{r}, \mathbf{r}_0) = \mathbf{E}^i(\mathbf{r}, \mathbf{r}_0) + \mathbf{E}^d(\mathbf{r}, \mathbf{r}_0), \tag{2.1}$$

where $\mathbf{r} = \sqrt{x^2 + y^2 + z^2}$ is the distance to the observation point and $\mathbf{r}_0 = \sqrt{x_0^2 + y_0^2 + z_0^2}$

is the distance to the source location. Also in (2.1) superscripts T, i and d are indicative of

the total, direct and diffracted fields respectively, the diffracted fields being the perturbation

in the total fields caused by the impedance half-space. $\mathbf{E}^i(\mathbf{r}, \mathbf{r}_0)$ can be calculated directly

and the expression for it is given in Appendix A. Of interest are the diffracted fields and

we begin the exact image derivation with an alternate spectral domain representation of the dipole fields. As the focus of this work is the transformation of the this representation into a form more conducive to numerical evaluation, the derivation will not be repeated here. Interested readers are referred to Appendix A for an explicit derivation of these expressions. The spectral representation of the diffracted electric fields of a dipole of orientation $\hat{l}$, where $\hat{l} = l_x\hat{x} + l_y\hat{y} + l_z\hat{z}$, located at the origin, and radiating above an infinite impedance plane are given by

$$
\begin{aligned}
\mathbf{E}^d(\mathbf{r}, \mathbf{r}_0) = \frac{k_0 Z_0 I_0 l}{4\pi} \Bigg\{ &\hat{x} \int_0^\infty \frac{k_\rho}{2k_z} \{\Gamma_h[-l_x(J_2(k_\rho D)\cos 2\phi + J_0(k_\rho D)) - l_y J_2(k_\rho D)\sin 2\phi)] \\
&+ \Gamma_v[\frac{2ik_z k_\rho}{k_0^2} l_z \cos\phi J_1(k_\rho D) + \frac{k_z^2}{k_0^2} l_x(J_0(k_\rho D) - J_2(k_\rho D)\cos 2\phi) \\
&- \frac{k_z^2}{k_0^2} l_y J_2(k_\rho D)\sin 2\phi]\} \, e^{ik_z(z+z_0)} \, dk_\rho \\
&+ \hat{y} \int_0^\infty \frac{k_\rho}{2k_z} \{\Gamma_h[-l_x J_2(k_\rho D)\sin 2\phi - l_y(J_0(k_\rho D) - J_2(k_\rho D)\cos 2\phi)] \\
&+ \Gamma_v[\frac{2ik_z k_\rho}{k_0^2} l_z \sin\phi J_1(k_\rho D) - \frac{k_z^2}{k_0^2} l_x J_2(k_\rho D)\sin 2\phi \\
&+ \frac{k_z^2}{k_0^2} l_y(J_0(k_\rho D) + J_2(k_\rho D)\cos 2\phi)]\} \, e^{ik_z(z+z_0)} \, dk_\rho \\
&- \hat{z} \int_0^\infty \frac{k_\rho}{k_z} \Gamma_v[\frac{k_\rho^2}{k_0^2} l_z J_0(k_\rho D) + \frac{ik_z k_\rho}{k_0^2} (l_x \cos\phi \\
&+ l_y \sin\phi) J_1(k_\rho D)] \, e^{ik_z(z+z_0)} \, dk_\rho \Bigg\},
\end{aligned}
$$

(2.2)

where Γ_h and Γ_v are the horizontal (TE to z) and vertical (TM to z) Fresnel reflection coefficients, respectively, given by

$$
\Gamma_h = \frac{\eta - k_0/k_z}{\eta + k_0/k_z}, \qquad\qquad \Gamma_v = \frac{-\eta + k_z/k_0}{\eta + k_z/k_0}, \qquad (2.3)
$$

and $\eta = Z_1/Z_0$, is the normalized impedance of the half-space. In (2.2) k_z is the dependent variable defined as $k_z^2 = k_0^2 - k_\rho^2$, and J_0, J_1, and J_2 are Bessel functions of the first kind, of order $0, 1$, and 2 respectively. Also in (2.2) D defines the radial distance between source and observation points, z the height of the observation point, ϕ is the angle between D and the x axis, with z_0 being the height of the source point, all of which are seen in Figure 2.1.

The integrals in (2.2) are Sommerfeld type integrals and as already stated they are highly oscillatory in nature, with poor convergence properties making them difficult to evaluate numerically, especially for the case of $D \gg (z + z_0)$. To improve the convergence behavior of these integrals exact image theory is applied, by the application of integral transforms and appropriate identities. The method is exact with no approximations made and the resulting expressions are valid for any arbitrary source and observation position. The basic methodology is to first rewrite the spectral domain formulation of (2.2) in terms of zero*th* order Bessel functions of the first kind only. Terms containing reflection coefficients in the resulting expressions are expanded where necessary, and then rewritten in the simple form of the Laplace transform of an exponential function. Order of integration is exchanged and the spectral domain integration over k_ρ in (2.2) is performed in an analytic fashion. The remaining expressions in the Laplace domain contain integrals which are dominated by rapidly decaying exponentials and exhibit significantly improved convergence properties over the original Sommerfeld expressions. In the next section relevant transforms and identities will be given that are needed for the derivations that follow.

2.2.1 Transforms & Identities

In this section transforms and identities which are used throughout the derivations that follow are defined. To apply exact image theory Γ_h and Γ_v, given in (2.3), must be defined in terms of a Laplace transform of an exponential function. Γ_h and Γ_v can be rewritten as,

$$\Gamma_h = 1 - \frac{2k_0/\eta}{k_z + k_0/\eta} = 1 - \frac{2\kappa}{k_z + \kappa}, \tag{2.4}$$

18

where $\kappa = k_0/\eta$, and

$$\Gamma_v = 1 - \frac{2\eta k_0}{k_z + \eta k_0} = 1 - \frac{2\gamma}{k_z + \gamma}, \tag{2.5}$$

where $\gamma = \eta k_0$. Now recognizing that

$$\int_0^\infty e^{-\zeta \xi} e^{-k_z \xi} \, d\xi = \frac{1}{k_z + \zeta}, \tag{2.6}$$

where ζ is some constant coefficient, we can rewrite Γ_h and Γ_v in the form of a Laplace transform of an exponential function or,

$$\Gamma_h = 1 - 2\kappa \int_0^\infty e^{-(\kappa + k_z)\xi} \, d\xi, \tag{2.7}$$

and

$$\Gamma_v = 1 - 2\gamma \int_0^\infty e^{-(\gamma + k_z)\xi} \, d\xi. \tag{2.8}$$

In the application of exact image theory to the case of a horizontal dipole, several terms arise in the derivation which contain Γ_h and Γ_v, however cannot be directly expressed as the Laplace transform defined in (2.6). For the sake of simplicity and in order to minimize the complexity of the resulting expressions it is desirable that all integral transforms applied be in the form of this Laplace transform. For a horizontal dipole this is accomplished by expanding the terms, where necessary, by partial fractions into a form which allows them to be directly written in the form of (2.6).

In applying exact image theory to the Sommerfeld type expressions for the fields of a dipole above an impedance surface an initial step in the derivation is to apply Bessel function identities in order to rewrite (2.2) in terms of J_0 only. To do this the following

identities are needed:

$$\frac{1}{k_0^2}\frac{\partial^2}{\partial x^2}J_0(k_\rho D) = -\frac{k_\rho^2}{2k_0^2}\left[J_0(k_\rho D) - \cos 2\phi J_2(k_\rho D)\right], \qquad (2.9)$$

$$\frac{1}{k_0^2}\frac{\partial^2}{\partial y^2}J_0(k_\rho D) = -\frac{k_\rho^2}{2k_0^2}\left[J_0(k_\rho D) + \cos 2\phi J_2(k_\rho D)\right], \qquad (2.10)$$

$$\frac{1}{k_0^2}\left(\frac{\partial^2}{\partial x^2} + \frac{\partial^2}{\partial y^2}\right)J_0(k_\rho D) = -\frac{k_\rho^2}{k_0^2}J_0(k_\rho D), \qquad (2.11)$$

$$\frac{1}{k_0^2}\frac{\partial^2}{\partial x\partial y}J_0(k_\rho D) = \frac{k_\rho^2}{2k_0^2}\sin 2\phi J_2(k_\rho D), \qquad (2.12)$$

$$\frac{1}{k_0^2}\frac{\partial^2}{\partial x\partial z}J_0(k_\rho D) = -i\cos\phi\frac{k_z k_\rho}{k_0^2}J_1(k_\rho D), \qquad (2.13)$$

$$\frac{1}{k_0^2}\frac{\partial^2}{\partial y\partial z}J_0(k_\rho D) = -i\sin\phi\frac{k_z k_\rho}{k_0^2}J_1(k_\rho D). \qquad (2.14)$$

An additional identity which will allows for the analytic evaluation of the spectral domain integrals over k_ρ in the exact image expressions is

$$\frac{e^{ik_0 R}}{R} = i\int_0^\infty J_0(k_\rho D)\, e^{ik_z(z+z_0)}\,\frac{k_\rho}{k_z}\,dk_\rho, \qquad (2.15)$$

where $R = \sqrt{(x-x_0)^2 + (y-y_0)^2 + (z+z_0)^2}$. The identity in (2.15) relates the free space Green's function to an alternate representation in the form of a Sommerfeld integral and is appropriately referred to in the literature as the Sommerfeld Integral Identity.

20

2.2.2 Vertical Electric Dipole

To find the diffracted fields generated by a vertical (z directed) dipole, the components of (2.2) containing l_z are first considered and then modified to include only zero*th* order Bessel functions. The reflection coefficients are rewritten in terms of their Laplace transform and then the order of integration is exchanged in order to evaluate the integral in terms of k_ρ analytically, using the Sommerfeld Integral Identity given by (2.15).

For a vertical dipole (2.2) reduces to

$$\mathbf{E}_v^d(\mathbf{r},\mathbf{r}_0) = \frac{k_0 Z_0 I_0 l}{4\pi} \, l_z \int\limits_0^\infty \frac{k_\rho}{k_z} \, \Gamma_v \left\{ \frac{ik_z k_\rho}{k_0^2} \cos\phi J_1(k_\rho D) \, \hat{x} \right.$$
$$\left. + \frac{ik_z k_\rho}{k_0^2} \sin\phi J_1(k_\rho D) \, \hat{y} - \frac{k_\rho^2}{k_0^2} J_0(k_\rho D) \, \hat{z} \right\} e^{ik_z(z+z_0)} \, dk_\rho,$$

(2.16)

where the subscript v in (2.16) designates a vertical dipole. Applying the identities in Section 2.2.1, (2.16) can be rewritten as

$$\mathbf{E}_v^d(\mathbf{r},\mathbf{r}_0) = -\frac{Z_0 I_0 l}{4\pi k_0} \, l_z \left\{ \frac{\partial^2}{\partial x \partial z}\hat{x} + \frac{\partial^2}{\partial y \partial z}\hat{y} - \left(\frac{\partial^2}{\partial x^2} + \frac{\partial^2}{\partial y^2} \right)\hat{z} \right\}$$
$$\int\limits_0^\infty \frac{k_\rho}{k_z} \, \Gamma_v \, J_0(k_\rho D) \, e^{ik_z(z+z_0)} \, dk_\rho.$$

(2.17)

Now rewriting Γ_v in the form of (2.8), and substituting into (2.17) gives

$$\mathbf{E}_v^d(\mathbf{r},\mathbf{r}_0) = -\frac{Z_0 I_0 l}{4\pi k_0} \, l_z \left\{ \frac{\partial^2}{\partial x \partial z}\hat{x} + \frac{\partial^2}{\partial y \partial z}\hat{y} - \left(\frac{\partial^2}{\partial x^2} + \frac{\partial^2}{\partial y^2} \right)\hat{z} \right\}$$
$$\left[\int\limits_0^\infty \frac{k_\rho}{k_z} \, J_0(k_\rho D) \, e^{ik_z(z+z_0)} \, dk_\rho \right.$$

(2.18)

$$\left. - 2\gamma \int\limits_0^\infty \int\limits_0^\infty \frac{k_\rho}{k_z} \, J_0(k_\rho D) \, e^{-\gamma\xi} e^{ik_z(z+z_0+i\xi)} \, dk_\rho \, d\xi \right].$$

The integrals in (2.18) in terms of k_ρ can be solved analytically by applying the Sommerfeld

21

integral identity of (2.15), giving the final form of the diffracted electric fields for a vertical
(z directed) dipole

$$\mathbf{E}_v^d(\mathbf{r}, \mathbf{r}_0) = \frac{iZ_0 I_0 l}{4\pi k_0} \, l_z \left\{ \frac{\partial^2}{\partial x \partial z} \hat{x} + \frac{\partial^2}{\partial y \partial z} \hat{y} - \left(\frac{\partial^2}{\partial x^2} + \frac{\partial^2}{\partial y^2} \right) \hat{z} \right\}$$
$$\left[\frac{e^{ik_0 R}}{R} - 2\gamma \int_0^\infty e^{-\gamma\xi} \frac{e^{ik_0 R'(\xi)}}{R'(\xi)} \, d\xi \right], \tag{2.19}$$

where R is as previously defined and $R'(\xi) = \sqrt{(x-x_0)^2 + (y-y_0)^2 + (z+z_0+i\xi)^2}$. The
integrand in the last term of (2.19) can be interpreted as a distributed image source in the
complex z plane located at $-z_0$, and as seen in Figure 2.2. In this integrand both exponential
factors, $-\gamma\xi$, and $-k_0 R'(\xi)$, decay rapidly as ξ becomes large. Due to this, the integral in
(2.19) converges very rapidly, for all source and observation locations.
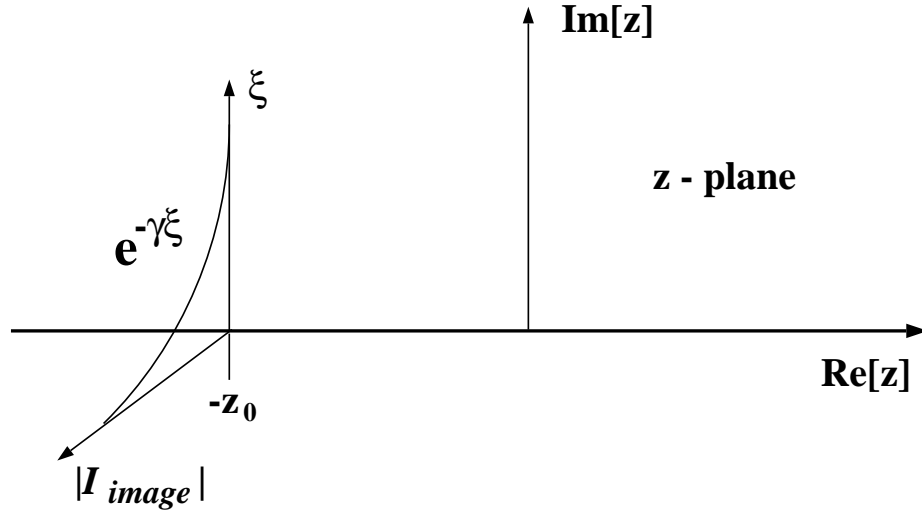
Figure 2.2: Exact image in z-plane

2.2.3 Horizontal Electric Dipole

Before beginning the derivation of the fields from a horizontal electric dipole a brief
note about the application of duality is relevant. Having solved the problem of the elec-
tric fields from a vertical electric dipole above an impedance half-space, the problem of

the magnetic fields of a vertical magnetic dipole above a similar half-space can be immediately written by applying duality. Through Maxwell's equations, electric fields are obtained, equivalent to those generated by a loop of electric current in the $x - y$ plane, and it would appear at first glance that a solution which gives some insight into the problem of a horizontal electric dipole is at hand. Several problems arise however. First it is desired to obtain accurate dipole fields for any dipole orientation and observation and information about the effects of the dipole pattern are lost in the dual solution. Also in applying duality the case of an impedance surface is transformed to that of an admittance surface, which gives little physical insight into the problem. Because of these issues, the case of a horizontal dielectric dipole radiating above an impedance half-space will be derived directly. As the scalar potential is not obvious in the expressions for a horizontal dipole, the derivation to be presented, while somewhat more cumbersome algebraically, results in complete field expressions in terms of the exact image formulation for arbitrary dipole orientation in the $x - y$ plane.

In a manner similar to that of the vertical dipole appropriate terms in the Sommerfeld type expressions for a horizontal dipole will be put in terms of J_0 only to facilitate evaluation of the integral over k_ρ analytically. Initially the x component of the electric field is derived. The y component is determined in the same fashion, which for brevity will not be repeated, and only the final result is provided. Finally the z component of the field generated by a horizontal electric dipole is derived.

To derive the x component of the diffracted electric field for a horizontal electric dipole the identities of (2.9) through (2.14) are applied, and noting that $k_z^2 = k_0^2 - k_\rho^2$, (2.2), be-

comes

$$\mathbf{E}_h^d(\mathbf{r}, \mathbf{r}_0) \cdot \hat{x} = \frac{k_0 Z_0 I_0 l}{4\pi} \int\limits_0^\infty \left[\frac{l_x}{k_\rho^2} \left(\Gamma_h \frac{\partial^2}{\partial y^2} - \Gamma_v \frac{k_0^2 - k_\rho^2}{k_0^2} \frac{\partial^2}{\partial x^2} \right) \right.$$
$$\left. - \frac{l_y}{k_\rho^2} \left(\Gamma_h + \Gamma_v \frac{k_0^2 - k_\rho^2}{k_0^2} \right) \frac{\partial^2}{\partial x \partial y} \right] \frac{k_\rho}{k_z} J_0(k_\rho D) \, e^{ik_z(z+z_0)} dk_\rho,$$

$$(2.20)$$

where the subscript h designates a horizontal dipole. (2.20) can be rewritten as

$$\mathbf{E}_h^d(\mathbf{r}, \mathbf{r}_0) \cdot \hat{x} = \frac{k_0 Z_0 I_0 l}{4\pi} \left\{ l_x \left(\frac{\partial^2}{\partial y^2} f_a - \frac{\partial^2}{\partial x^2} f_b + \frac{1}{k_0^2} \frac{\partial^2}{\partial x^2} f_c \right) \right.$$
$$\left. - l_y \frac{\partial^2}{\partial x \partial y} \left(f_a + f_b - \frac{1}{k_0^2} f_c \right) \right\},$$

$$(2.21)$$

where

$$f_a = \int\limits_0^\infty \frac{k_\rho}{k_z} J_0(k_\rho D) \, e^{ik_z(z+z_0)} \frac{\Gamma_h}{k_\rho^2} \, dk_\rho, \qquad (2.22)$$

$$f_b = \int\limits_0^\infty \frac{k_\rho}{k_z} J_0(k_\rho D) \, e^{ik_z(z+z_0)} \frac{\Gamma_v}{k_\rho^2} \, dk_\rho, \qquad (2.23)$$

and

$$f_c = \int\limits_0^\infty \frac{k_\rho}{k_z} J_0(k_\rho D) \, e^{ik_z(z+z_0)} \, \Gamma_v \, dk_\rho. \qquad (2.24)$$

While f_c can be evaluated directly by expressing Γ_v in the form of (2.8) (as in the previous section, eqns. (2.17), (2.18), and (2.19)), the terms Γ_h/k_ρ^2 and Γ_v/k_ρ^2, in f_a, and f_b, cannot be directly written in terms of the Laplace transform of (2.6), however by applying partial

24

fraction expansion they can be put in the appropriate form. Defining these terms as

$$A = \frac{\Gamma_h}{k_\rho^2}, \qquad B = \frac{\Gamma_v}{k_\rho^2}, \tag{2.25}$$

writing Γ_h and Γ_v explicitly in terms of k_0, k_z, κ, and γ (see (2.4) and (2.5)), and recognizing that $k_\rho^2 = k_0^2 - k_z^2 = (k_0 - k_z)(k_0 + k_z)$, A and B can be written as

$$A = \frac{k_z - \kappa}{(k_0 - k_z)(k_0 + k_z)(k_z + \kappa)}, \tag{2.26}$$

and

$$B = \frac{k_z - \gamma}{(k_0 - k_z)(k_0 + k_z)(k_z + \gamma)}. \tag{2.27}$$

Expanding (2.26) and (2.27) by partial fractions gives expressions of the following form for A and B

$$A = \frac{A_1}{(k_0 - k_z)} + \frac{A_2}{(k_0 + k_z)} + \frac{A_3}{(k_z + \kappa)}, \tag{2.28}$$

$$B = \frac{B_1}{(k_0 - k_z)} + \frac{B_2}{(k_0 + k_z)} + \frac{B_3}{(k_z + \gamma)}, \tag{2.29}$$

where

$$A_1 = -B_1 = \frac{\eta - 1}{2k_0(\eta + 1)},$$

$$A_2 = -B_2 = \frac{\eta + 1}{2k_0(\eta - 1)}, \tag{2.30}$$

$$A_3 = -B_3 = \frac{2\eta}{k_0(1 - \eta^2)},$$

and where the coefficients in (2.30) are given explicitly in terms of normalized impedance η and k_0, which will be used in the final expressions for the x component of the diffracted electric fields. Now representing each term of the partial fraction expansions of (2.28) and (2.29) in the form of the Laplace transform of (2.6), changing the order of integration as before and applying (2.15) to evaluate the integral over k_ρ analytically, gives the following expressions for f_a and f_b

$$f_a = -i \int_0^\infty \left[e^{-k_0\xi} \left(A_1 \frac{e^{ik_0R''(\xi)}}{R''(\xi)} + A_2 \frac{e^{ik_0R'(\xi)}}{R'(\xi)} \right) + A_3 \, e^{-\kappa\xi} \frac{e^{ik_0R'(\xi)}}{R'(\xi)} \right] d\xi, \qquad (2.31)$$

$$f_b = -i \int_0^\infty \left[e^{-k_0\xi} \left(B_1 \frac{e^{ik_0R''(\xi)}}{R''(\xi)} + B_2 \frac{e^{ik_0R'(\xi)}}{R'(\xi)} \right) + B_3 \, e^{-\gamma\xi} \frac{e^{ik_0R'(\xi)}}{R'(\xi)} \right] d\xi, \qquad (2.32)$$

where $R''(\xi) = \sqrt{(x-x_0)^2 + (y-y_0)^2 + (z+z_0-i\xi)^2}$. Also the expression for f_c is given by

$$f_c = -i \left\{ \frac{e^{ik_0R}}{R} - 2\gamma \int_0^\infty e^{-\gamma\xi} \frac{e^{ik_0R'(\xi)}}{R'(\xi)} \, d\xi \right\}. \qquad (2.33)$$

26

Noting that $B = -A$, (2.21) can now be rewritten as

$$
\begin{aligned}
\mathbf{E}_h^d(\mathbf{r}, \mathbf{r}_0) \cdot \hat{x} = ik_0 Z_0 I_0 l \Bigg\{ & l_x \left(\frac{\partial^2}{\partial x^2} + \frac{\partial^2}{\partial y^2} \right) \\
& \int_0^\infty \left[\frac{1-\eta}{2k_0(1+\eta)} e^{-k_0\xi} \frac{e^{ik_0 R''(\xi)}}{4\pi R''(\xi)} + \frac{1+\eta}{2k_0(1-\eta)} e^{-k_0\xi} \frac{e^{ik_0 R'(\xi)}}{4\pi R'(\xi)} \right] d\xi \\
& - l_x \frac{2\eta}{k_0(1-\eta^2)} \int_0^\infty \left[e^{-\kappa\xi} \frac{\partial^2}{\partial y^2} \frac{e^{ik_0 R'(\xi)}}{4\pi R'(\xi)} + e^{-\gamma\xi} \frac{\partial^2}{\partial x^2} \frac{e^{ik_0 R'(\xi)}}{4\pi R'(\xi)} \right] d\xi \\
& - \frac{1}{k_0^2} \left(l_x \frac{\partial^2}{\partial x^2} + l_y \frac{\partial^2}{\partial x \partial y} \right) \left[\frac{e^{ik_0 R}}{4\pi R} - 2k_0\eta \int_0^\infty e^{-\gamma\xi} \frac{e^{ik_0 R'(\xi)}}{4\pi R'(\xi)} d\xi \right] \\
& + l_y \frac{\partial^2}{\partial x \partial y} \left(\frac{2\eta}{k_0(1-\eta^2)} \right) \int_0^\infty (e^{-\kappa\xi} - e^{-\gamma\xi}) \frac{e^{ik_0 R'(\xi)}}{4\pi R'(\xi)} d\xi \Bigg\},
\end{aligned}
$$

(2.34)

In (2.34) an additional term is observed, containing the exponential factor $R''(\xi)$, which is not present in the expressions for the vertical dipole and also is not evident in the formulation by Lindell and Alanen for a horizontal dipole over a dielectric half-space [25]. This denotes the image location in the conjugate complex z-plane which results in an exponentially diverging factor. While this term is an exponentially growing term, the image current distribution, which depends on the surface impedance, is exponentially decaying at a greater rate and dominates the integrand ($\xi > Im[R''(\xi)]$). Because of this the integral in the first term of (2.34) still exhibits the rapid convergence properties inherent in the integral expressions generated by the application of exact image theory.

The y component of the diffracted electric field generated by a horizontal dipole is derived in a similar fashion and for the sake of brevity is not repeated here. The expression

for it is given by

$$
\mathbf{E}_h^d(\mathbf{r}, \mathbf{r}_0) \cdot \hat{y} = ik_0 Z_0 I_0 l \left\{ l_y \left(\frac{\partial^2}{\partial x^2} + \frac{\partial^2}{\partial y^2} \right) \right.
$$

$$
\int_0^\infty \left[\frac{1 - \eta}{2k_0(1 + \eta)} e^{-k_0 \xi} \frac{e^{ik_0 R''(\xi)}}{4\pi R''(\xi)} + \frac{1 + \eta}{2k_0(1 - \eta)} e^{-k_0 \xi} \frac{e^{ik_0 R'(\xi)}}{4\pi R'(\xi)} \right] d\xi
$$

$$
- l_y \frac{2\eta}{k_0(1 - \eta^2)} \int_0^\infty \left[e^{-\kappa \xi} \frac{\partial^2}{\partial x^2} \frac{e^{ik_0 R'(\xi)}}{4\pi R'(\xi)} + e^{-\gamma \xi} \frac{\partial^2}{\partial y^2} \frac{e^{ik_0 R'(\xi)}}{4\pi R'(\xi)} \right] d\xi
$$

$$
- \frac{1}{k_0^2} \left(l_y \frac{\partial^2}{\partial y^2} + l_x \frac{\partial^2}{\partial x \partial y} \right) \left[\frac{e^{ik_0 R}}{4\pi R} - 2k_0 \eta \int_0^\infty e^{-\gamma \xi} \frac{e^{ik_0 R'(\xi)}}{4\pi R'(\xi)} d\xi \right]
$$

$$
\left. + l_x \frac{\partial^2}{\partial x \partial y} \left(\frac{2\eta}{k_0(1 - \eta^2)} \right) \int_0^\infty (e^{-\kappa \xi} - e^{-\gamma \xi}) \frac{e^{ik_0 R'(\xi)}}{4\pi R'(\xi)} d\xi \right\}.
$$

(2.35)

Derivation of the z component of the diffracted electric field generated by a horizontal dipole is rather straightforward. Beginning with (2.2) and applying the appropriate identities we arrive at

$$
\mathbf{E}_h^d(\mathbf{r}, \mathbf{r}_0) \cdot \hat{z} = \frac{1}{k_0^2} \left(l_x \frac{\partial^2}{\partial x \partial z} + l_y \frac{\partial^2}{\partial y \partial z} \right) \int_0^\infty \frac{k_\rho}{k_z} \Gamma_v J_0 e^{ik_z(z + z_0)} dk_\rho,
$$

(2.36)

and recognizing the integral in (2.36) as f_c, the z component of the electric field generated by a horizontal dipole is given by

$$
\mathbf{E}_h^d(\mathbf{r}, \mathbf{r}_0) \cdot \hat{z} = -ik_0 Z_0 I_0 l \left\{ \frac{1}{k_0^2} \left(l_x \frac{\partial^2}{\partial x \partial z} + l_y \frac{\partial^2}{\partial y \partial z} \right) \right.
$$

$$
\left. \left[\frac{e^{ik_0 R}}{4\pi R} - 2\gamma \int_0^\infty e^{-\gamma \xi} \frac{e^{ik_0 R'(\xi)}}{4\pi R'(\xi)} d\xi \right] \right\}.
$$

(2.37)

2.3   Analysis & Results: Exact Image Theory

In this section a validation of the exact image method will be given, along with timing results showing the significant speed-up in computation time over that of the original Som-

28

merfeld type expressions. In the results that follow all integrals are numerically evaluated using the Gaussian quadrature numerical integration package Quadpack contained in the Slatec mathematical computation libraries. The Quadpack routines require defining both an absolute and relative error parameter, and these were set at 0.0 and 0.001 respectively.

For the initial comparison of the exact image formulation to the original Sommerfeld type expressions, consider an electric dipole located 2m above the impedance surface ($z_0 = 2m$), at the coordinate origin ($x_0 = y_0 = 0$) and radiating at 30 MHz. All field quantities are normalized to dipole length l, current I_0 and wavelength λ ($\mathbf{E}/(I_0 l/\lambda)$), for all cases. The geometry and coordinates are again as shown in Figure 2.1. The observation is on a radial line, 2m above the impedance surface ($z = 2m$), ranging from 10m to 10010m along the x axis ($D = 10 \rightarrow 10010m$, $\phi = 0$) and field values are calculated at 11 data points along this line. The normalized surface impedance value is chosen to be $\eta = 0.3 - i0.1$ corresponding to the impedance of San Antonio Gray Clay Loam with a 5% gravimetric moisture content and a density of 1.4 g/cm^3, derived from the values of permittivity and conductivity given by Hipp [1], and as shown in Table 1.1.

Figure 2.3 shows the x component of the diffracted electric field, for a vertical dipole, for this test case (no direct x field component in this case). In Figure 2.3 results from numerical evaluation of the exact image expressions are compared to results from numerical evaluation of the original Sommerfeld type expressions. As can be seen the two results are in excellent agreement. For the same test case Figure 2.4 shows the diffracted and total (direct + diffracted) z electric field components for a vertical (z directed) dipole, again comparing the exact image calculation to those of the Sommerfeld formulation. As can be seen in Figure 2.4 the diffracted fields are in good agreement, except for a slight discrepancy at 4000m, where evaluation of the Sommerfeld type integrals did not completely converge. The total fields in Figure 2.4 show increased error at 4000m for the Sommerfeld solution and also at distances beyond 6000m. This is due to the fact that the total field is the result of two large numbers (direct and diffracted field) tending to cancel, for source and obser-
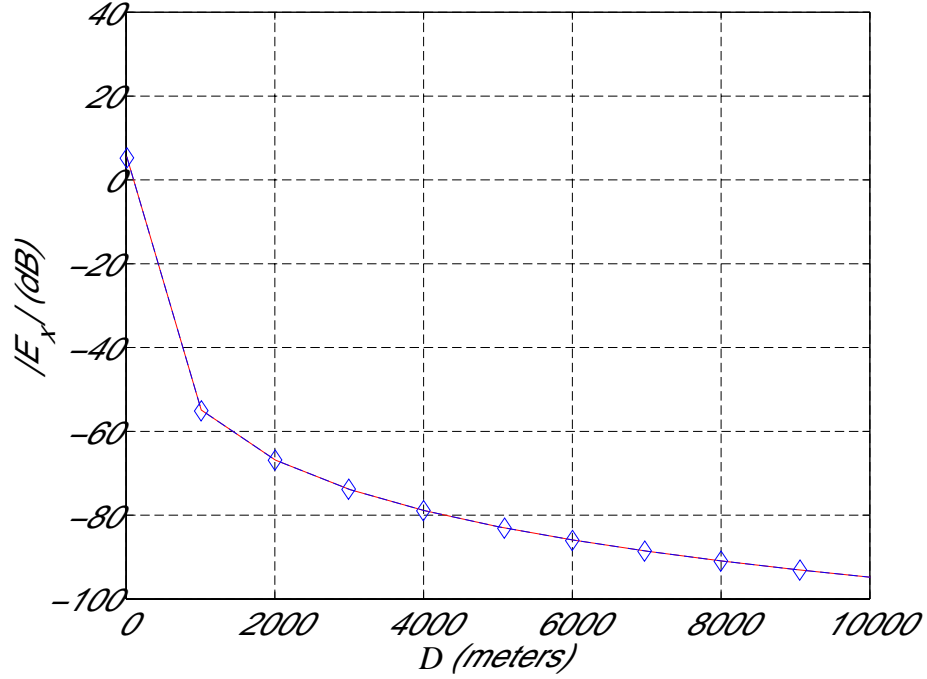
Figure 2.3: x-component of total electric fields (diffracted only for this case) for a vertical ($\hat{z}$) electric dipole, exact image (———) compared with Sommerfeld ($\diamond\diamond\diamond\diamond\diamond$). Dipole is located at $x_0 = y_0 = 0$, $z_0 = 2m$ and operating at 30 MHz. Observation is at $z = 2m$, $D = 10 - 10010m$, along the $\phi = 0$ (x axis). Normalized Surface impedance value is $\eta = 0.3 - i0.1$.

vation near the impedance surface. This has the effect of highlighting the numerical error in the Sommerfeld integrals for the diffracted field, while the curves generated by the exact image formulation decay smoothly as expected, thus indicating better convergence in the numerical solution. This in fact is the case where higher order terms (Norton surface wave) in the approximate asymptotic solutions dominate the total fields for $R \gg (z + z_0)$. To evaluate the effects of the Norton surface wave we observe that the expression for f_c given in (2.24) is simply the z directed potential for a vertical dipole. Defining this potential as G_z, the asymptotic solution of G_z can be decomposed as

$$G_z = G_z^i + G_z^{go} + G_z^{nsw} \tag{2.38}$$

where superscript i indicates the direct wave, go is the Geometrical Optics (GO) term,

30
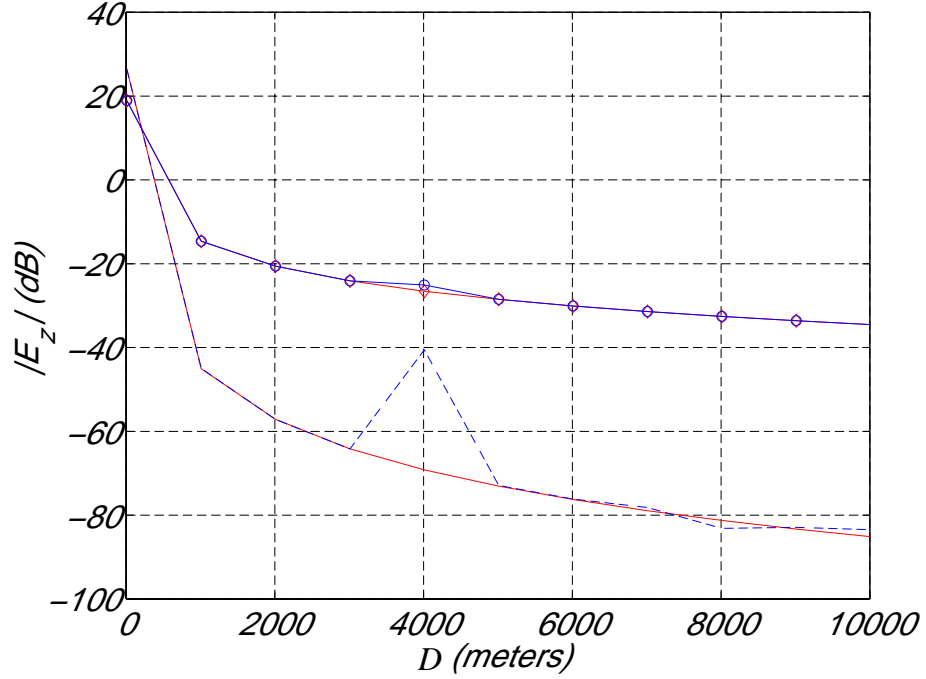
Figure 2.4: z-component of diffracted (exact image ($\diamond\diamond\diamond\diamond\diamond$) and Sommerfeld ($\circ\circ\circ\circ\circ$)) and total electric fields (exact image (————) and Sommerfeld ($-\ -\ -\ -$)) for a vertical ($\hat{z}$) electric dipole. Dipole is located at $x_0 = y_0 = 0$, $z_0 = 2m$ and operating at 30 MHz. Observation is at $z = 2m$, $D = 10 - 10010m$, along the $\phi = 0$ (x axis). Normalized Surface impedance value is $\eta = 0.3 - i0.1$.

equivalent to the first order Saddle point solution, and *nsw* indicates the Norton surface wave component of the asymptotic solution, which is simply the higher order terms in the Saddle point expansion, and which decay as $1/R^2$. The first two terms in (2.38) are given by

$$G_z^i + G_z^{go} = \frac{e^{ik_0R_0}}{4\pi R_0} + \Gamma_{v,sp}\frac{e^{ik_0R}}{4\pi R} \tag{2.39}$$

where $R_0 = \sqrt{(x-x_0)^2 + (y-y_0)^2 + (z-z_0)^2}$ and $\Gamma_{v,sp}$ is the vertical Fresnel reflection coefficient evaluated at the saddle point, and given by

$$\Gamma_{v,sp} = \frac{\cos\theta_0 - \eta}{\cos\theta_0 + \eta}. \tag{2.40}$$

31

In (2.40) $\cos\theta_0 = (z + z_0)/R$, and θ_0 is as defined in Figure 2.1. Equation (2.39) can be rewritten as

$$G_z = \frac{e^{ik_0 R_0}}{4\pi R_0} - \frac{e^{ik_0 R}}{4\pi R} + \frac{2\cos\theta_0}{\cos\theta_0 + \eta}, \tag{2.41}$$

As source and observation move near the impedance surface the first two terms in (2.41) tend to cancel and terms which decay as $1/\rho^2$ tend to dominate. These terms are implicit in the third term of (2.41) and the higher order terms of the asymptotic expansion (Norton surface wave). Assuming that $|\eta| \gg \cos\theta_0$, expanding (2.41) in a Taylor series, and representing $\cos\theta_0$ in terms of z, z_0, and ρ, the decay as $1/\rho^2$ as well as the dependence of (2.41) on η become explicit and (2.41) now becomes

$$G_z^i + G_z^{go} = \frac{1}{2\pi\rho^2} \left(-ik_0 z z_0 + \frac{z + z_0}{\eta} \right) e^{ik_0\rho}, \tag{2.42}$$

where in (2.42) it is assumed that a pole is not in the vicinity of the saddle point. Again assuming that $|\eta| \gg \cos\theta_0$, the higher order terms in the asymptotic expansion (Norton surface wave) are given by,

$$G_z^{nsw} = \frac{\sqrt{-i}}{8\pi k_0 \rho^2} \left[\frac{1}{4} - \frac{4}{\eta^2} \right] e^{ik_0\rho}. \tag{2.43}$$

Figure 2.5 shows the y components of the total electric field for a horizontal (y directed) dipole, and for the same test case. Again the convergence problems of the Sommerfeld type integrals are apparent in Figure 2.5 in the degradation of the appropriate curve beyond 2000m.

Having compared the accuracy of the exact image formulation to that of the original Sommerfeld expressions the significant improvement in computational time will now be discussed. In Figure 2.6 and Figure 2.7 the computation time (in seconds), required to calculate all field components at each observation point is plotted for this same test case. The
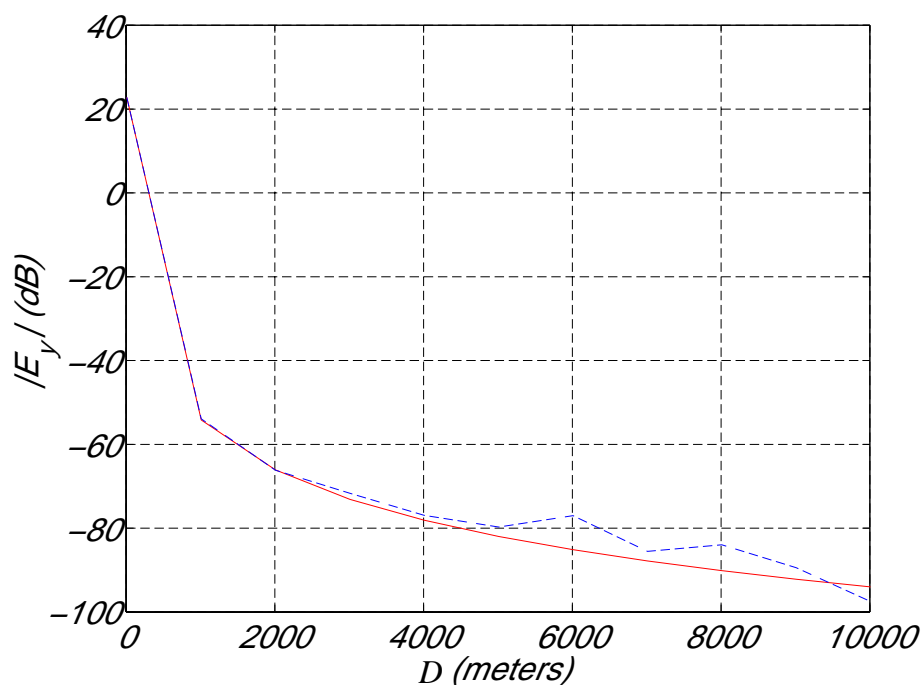
Figure 2.5: *y*-component of total electric fields for a horizontal ($\hat{y}$) electric dipole, exact image (———) compared with Sommerfeld ($- - - -$). Dipole is located at $x_0 = y_0 = 0$, $z_0 = 2m$ and operating at 30 MHz. Observation is at $z = 2m$, $D = 10 - 10010m$, along the $\phi = 0$ (*x* axis). Normalized Surface impedance value is $\eta = 0.3 - i0.1$.

curves in Figure 2.6 compare the time required for numerical evaluation of the Sommerfeld type solution for the case of a vertical dipole, to the time required for the exact image formulation to perform the same field calculations. Figure 2.7 shows a similar comparison for a horizontal (*y* directed) electric dipole. As is obvious from both sets of curves, the computation time required for the exact image calculations are significantly faster than the time required to calculate the Sommerfeld integrals, in fact over two orders of magnitude faster as the observation distance goes beyond 2000*m*. Note that for both methods only necessary integrals were evaluated, i.e., for example, the integrals containing l_x were not called if the dipole was strictly *z* directed (l_z component only). In continuing with a comparison of computation time between exact image and the Sommerfeld integrals, Table 2.1 shows a comparison of the speed-up in computation time required by the exact image formulation
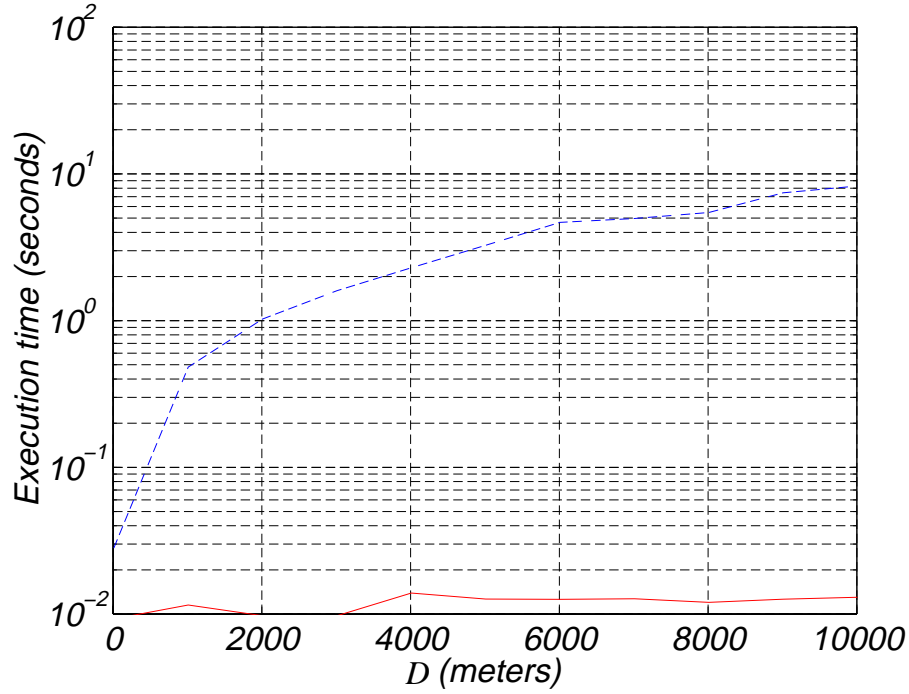
Figure 2.6: Time (in seconds) to calculate all electric field components, at each observation point, for a vertical ($\hat{z}$) electric dipole, exact image (————) and Sommerfeld ($-$ $-$ $-$ $-$). Dipole is located at $x_0 = y_0 = 0$, $z_0 = 2m$ and operating at 30 MHz. Observation is at $z = 2m$, $D = 10 - 10010m$, along the $\phi = 0$ (x axis). Normalized Surface impedance value is $\eta = 0.3 - i0.1$.

over the original Sommerfeld type expressions. Speed-up is defined as the ratio of the time required to calculate the Sommerfeld expressions to that required to perform the exact image calculations (Sommerfeld time (seconds)/ exact image time (seconds)). In Table 2.1 the computation time for each method is the time required to calculate all field components at all observation positions (still eleven data points, from $D = 10 \rightarrow 10010m$, $\phi = 0$), again for the case of $\eta = 0.3 - i0.1$, but with varying source and observation heights. As is seen in Table 2.1 the exact image calculations exhibit a significant speed-up in convergence time, over the Sommerfeld type expression, for numerical evaluation of the integrals. As a final comparison of computation times, Table 2.2 shows the speed-up in computation time of the exact image formulation over the Sommerfeld type expressions, for varying normalized complex impedance values and for eleven data points, from $D = 10 \rightarrow 10010m$, $\phi = 0$,
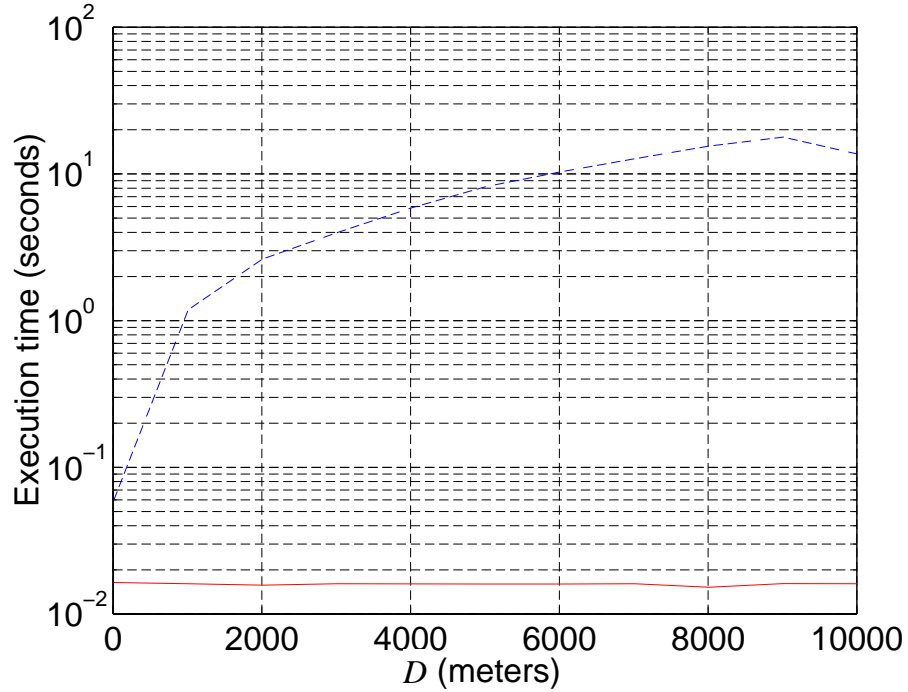
Figure 2.7: Time (in seconds) to calculate all electric field components, at each observation point, for a horizontal ($\hat{y}$) electric dipole, exact image (————) and Sommerfeld ($-$ $-$ $-$ $-$). Dipole is located at $x_0 = y_0 = 0$, $z_0 = 2m$ and operating at 30 MHz. Observation is at $z = 2m$, $D = 10 - 10010m$, along the $\phi = 0$ (x axis). Normalized Surface impedance value is $\eta = 0.3 - i0.1$.

and for source and observation $2m$ above the impedance surface. Again the exact image calculations are at least an order of magnitude faster than the Sommerfeld calculations for all cases except that of a PEC surface.

Also in this section the effects of varying soil moisture on the total electric fields of a vertical dipole, are presented. The dipole is again radiating at 30 MHz, with source $2m$ above the impedance surface, observation is also $2m$ above the impedance surface, and again along the x axis from $D = 10$ to $D = 10010m$. Figure 2.8 shows a comparison of the z component of the total electric fields, calculated using the exact image expressions, for the same San Antonio Gray Clay Loam previously described, and again with a density of $1.4 \, g/cm^3$. The curves show field levels for gravimetric moisture contents of $0\%, 2.5\%, 5\%$, 10%, and 20%, corresponding to normalized surface impedances (η) of $0.53, 0.38 - i0.09$,

Table 2.1: Speed-up in computation time of exact image calculation over Sommerfeld type integrals for normalized surface impedance of 0.3-i0.1, eleven data points from $D = 10 \to 10010m$, $\phi = 0$ and varying source/observation heights.

$z_0(m)$	$z(m)$	Speed-up, Vertical Dipole	Speed-up, Horizontal Dipole
2	2	303.92	565.96
2	200	54.89	106.92
200	2	56.11	107.00
200	200	65.00	110.00

Table 2.2: Speed-up in computation time of exact image calculation over Sommerfeld type integrals for varying complex impedance, η. Source and receiver are $2m$ above surface for all cases. Eleven data points are calculated from $D = 10 \to 10010m$, $\phi = 0$.

η	Speed-up, Vertical Dipole	Speed-up, Horizontal Dipole
0.0-i0.0	5.41	13.86
0.1-i0.0	282.00	613.80
0.3-i0.0	318.17	624.60
0.5-i0.0	490.38	715.92
0.003-i0.1	9.81	31.03
0.003-i0.3	10.03	18.3
0.003-i0.5	9.96	14.51
0.1-i0.1	254.29	425.62
0.3-i0.3	266.00	452.20
0.5-i0.5	348.25	510.28

$0.3 - i0.1$, $0.15 - i0.09$, $0.12 - i0.07$, respectively. As can be seen in Figure 2.8 the effect of increasing moisture content (η is decreased) is to increase the vertical component of the total electric fields by as much as 20 dB over the range shown. This dependence on η can be seen in the asymptotic form of the fields ((2.42)). A similar analysis for a horizontal dipole (y directed and again observation along the x axis) showed the total field levels to be essentially insensitive to varying soil moisture.

As a final example the frequency response of the field of a vertical dipole over the impedance half-space is examined. The frequency response is indicative of the dispersive effects of the half-space, and these effects are of significant interest in the point to point
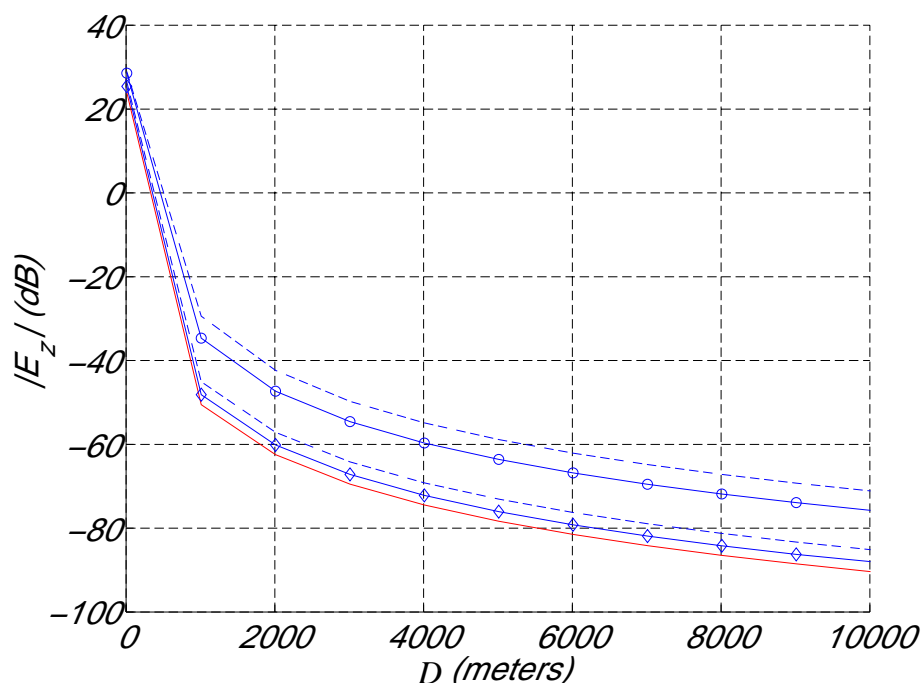
Figure 2.8: Effect of varying soil moisture on z-component of total electric fields for a vertical ($\hat{z}$) dipole located at the origin, 2m above an impedance surface, ($x_0 = y_0 = 0, z_0 = 2m$) and operating at 30 MHz. Observation is also 2m above the surface and extends radially from the source along the $\phi = 0$ (x axis) from $D = 10 - 10010m$. Results are for soil moisture of 0% ($\eta = 0.53$, (————)), 2.5% ($\eta = 0.38 - i0.09$, ($\circ\circ\circ\circ\circ$)), 5% ($\eta = 0.3 - i0.1$, ($- - - -$)), 10% ($\eta = 0.15 - i0.09$, ($\circ\circ\circ\circ\circ$)) and 20% ($\eta = 0.12 - i0.07$, ($\cdot - \cdot - \cdot - \cdot$))

transmission of wideband radio signals over the earth. For this example the source and observation are placed $2m$ above the surface and the frequency response is examined at radial distance $D = 300m$ from the source. Frequency is swept from 30 MHz to 130 MHz in steps of 142.86 KHz. For obvious reasons the electric field quantities are not normalized to $I_0 l / \lambda$ as in the previous examples. Also field expressions must be multiplied by the dipole length (in meters), and in this example the length is set at $0.2307m$ ($\lambda/10$ at 130MHz). As the normalized impedance of the surface varies with frequency, the appropriate real component of the relative permittivity (ε'_r) and conductivity (σ) are selected from the tables given by Hipp [1] (Table 1.1) and the normalized impedance calculated from these parameters at each frequency. As previously mentioned these values are slowing varying functions of

frequency so the values given in Table 1.1, are assumed to be constant across the band. The normalized impedance, η, at each frequency is then given by $\eta = 1/\sqrt{\varepsilon'_r + i\varepsilon''_r}$, where $\varepsilon''_r = \sigma/(\omega\varepsilon_0)$ and $\varepsilon_0 = 8.85 \times 10^{-12}$ is the permittivity of free space. For this example these values were again chosen to be representative of San Antonio Gray Clay Loam with a 20% gravimetric moisture content and a density of $1.4\ g/cm^3$ ($\varepsilon'_r = 24.0$ and $\sigma = 8 \times 10^{-2}$ in Table 1.1). Figure 2.9 and Figure 2.10 compare the magnitude and phase of the frequency response of the direct dipole field to that of the total field. It is shown that the
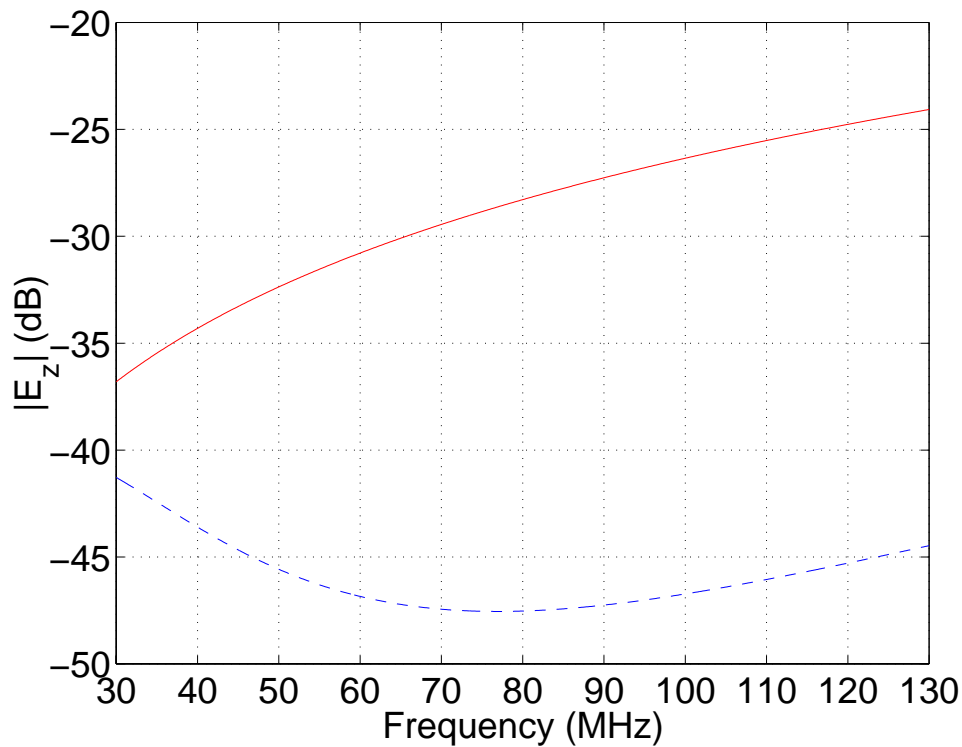
Figure 2.9: Comparison of the magnitude of the frequency response of the direct field (————) to total field ($- - - -$), for a vertical ($\hat{z}$) dipole located at the origin, 2.0m above the impedance surface ($x_0 = y_0 = 0, z_0 = 2.0m$) with real permittivity $\varepsilon'_r = 22.0$, conductivity $\sigma = 8 \times 10^{-2}$. Frequency sweep is from 30 to 130 MHz in steps of 142.86 KHz. Observation is also 2.0m above the surface along the $\phi = 0$ (x axis) and $300m$ from the source ($D = 300m$).

magnitude of the frequency response for the total field is monotonic and slowing varying while the phase is essentially linear and almost identical to the phase of the direct field. The phase behavior indicates that there is little or no dispersion of the broadband signal in
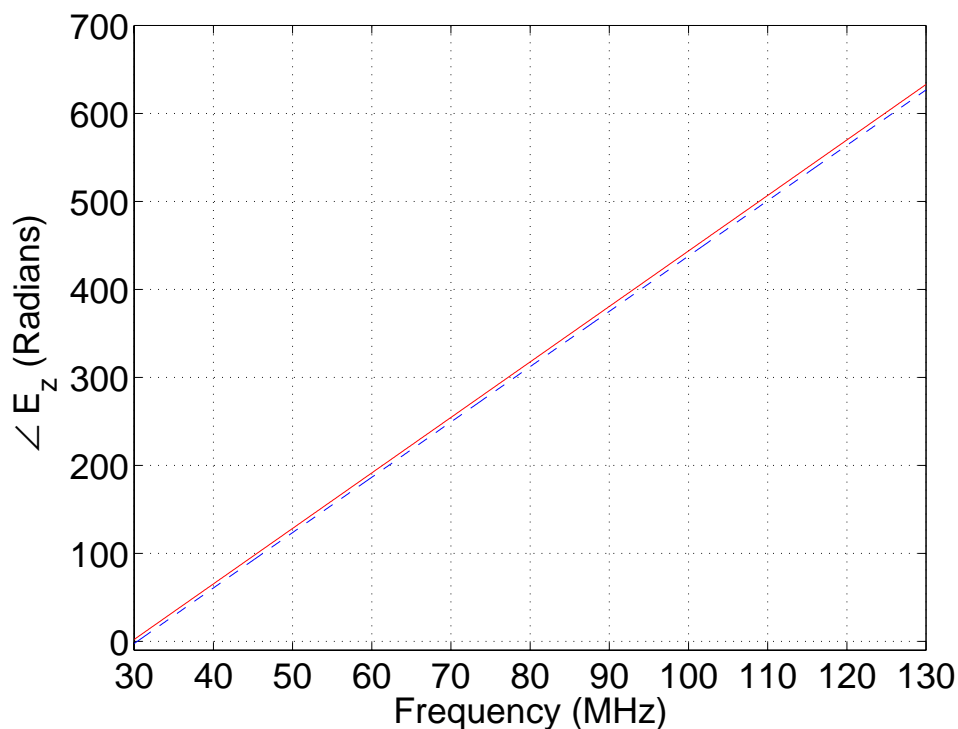
Figure 2.10: Comparison of the phase of the frequency response of the direct field (————) to total field ($-$ $-$ $-$ $-$) (in radians), for a vertical ($\hat{z}$) dipole located at the origin, 2.0m above the impedance surface ($x_0 = y_0 = 0, z_0 = 2.0m$) with real permittivity $\varepsilon'_r = 22.0$, conductivity $\sigma = 8 \times 10^{-2}$. Frequency sweep is from 30 to 130 MHz in steps of 142.86. Observation is also 2.0m above the surface along the $\phi = 0$ (x axis) and 300m from the source ($D = 300m$)

such communications channels. This was found to be true for various complex impedances corresponding to different moisture content, with the exception of the case of either source or observation raised above the surface to a point where there is a significant difference in path delay between the direct and ground (diffracted) waves.

2.4   Chapter Summary: Exact Image Theory

In this chapter the effects of a lossy, homogeneous flat earth on a propagating radio wave was analyzed. Starting with a spectral domain representation of the fields of an infinitesimal dipole above an impedance half space, the highly oscillatory Sommerfeld type integrals

39

inherent in the original formulation, were transformed into a form more conducive to numerical computation. By application of exact image theory, the convergence properties of these integrals are improved to a degree making them practical for numerical computation in their rigorous form. The Sommerfeld expressions are written in terms of zero*th* order Bessel functions of the first kind, and the reflection coefficients cast in the form of a simple Laplace transform of an exponential function. Where necessary terms are expanded by partial fractions so they can be expressed in this form. Order of integration is then exchanged and the inverse transform from the spectral domain performed analytically. The remaining expressions consist of integrals whose integrand is dominated by a decaying exponential, and exhibit rapid convergence qualities. Numerical evaluation of these integrals show good agreement with results obtained by numerical evaluation of the Sommerfeld type integrals, while exhibiting a speed up in computation time of several orders of magnitude.

Having formulated a practical method for the efficient and accurate calculation of the dipole fields above a homogeneous impedance surface, it is now desired to include the effects of an impedance transition as might be caused by a river or land/sea interface in a locally flat earth. In the next chapter this effect is accounted for by applying a perturbation technique in the Fourier domain to solve for unknown surface currents. The method to be described in Chapter 3 is valid for any general one-dimensional impedance transition, where the Fourier transform of the impedance transition function exists.

CHAPTER 3

Fields of an Infinitesimal Dipole Above an Impedance Surface: Effect of an Impedance Transition

In the previous chapter the effects of a homogeneous impedance surface on the fields of an infinitesimal dipole were determined in a more efficient fashion by application of exact image theory to the original spectral domain expressions, in the form of Sommerfeld type integrals. In this chapter the model is extended to account for the effects of a general one-dimensional impedance transition on the dipole fields. This transition in an otherwise homogeneous surface can be representative of a river, trough, or land/sea interface. The problem of plane wave excitation is first solved and then extended to that of dipole excitation in the standard way by representation of the dipole fields as a continuous spectrum of plane waves. To derive the model an integral equation is first formulated in the Fourier domain, and then solved iteratively using a perturbation technique. An analytical solution is provided to any desired order in terms of multi-fold convolution integrals of the Fourier transform of the impedance function. For far-field observation the resulting integrals are solved by applying standard saddle point techniques, resulting in expressions for the induced surface currents which are algebraic to first order in the perturbation series. Also, an error bound for the perturbation parameter is established and defined in terms of incident wave polarization and angle. The method is first validated by comparison with Geometri-

cal Theory of Diffraction (GTD) techniques for an abrupt impedance transition (step insert) and plane wave excitation. Effects of varying both the width of the insert and perturbation parameter of the insert are discussed as well as the effect of oblique incidence and a more gradual transition on the scattered fields. The technique is then integrated with that of the previous chapter for a homogeneous surface, and the effect of a seashore or land/sea transition on the total fields of an infinitesimal dipole are examined. Note that, as previously discussed, the effect of the transition on the total dipole fields is defined as the scattered fields, while the effects of the homogeneous surface is defined as the diffracted fields.

3.1   Introduction: Impedance Transition

In order to completely characterize the fields of an infinitesimal dipole above a lossy Earth, the effects of any impedance transition or inhomogeneity, such as caused by a river or land/sea interface must be accounted for. For non-canonical problems it is usually difficult to obtain exact solutions for Maxwell's equations and thus approximate solutions are sought. GTD methods, while accurate at high frequencies, have only been applied to problems where abrupt variations in a surface are present. The problem of coastal diffraction was originally examined by Clemmow [26], however he did not consider the case of impedance junctions and was not able to derive closed form expressions for the relevant split functions. Maliuzhinets was the first to consider two impedance junctions as a special case of wedge diffraction [27] and the simpler dual-integral equation method can also be employed [4]. The problem of plane wave diffraction from shorelines in planar land-sea boundaries, using the Wiener-Hopf technique, was addressed by Bazer et al. [28]. For this canonical geometry the sea and land surfaces were modeled by a perfectly conducting and impedance surface respectively, and the diffraction is evaluated using the Wiener-Hopf method. Wait and others addressed the diffraction effects caused by an inhomogeneous surface using an integral equation technique to solve for an attenuation factor [29, 30, 31].

This solution can be shown to be equivalent to a Physical Optics (PO) solution, and is formulated in terms of integrals which must be solved numerically.

An analytic solution is sought for problems with a more general variation across the impedance surface, and with arbitrary dimensions compared to the wavelength. Sarabandi presented an analytic technique for the 2-D problem of a resistive sheet when excited by a plane wave, and with one-dimensional variation in the resistivity [32]. In [32] it was shown that the method could be extended to that of an impedance sheet by simply replacing the resistivity with the complex impedance divided by a factor of two. In this chapter the method is extended to account for the scattering caused by a general one-dimensional impedance transition in an otherwise homogeneous impedance surface when excited by a small dipole of arbitrary orientation. To derive the formulation for small dipole excitation the method of [32] for plane wave excitation is first extended to include arbitrary incidence angles. The technique is then extended to that of small dipole excitation in the usual fashion by representing the incident dipole fields in their spectral domain form as an infinite spectrum of plane waves.

When the actual solution of a problem varies only slightly (is perturbed) from a known exact solution, perturbation theory is a viable approach to solve these general problems. In this chapter a perturbation technique is applied to determine an analytic solution to the scattering from a surface impedance transition of arbitrary profile, such as rivers, shorelines, or troughs, when excited by a small dipole of arbitrary orientation. Basically the transition is modeled as an impedance transition in an infinite impedance plane, representing the ground plane, which as previously noted, is an acceptable approximation over a frequency range including HF to lower microwave frequencies. An integral equation is defined on the surface for plane wave excitation, and which assumes a one dimensional impedance variation only. Unknown induced surface currents are expanded in terms of a perturbation series in powers of surface impedance Z_1, where Z_1 is the impedance of the unperturbed surface (homogeneous surface as defined in the last chapter). To facilitate the analysis,

43

the integral equation is transformed to the Fourier domain and from this, recursive expressions for the induced surface current of any order are derived. The resulting expressions are analytic and valid for any general one-dimensional impedance transition for which the Fourier transform exists. The formulation is then extended to that of small dipole excitation by representing the dipole fields as a continuous spectrum of plane waves. For source and observation distant from the transition saddle point techniques are applied to solved the radiation integrals. Resulting expressions are algebraic to first order in the perturbation series.

To validate the technique, results, up to second order in the perturbation series, are generated for plane wave excitation across a step insert and compared to a third order GTD solution [33]. The effects of varying both the perturbation parameter and insert width are discussed. Results are then given for plane wave excitation at various oblique angles. Results from both an impedance step insert and a more gradual impedance transition, better representing a riverbed, are also compared. The effects of a land/sea transition on the total fields of a dipole are then examined, where it is shown that the effects of the transition on the total fields is significant for observation distances far from the transition and independent of the gradient of the transition when both source and observation are near the impedance surface.

3.2 Plane Wave Excitation

3.2.1 Integral Equation Formulation

The geometry of the problem is as shown in Figure 3.1 with θ and ϕ as defined in standard spherical coordinates. In all equations superscript i and s denote parameters of the incident or scattered fields, respectively, and primed and unprimed coordinates reflect as usual the Green's function source and observation coordinates, respectively.

Noting that the geometry is uniform in y and thus the propagation constant of the scat-

tered field must match that of the incidence field along the *y* dimension, thus the scattered field field can only exist along the specular cone as is seen in Figure 3.1. As previously men-
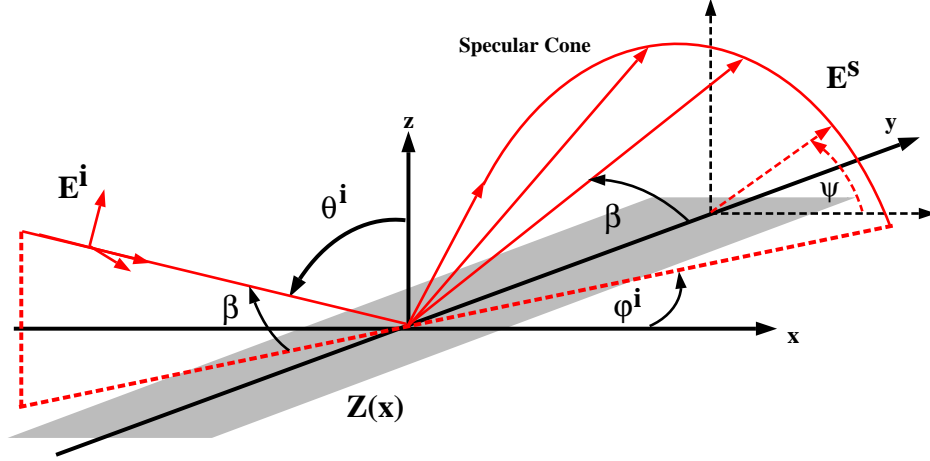
Figure 3.1: Scattering geometry for variable impedance surface.

tioned the assumption is of a lossy Earth, which is a highly conductive, dielectric medium, and thus the standard impedance boundary condition (SIBC) $(\hat{n} \times \hat{n} \times \mathbf{E}) = -Z(x)(\hat{n} \times \mathbf{H}))$ is applied, where $Z(x)$ is the impedance parameter as a function of *x*. The field equivalence principle allows the tangential magnetic field in the SIBC to be replaced by an equivalent electric current, $\mathbf{J} = (\hat{n} \times \mathbf{H})$, and as the fields of interest are in the upper half-space the impedance surface can be replaced with a magnetic wall, doubling the electric currents and eliminating the need to account for magnetic currents. This results in the following implied integral equation for the total electric fields, evaluated on the impedance surface ($z = 0$).

$$\mathbf{E}^T = (\mathbf{E}^i + \mathbf{E}^r + \mathbf{E}^s)\,|_{z=0} = Z(x)\mathbf{J}(x), \tag{3.1}$$

where the superscripts $T, i, r,$ and s are indicative of the total, incident, reflected, and scattered fields, respectively. The scattered field in (3.1) is explicitly written as,

$$\mathbf{E}^s = 2ik_0 Z_0 \int\limits_{-\infty}^{+\infty} \overline{\overline{G}}_{2D\perp}(\rho,\rho') \cdot \mathbf{J}(x')\,dx', \tag{3.2}$$

45

where $\overline{\overline{G}}_{2D\perp}(\rho,\rho')$ is the spectral domain representation of the 2D Dyadic Green's function, for $z > z'$, evaluated on the impedance surface at $z = z' = 0$ and given by

$$\overline{\overline{G}}_{2D\perp}(\rho,\rho') = e^{ik_y^i y}\,\frac{i}{4\pi}\int\frac{1}{k_z}\,[\hat{e}\hat{e}+\hat{m}\hat{m}]e^{ik_x(x-x')}\,dk_x, \qquad (3.3)$$

and where the factor of 2 in (3.2) is from image theory. (Interested readers are referred to Appendix B for the derivation of $\overline{\overline{G}}_{2D\perp}(\rho,\rho')$). In (3.3), $\rho = x\hat{x}+z\hat{z}$ and $k_z = \sqrt{k_0^2 - k_y^{i\,2} - k_x^2} = \sqrt{k_0^2\sin^2\beta - k_x^2}$ with β defined by $\hat{k}^i\cdot\hat{y} = \cos\beta = \sin\theta^i\sin\phi^i$. The unit vectors, $\hat{e}$ and $\hat{m}$, in (3.3) are given by

$$\hat{e} = \frac{\hat{k}\times\hat{y}}{|\hat{k}\times\hat{y}|} \qquad \text{and} \qquad \hat{m} = \hat{e}\times\hat{k}. \qquad (3.4)$$

Noting that $\hat{k} = [k_x\hat{x}+k_y\hat{y}+k_z\hat{z}]/k_0$, simplified expressions for $\hat{e}$ and $\hat{m}$ are given by

$$\hat{e} = \frac{k_x\hat{z}-k_z\hat{x}}{k_0\sin\beta} \qquad \text{and} \qquad \hat{m} = \frac{\hat{y}-\cos\beta\,\hat{k}}{\sin\beta}. \qquad (3.5)$$

In (3.2), $\mathbf{J}(x') = J_x(x')\,\hat{x}+J_y(x')\,\hat{y}$ and a dependency on y of the form $e^{ik_y^i y}$ is assumed and suppressed. Substituting (3.3) into (3.2) it can be shown that

$$\mathbf{E}^s = -2\,\frac{k_0\,Z_0}{4\pi}\iint\limits_{-\infty}^{+\infty}\frac{1}{k_z}\left\{\hat{e}\left[J_x(x')\left(\frac{-k_z}{k_0\sin\beta}\right)\right]+\hat{m}\left[-\cot\beta\,\frac{k_x}{k_0}J_x(x')+\sin\beta\,J_y(x')\right]\right\}$$

$$e^{ik_x(x-x')}\,dk_x\,dx'. $$

$$(3.6)$$

Defining the incident field, $\mathbf{E}^i$ as $\mathbf{E}^i = \mathbf{E}_0\,e^{i\hat{k}^i\cdot\mathbf{r}}$, where $\mathbf{r} = x\hat{x}+y\hat{y}+z\hat{z}$, the incident and reflected tangential electric fields on the surface are given by

$$(\mathbf{E}_{tan}^i + \mathbf{E}_{tan}^r)\,|_{z=0}= 2(\mathbf{E}_0 - (\mathbf{E}_0\cdot\hat{z})\hat{z})e^{i(k_x^i x+k_y^i y)}, \qquad (3.7)$$

46

where again the factor of 2 on the right side of (3.7) is from image theory. The integral equation of (3.1) can now be written explicitly as

$$
\frac{Z(x)}{2}\mathbf{J}(x) = (\mathbf{E}_0 - (\mathbf{E}_0 \cdot \hat{z})\hat{z})\, e^{ik_x^i x} - \frac{k_0\, Z_0}{4\pi} \int\limits_{-\infty}^{+\infty}\!\!\!\int \frac{1}{k_z}\left\{\, \hat{e}\left[J_x(x')\left(\frac{-k_z}{k_0 \sin\beta}\right)\right]\right.
$$
$$
\left. +\hat{m}\left[-\cot\beta\, \frac{k_x}{k_0}J_x(x') + \sin\beta\, J_y(x')\right]\right\}\, e^{ik_x(x-x')}\, dk_x\, dx'. \tag{3.8}
$$

To facilitate analysis (3.8) is transformed to the Fourier domain using the standard definition of a Fourier transform or

$$
\tilde{F}(\alpha) = \int\limits_{-\infty}^{+\infty} f(x)\, e^{-i\alpha x}\, dx, \tag{3.9}
$$

where the overstrike ˜ on any variable implies it is a Fourier domain variable. Applying the Fourier transform to the integrand of (3.8) and recognizing that it is in the form of a convolution integral with respect to x', eliminates the integration with respect to x' in the Fourier domain. The resulting integrand contains a delta function, $\delta(\alpha - k_x)$, allowing the integral with respect to k_x to be evaluated in closed form by applying the sifting property of integrals. Performing these operations on (3.8) and noting that k_z becomes $k_z = \sqrt{k_0^2 - \alpha^2 - k_y^{i\,2}} = \sqrt{k_0^2 \sin^2\beta - \alpha^2}$. the following integral equation in the Fourier domain is obtained

$$
\frac{1}{4\pi}\tilde{Z}(\alpha) * \tilde{J}_x(\alpha) = 2\pi\delta(\alpha - k_x^i)\, (\mathbf{E}_0 - (\mathbf{E}_0 \cdot \hat{z})\hat{z})
$$
$$
- \frac{k_0 Z_0}{2}\frac{1}{k_z}\left\{\hat{e}\left[\frac{-k_z}{k_0 \sin\beta}\, \tilde{J}_x(\alpha)\right] + \hat{m}\left[-\cot\beta\, \frac{\alpha}{k_0}\tilde{J}_x(\alpha) + \sin\beta\, \tilde{J}_y(\alpha)\right]\right\}
$$
$$
\tag{3.10}
$$

Now using the definitions for $\hat{e}$ and $\hat{m}$ given in (3.5), and after some algebraic manipulations, the following integral equations for each current component in the Fourier domain

47

are obtained:

$$\frac{1}{4\pi}\tilde{Z}(\alpha)*\tilde{J}_x(\alpha) = 2\pi\delta(\alpha-k_x^i)(\mathbf{E}_0\cdot\hat{x}) - \frac{k_0 Z_0}{2}\frac{1}{k_z}\left\{\left(1-\frac{\alpha^2}{k_0^2}\right)\tilde{J}_x(\alpha) - \cos\beta\,\frac{\alpha}{k_0}\tilde{J}_y(\alpha)\right\}$$

(3.11)

$$\frac{1}{4\pi}\tilde{Z}(\alpha)*\tilde{J}_y(\alpha) = 2\pi\delta(\alpha-k_x^i)(\mathbf{E}_0\cdot\hat{y}) - \frac{k_0 Z_0}{2}\frac{1}{k_z}\left\{-\cos\beta\,\frac{\alpha}{k_0}\tilde{J}_x(\alpha) + \sin^2\beta\,\tilde{J}_y(\alpha)\right\}$$

(3.12)

3.2.2   Iterative Solution

To obtain an iterative solution for the unknown induced surface currents in (3.11) and
(3.12), the surface impedance $Z(x)$ is first defined in terms of a perturbation parameter,
Δ and expressions are obtained for the zero*th* order currents. These are applied to the
expanded current expressions in (3.11) and (3.12) and after some algebraic manipulation
recursive expressions are obtained which relate successive orders of current in the pertur-
bation series.

Defining the surface impedance, $Z(x)$, in terms of Δ and an impedance transition func-
tion $h(x)$ gives,

$$Z(x) = Z_1(1+\Delta h(x)),$$

(3.13)

where Z_1 is the unperturbed impedance of the homogeneous surface. In the Fourier domain
(3.13) becomes

$$\tilde{Z}(\alpha) = 2\pi Z_1\delta(\alpha) + Z_1\tilde{h}(\alpha)\Delta.$$

(3.14)

Noting that Δ can be complex without loss of generality, for sufficiently small values of Δ

the surface currents in the Fourier domain may be expanded as,

$$\tilde{\mathbf{J}}(\alpha) = \sum_{n=0}^{\infty} \left(\tilde{J}_{nx}(\alpha)\, \hat{x} + \tilde{J}_{ny}(\alpha)\, \hat{y} \right) \Delta^n. \tag{3.15}$$

For the zero*th* order current components, $\tilde{J}_{0x}, \tilde{J}_{0y}$, corresponding to $\Delta = 0$, the impedance function in the Fourier domain becomes, $\tilde{Z}(\alpha) = 2\pi Z_1 \delta(\alpha)$. Substituting this into (3.11) and (3.12) gives the following two integral equations for the x and y components of the surface fields due to the zero*th* order currents in the Fourier domain

$$\frac{1}{2}Z_1 \tilde{J}_{0x}(\alpha) = 2\pi\, E_{0x}\, \delta(\alpha - k_x^i) - \frac{k_0 Z_0}{2}\frac{1}{k_z}\left\{ \left(1 - \frac{\alpha^2}{k_0^2}\right)\tilde{J}_{0x} - \cos\beta\, \frac{\alpha}{k_0}\tilde{J}_{0y}(\alpha) \right\} \tag{3.16}$$

$$\frac{1}{2}Z_1 \tilde{J}_{0y}(\alpha) = 2\pi\, E_{0y}\, \delta(\alpha - k_x^i) - \frac{k_0 Z_0}{2}\frac{1}{k_z}\left\{ -\cos\beta\, \frac{\alpha}{k_0}\tilde{J}_{0x}(\alpha) + \sin^2\beta\, \tilde{J}_{0y}.(\alpha) \right\} \tag{3.17}$$

where $E_{0x} = \mathbf{E}_0 \cdot \hat{x}$ and $E_{0y} = \mathbf{E}_0 \cdot \hat{y}$. Collecting terms in (3.16) and (3.17) and solving for $\tilde{J}_{0x}, \tilde{J}_{0y}$ gives the following expressions for the zero*th* order currents:

$$\tilde{J}_{0x}(\alpha) = \frac{\{E_{0x}[\frac{1}{2}Z_1 + \frac{k_0 Z_0}{2k_z}\sin^2\beta] + E_{0y}[\frac{Z_0\alpha}{2k_z}\cos\beta]\}\, 2\pi\delta(\alpha - k_x^i)}{[\frac{1}{2}Z_1 + \frac{k_0 Z_0}{2k_z}(1 - \frac{\alpha^2}{k_0^2})][\frac{1}{2}Z_1 + \frac{k_0 Z_0}{2k_z}\sin^2\beta] - \left(\frac{Z_0\alpha\cos\beta}{2k_z}\right)^2}, \tag{3.18}$$

$$\tilde{J}_{0y}(\alpha) = \frac{\{E_{0y}[\frac{1}{2}Z_1 + \frac{k_0 Z_0}{2k_z}(1 - \frac{\alpha^2}{k_0^2})] + E_{0x}[\frac{Z_0\alpha}{2k_z}\cos\beta]\}\, 2\pi\delta(\alpha - k_x^i)}{[\frac{1}{2}Z_1 + \frac{k_0 Z_0}{2k_z}(1 - \frac{\alpha^2}{k_0^2})][\frac{1}{2}Z_1 + \frac{k_0 Z_0}{2k_z}\sin^2\beta] - \left(\frac{Z_0\alpha\cos\beta}{2k_z}\right)^2} \tag{3.19}$$

Note that the fields generated by these currents are the same fields calculated in Chapter 2 by exact image theory, i.e., the effect of the homogeneous impedance surface.

To derive the recursive relationship for the x component of the higher order currents (and noting that a similar derivation is used to derive the y component) the perturbed

impedance of (3.14) and the current expansion of (3.15) is applied to (3.11) resulting in the following expression

$$\sum_{n=0}^{\infty} \left(\frac{1}{2} Z_1 \tilde{J}_{nx}(\alpha) \Delta^n + \frac{1}{4\pi} Z_1 \tilde{h}(\alpha) * \tilde{J}_{nx}(\alpha) \Delta^{n+1} \right) = 2\pi E_{0x} \delta(\alpha - k_x^i)$$
$$- \frac{k_0 Z_0}{2} \sum_{n=0}^{\infty} \frac{1}{k_z} \left\{ \left(1 - \frac{\alpha^2}{k_0^2} \right) \tilde{J}_{nx}(\alpha) - \cos\beta \, \frac{\alpha}{k_0} \tilde{J}_{ny}(\alpha) \right\} \Delta^n.$$

(3.20)

Rearranging the terms gives

$$\frac{1}{2} Z_1 \tilde{J}_{0x}(\alpha) + \sum_{n=0}^{\infty} \left(\frac{1}{2} Z_1 (\tilde{J}_{(n+1)x}(\alpha) + \frac{1}{2\pi} \tilde{h}(\alpha) * \tilde{J}_{nx}(\alpha) \right) \Delta^{n+1}$$
$$= 2\pi E_{0x} \delta(\alpha - k_x^i) - \frac{k_0 Z_0}{2} \frac{1}{k_z} \left\{ \left(1 - \frac{\alpha^2}{k_0^2} \right) \tilde{J}_{0x}(\alpha) - \cos\beta \, \frac{\alpha}{k_0} \tilde{J}_{0y}(\alpha) \right\}$$
$$- \frac{k_0 Z_0}{2} \sum_{n=0}^{\infty} \frac{1}{k_z} \left\{ \left(1 - \frac{\alpha^2}{k_0^2} \right) \tilde{J}_{(n+1)x}(\alpha) - \cos\beta \, \frac{\alpha}{k_0} \tilde{J}_{(n+1)y}(\alpha) \right\} \Delta^{n+1}.$$

(3.21)

Observing that (3.16) is embedded in (3.21) all terms containing zero*th* order current components vanish. Noting that the equality remaining must hold for like powers of Δ, the following relationship is established for the *x* current component:

$$\frac{1}{2} Z_1 \tilde{J}_{(n+1)x}(\alpha) = - \frac{1}{4\pi} Z_1 \tilde{h}(\alpha) * \tilde{J}_{nx}(\alpha)$$
$$- \frac{k_0 Z_0}{2} \frac{1}{k_z} \left\{ \left(1 - \frac{\alpha^2}{k_0^2} \right) \tilde{J}_{(n+1)x}(\alpha) - \cos\beta \, \frac{\alpha}{k_0} \tilde{J}_{(n+1)y}(\alpha) \right\}$$

(3.22)

Similarly, for the *y* current component

$$\frac{1}{2} Z_1 \tilde{J}_{(n+1)y}(\alpha) = - \frac{1}{4\pi} Z_1 \tilde{h}(\alpha) * \tilde{J}_{ny}(\alpha)$$
$$- \frac{k_0 Z_0}{2} \frac{1}{k_z} \left\{ - \cos\beta \, \frac{\alpha}{k_0} \tilde{J}_{(n+1)x}(\alpha) + \sin^2\beta \, \tilde{J}_{(n+1)y}(\alpha) \right\}.$$

(3.23)

Collecting terms and solving (3.22) and (3.23) for the higher order current components

gives the following recursive relationship between successive orders of current, in the Fourier domain,

$$\tilde{J}_{(n+1)x}(\alpha) =$$

$$\frac{1}{2\pi} \left[\frac{\left(\frac{k_z\eta}{k_0}\right)\left[\left(\frac{k_z\eta}{k_0}\right) + \sin^2\beta\right]\tilde{h}(\alpha) * \tilde{J}_{nx}(\alpha) + \frac{k_z\eta}{k_0}\frac{\alpha}{k_0}\cos\beta\,\tilde{h}(\alpha) * \tilde{J}_{ny}(\alpha)}{\left(1 + \frac{k_z\eta}{k_0}\right)\left\{\frac{\alpha^2}{k_0^2} - \sin^2\beta - \frac{k_z\eta}{k_0}\right\}} \right], \quad (3.24)$$

$$\tilde{J}_{(n+1)y}(\alpha) =$$

$$\frac{1}{2\pi} \left[\frac{\left(\frac{k_z\eta}{k_0}\right)\left[\left(\frac{k_z\eta}{k_0}\right) + \left(1 - \frac{\alpha^2}{k_0^2}\right)\right]\tilde{h}(\alpha) * \tilde{J}_{ny}(\alpha) + \frac{k_z\eta}{k_0}\frac{\alpha}{k_0}\cos\beta\,\tilde{h}(\alpha) * \tilde{J}_{nx}(\alpha)}{\left(1 + \frac{k_z\eta}{k_0}\right)\left\{\frac{\alpha^2}{k_0^2} - \sin^2\beta - \frac{k_z\eta}{k_0}\right\}} \right], \quad (3.25)$$

where η is the normalized surface impedance, previously defined in Chapter 2, and given by $\eta = Z_1/Z_0$.

3.2.3 Scattered Field Expressions: Plane Wave

Once the induced currents are obtained the scattered field expressions for any order current in the perturbation series can be calculated for any observation position by application of the radiation integrals. Recalling that the induced current is of the form, $\mathbf{J}_n(x,y) = \Delta^n \, \mathbf{J}_n(x) \, e^{ik_y^i y}$, the scattered field can be obtained from

$$\mathbf{E}^s(\mathbf{r}) = 2ik_0 Z_0 \Delta^n \int\!\!\!\int\limits_{-\infty}^{+\infty} \overline{\overline{G}}(\mathbf{r},\mathbf{r}') \cdot \mathbf{J}_n(x') \, e^{ik_y^i y'} \, dx' \, dy', \quad (3.26)$$

where $\overline{\overline{G}}(\mathbf{r},\mathbf{r}')$ in (3.26) is the spectral domain representation of the free space dyadic Green's function for $z > z'$ given in Appendix B. Substituting the expressions for $\overline{\overline{G}}(\mathbf{r},\mathbf{r}')$

from Appendix B into (3.26) and integrating first with respect to y' and then k_y gives

$$\mathbf{E}^s(\mathbf{r}) = -\frac{k_0 Z_0 \Delta^n}{2\pi} \iint\limits_{-\infty}^{+\infty} \frac{1}{k_z} e^{i(k_x x + k_y^i y + k_z z)} \{\hat{h}\hat{h} + \hat{v}\hat{v}\} \cdot \mathbf{J}_n(x') e^{-ik_x x'} dx' \, dk_x, \qquad (3.27)$$

where the unit vectors, $\hat{h}, \hat{v}$, in (3.27) are given by

$$\hat{h} = \frac{\mathbf{k} \times \hat{z}}{|\mathbf{k} \times \hat{z}|} = \frac{k_y^i \hat{x} - k_x \hat{y}}{\sqrt{k_x^2 + k_y^{i\,2}}} \qquad (3.28)$$

and,

$$\hat{v} = \frac{1}{k_0} \hat{h} \times \mathbf{k} = \frac{-k_x k_z \hat{x} - k_y^i k_z \hat{y} + (k_x^2 + k_y^{i\,2}) \hat{z}}{k_0 \sqrt{k_x^2 + k_y^{i\,2}}}. \qquad (3.29)$$

Noting that $\int\limits_{-\infty}^{+\infty} \mathbf{J}_n(x') e^{-ik_x x'} dx'$, in (3.27) is simply the Fourier transform of $\mathbf{J}_n(x')$ with $\alpha = k_x$ the final form of the scattered field for plane wave excitation is

$$\mathbf{E}_n^s(\mathbf{r}) = -\frac{k_0 Z_0 \Delta^n}{2\pi} \int\limits_{-\infty}^{+\infty} \frac{1}{k_z} \{\hat{h}\hat{h} + \hat{v}\hat{v}\} \cdot \tilde{\mathbf{J}}_n(k_x) e^{i(k_x x + k_y^i y + k_z z)} \, dk_x, \qquad (3.30)$$

where subscript n defines the order of the perturbation series solution, and $k_z = \sqrt{k_0^2 - k_x^2 - k_y^{i\,2}}$.

3.2.4   Saddle Point Evaluation: Plane Wave Integral

For $\rho = \sqrt{x^2 + z^2} \gg \lambda$, standard saddle point techniques can be used to evaluate the integral in (3.30) [15, 34]. If the slowly varying function $(\{\ \} \cdot \tilde{\mathbf{J}}_n(k_x))$ in 3.30) is non-zero in the vicinity of the saddle or stationary point, stationary phase techniques, equivalent to first order saddle point method, can be applied. Evaluating the exponential function, $f(k_x^i) = k_x x + k_z z$, at it's extrema gives the following expressions for k_x and k_z at the stationary

points,

$$k_x = \sqrt{k_0^2 - k_y^{i\,2}}\cos\psi \triangleq k_\rho^i \cos\psi$$

$$k_z = k_\rho^i \sin\psi,$$

(3.31)

where ψ is the scattering angle defined from the x axis, and positive towards the z axis, in the $x - z$ plane and $k_\rho^i = k_0 \sin\beta$. Applying stationary phase for a one dimensional integral [35] to (3.30) gives the following far zone scattered field expression for plane wave excitation:

$$\mathbf{E}_n^s(\mathbf{r}) = -\frac{k_0 Z_0 \Delta^n}{\sqrt{2\pi k_\rho^i \rho}} \, \{\hat{h}\hat{h} + \hat{v}\hat{v}\} \cdot \breve{\mathbf{J}}_n(k_\rho^i \cos\psi) \, e^{i(k_\rho^i \rho - \frac{\pi}{4})} \, e^{ik_y^i y}, \tag{3.32}$$

where the unit vectors, $\hat{h}, \hat{v}$, in (3.32) are evaluated at the stationary points and are explicitly given at these points by

$$\hat{h} = \frac{\mathbf{k} \times \hat{z}}{|\mathbf{k} \times \hat{z}|} = \frac{-k_\rho^i \cos\psi\,\hat{y} + k_y^i\,\hat{x}}{\sqrt{k_\rho^{i\,2}\cos^2\psi + k_y^{i\,2}}} = \frac{-k_\rho^i \cos\psi\,\hat{y} + k_y^i\,\hat{x}}{\sqrt{k_0^2 \cos^2\psi + k_y^{i\,2}\sin^2\psi}}, \tag{3.33}$$

and,

$$\hat{v} = \frac{1}{k_0}\hat{h} \times \mathbf{k} = \frac{-k_\rho^i k_y^i \sin\psi\,\hat{y} - k_\rho^{i\,2}\sin\psi\cos\psi\,\hat{x} + (k_0^2\cos^2\psi + k_y^{i\,2}\sin^2\psi)\,\hat{z}}{k_0\sqrt{k_0^2\cos^2\psi + k_y^{i\,2}\sin^2\psi}}. \tag{3.34}$$

3.3 Short Dipole Excitation

To extend the perturbation solution to include excitation by a short dipole the incident dipole fields are represented in the form of a continuous spectrum of plane waves. The methods of the previous section for plane wave excitation can then be applied to each spectral component and the resulting expressions simply integrated over the entire dipole spectrum. Again stationary phase techniques (first order saddle point) can be applied to evaluate the resulting integrals when both source and observation are distant from the transition.

53

Consider a short dipole of length l carrying a sinusoidal current of amplitude I_0 and located at $\mathbf{r}_0 = x_0\hat{x} + y_0\hat{y} + z_0\hat{z}$. The field emitted from this dipole at some observation point $\mathbf{r} = x\hat{x} + y\hat{y} + z\hat{z}$ for $z < z_0$ can be expressed as a continuous spectrum of plane waves and is given by

$$\mathbf{E}^i(\mathbf{r}) = \frac{-I_0 l k_0 Z_0}{8\pi^2} \int\!\!\!\int\limits_{-\infty}^{+\infty} \left\{ \frac{1}{k_z^i}[\overline{\overline{I}} - \frac{\mathbf{K}^i \mathbf{K}^i}{k_0^2}] \cdot \hat{l}\, e^{-i\mathbf{K}^i \cdot \mathbf{r}_0} \right\} e^{i\mathbf{K}^i \cdot \mathbf{r}}\, dk_x^i\, dk_y^i, \tag{3.35}$$

where $\mathbf{K}^i = k_x^i \hat{x} + k_y^i \hat{y} - k_z^i \hat{z}$, $k_z^i = \sqrt{k_0^2 - k_x^{i\,2} - k_y^{i\,2}}$, and unit vector $\hat{l}$ indicates the dipole orientation. The integrand of (3.35) can be restated as $\mathbf{E}_0\, e^{i\mathbf{K}^i \cdot (\mathbf{r} - \mathbf{r}_0)}$, where

$$\mathbf{E}_0 = \frac{-I_0 l k_0 Z_0}{8\pi^2} \frac{1}{k_z^i} \left[\hat{l} - \frac{\mathbf{K}^i \cdot \hat{l}\, \mathbf{K}^i}{k_0^2} \right]. \tag{3.36}$$

Recognizing that the integrand describes a plane wave propagating along $\frac{\mathbf{K}^i}{k_0}$ vector and using the linearity property of electromagnetic waves, the scattered field can be expressed as a superposition of scattering from individual plane waves or

$$\mathbf{E}_{dn}^s(\mathbf{r}) = \int\!\!\!\int\limits_{-\infty}^{+\infty} \mathbf{X}(\mathbf{K}^i)\, e^{-i\mathbf{K}^i \cdot \mathbf{r}_0}\, dk_x^i\, dk_y^i \tag{3.37}$$

where the subscript dn indicates the scattered dipole fields from the current of order n in the perturbation series, and $\mathbf{X}(\mathbf{K}^i)$ is the scattered field generated from each spectral component of the dipole, of propagation vector $\mathbf{K}^i$, and given by (3.30).

3.3.1 Stationary Phase Evaluation: Short Dipole

Again considering a situation where distance between source and observation are large compared to wavelength, and also where both are distant from the transition in terms of wavelength, then stationary phase techniques can be used to evaluate the integrals of (3.37). Recognizing that the expression for $\mathbf{X}(\mathbf{K}^i)$ in the far-field of the impedance transition is as

described by (3.32) and substituting this expression into (3.37) gives the following expression for the far-zone scattered fields,

$$\mathbf{E}_{dn}^s(\mathbf{r}) = \iint\limits_{-\infty}^{+\infty} \mathbf{X}(\mathbf{K}^i) \, e^{ik_\rho^i \rho} \, e^{ik_y^i y} \, e^{-i\mathbf{K}^i \cdot \mathbf{r}_0} \, dk_x^i \, dk_y^i, \tag{3.38}$$

where the exponential terms $e^{ik_\rho^i \rho}$ and $e^{ik_y^i y}$ have been factored out of $\mathbf{X}(\mathbf{K}^i)$. Applying stationary phase for two dimensional integrals [36] and noting that the exponential function is given by

$$f(k_x^i, k_y^i) = k_y^i(y - y_0) - k_x^i x_0 + k_z^i z_0 + k_\rho^i \rho, \tag{3.39}$$

the components of $\mathbf{K}^i$ at the stationary points are found to be

$$k_x^i = \frac{-x_0(\rho + \rho_0)}{\rho_0 R_S} \, k_0$$

$$k_y^i = \frac{(y - y_0)}{R_S} \, k_0 \tag{3.40}$$

$$k_z^i = \frac{z_0(\rho + \rho_0)}{\rho_0 R_S} \, k_0,$$

where $\rho_0 = \sqrt{x_0^2 + z_0^2}$ and $R_S = \sqrt{(y - y_0)^2 + (\rho + \rho_0)^2}$. Evaluating (3.38) at the stationary points gives the final form of the scattered electric field for source and observation distant from each other and the transition, or

$$\mathbf{E}_{dn}^s(\mathbf{r}) = \mathbf{X}(\mathbf{K}^i) \frac{2\pi i}{C} \, e^{ik_0 R_S}, \tag{3.41}$$

55

where again $\mathbf{K}^i$ is evaluated at the stationary points. and where

$$C = \sqrt{\frac{\partial^2 f}{\partial k_x^{i\,2}} \frac{\partial^2 f}{\partial k_y^{i\,2}} - \left(\frac{\partial^2 f}{\partial k_x^i \partial k_y^i}\right)^2}. \tag{3.42}$$

Explicit expressions for (3.42) are obtained by evaluating the second derivatives of the exponential function at the stationary point and the resulting expressions are given by,

$$\frac{\partial^2 f}{\partial k_x^{i\,2}} = -\frac{\rho_0^2}{z_0\ k_z^i}, \tag{3.43}$$

$$\frac{\partial^2 f}{\partial k_y^{i\,2}} = -\frac{k_z^{i\,2} + k_y^{i\,2}}{k_z^{i\,3}}\, z_0 - \frac{k_0^2}{[k_0^2 - k_y^{i\,2}]^{3/2}}\, \rho, \tag{3.44}$$

$$\frac{\partial^2 f}{\partial k_x^i \partial k_y^i} = -\frac{k_x^i k_y^i}{k_z^{i\,3}}\, z_0. \tag{3.45}$$

Simplified expressions for $\tilde{\mathbf{J}}_n(k_x)$, where $k_x = k_\rho^i \cos\psi = k_0 \sin\beta \cos\psi$, can be derived by evaluating (3.24) and (3.25) at the stationary points with E_{0x} and E_{0y} in (3.24) and (3.25) defined by (3.36) Recognizing that $\sin\beta = \frac{(\rho + \rho_0)}{R_S}$, $\cos\beta = \frac{y - y_0}{R_S}$, and $k_z = k_0 \sin\beta\ \sin\psi$ the following expression for the induced surface currents in the Fourier domain are obtained.

$$\tilde{J}_{(n+1)x}(\alpha) = \\ -\frac{1}{2\pi} \frac{\eta \sin\beta \left\{[\eta \sin\psi + \sin\beta]\tilde{h}(\alpha) * \tilde{J}_{nx}(\alpha) + \cos\psi\ \cos\beta\ \tilde{h}(\alpha) * \tilde{J}_{ny}(\alpha)\right\}}{(1 + \eta \sin\beta\ \sin\psi)(\eta + \sin\beta\ \sin\psi)}, \tag{3.46}$$

$$\tilde{J}_{(n+1)y}(\alpha) =$$

$$-\frac{1}{2\pi}\frac{\eta\left\{\left[\eta\sin\beta\,\sin\psi+1-\sin^2\beta\,\cos^2\psi\right]\tilde{h}(\alpha)*\tilde{J}_{ny}(\alpha)+\sin\beta\,\cos\beta\,\cos\psi\tilde{h}(\alpha)*\tilde{J}_{nx}(\alpha)\right\}}{(1+\eta\sin\beta\,\sin\psi)\,(\eta+\sin\beta\,\sin\psi)}.$$

$$(3.47)$$

3.3.2 Near-field Observation

For certain cases it is desirable to allow the observation position to move into the near-field of the impedance transition while keeping the source distant, therefore allowing the spectral domain integration over k_x^i, k_y^i in (3.37) to still be performed in an approximate fashion using stationary phase techniques, while the scattered field for a given spectral component, $\mathbf{X}(\mathbf{K}^i)$ in (3.37) is evaluated numerically. In order to evaluate the integration over k_x^i, k_y^i by applying stationary phase techniques, it is necessary to have an explicit expression for the phase function, or high frequency component of the integrand. As the Fourier transform of the current function is slowly varying, this high frequency component is obviously the exponential factor in the integral expression for $\mathbf{X}(\mathbf{K}^i)$ given in (3.30). Analysis shows however, that there is no analytic solution for the stationary points of the dipole fields when the integrand is in this form. An alternate mapping in the complex plane can be applied however as the contour is no longer along the real axis, k_y^i is complex and the integration over y' in (3.26) is no longer straightforward. If however we subtract the stationary points of the integrand in (3.30) (and given in (3.31)) from the exponential factor of (3.30) and add them back, the following expression is obtained

$$\mathbf{E}^s(\mathbf{r}) = -\frac{k_0 Z_0 \Delta^n}{2\pi} \int\limits_{-\infty}^{+\infty} \frac{1}{k_z} \{\hat{h}\hat{h}+\hat{v}\hat{v}\} \cdot \tilde{\mathbf{J}}_n(k_x) e^{i((k_x - k_\rho^i \cos\psi)x++(k_z - k_\rho^i \sin\psi)z)} \, dk_x \, e^{i(k_\rho^i \rho + k_y^i y)},$$

$$(3.48)$$

where $x = \rho\cos\psi$, $y = \rho\sin\psi$, and therefore that $k_\rho^i(\cos\psi\,x + \sin\psi\,y) = k_\rho^i\rho$. Recognizing that the exponential function inside the integrand of (3.48) transitions to zero as the ob-

57

servation moves into the far-field, it is obvious that this function is slowly varying for all observation positions and that the rapidly varying component, $k_\rho^i \rho$ has been factored out of the integrand. The integrand of (3.48) can now be evaluated numerically, while the high frequency phase factor is of the form given in (3.38) and can be evaluated asymptotically, in a similar fashion.

3.3.3 Error Bound

An important feature of the perturbation solution is its convergence properties and it is appropriate at this point to establish some sense of these properties, i.e., for what values of Δ the perturbation expansion of (3.15) converges to the exact solution. To characterize the limits of the perturbation method an error bound is determined on the maximum Δ allowable, for a given incidence angle, and for a particular impedance profile. Analysis of an error bound for the case of plane wave incidence will also give a sense of the convergence of the perturbation series for dipole excitation in cases where one spectral component of the dipole radiation is the dominate excitation. Mathematically this can be shown by finding the radius of convergence of the expanded current series, in terms of the perturbation parameter Δ. Even for a value of $\Delta > 1$ the series will converge if the current coefficients are decreasing for higher orders. Let us first consider a limiting case for which an exact solution exists. This corresponds to a constant perturbation function ($h(x) = 1$) whose Fourier transform is a δ function. Applying this to (3.18) and (3.19), and assuming $\beta = \pi/2$, gives the following forms for the horizontally and vertically polarized currents:

$$\mathbf{J}_{0h}(x) = \frac{[\sin\phi^i \, \hat{x} + \cos\phi^i \, \hat{y}]}{\frac{1}{2}Z_1(1+\Delta) + \frac{Z_0}{2\cos\theta^i}} e^{ik_0 \sin\theta^i (\cos\phi^i x + \sin\phi^i y)}, \qquad (3.49)$$

$$\mathbf{J}_{0v}(x) = [\cos\phi^i \, \hat{x} + \sin\phi^i \, \hat{y}] \frac{\cos\theta^i}{\frac{1}{2}Z_1(1+\Delta) + \frac{Z_0 \cos\theta}{2}} e^{ik_0 \sin\theta^i (\cos\phi^i x + \sin\phi^i y)}, \qquad (3.50)$$

After some algebraic manipulations these equations can be put in the form of

$$\mathbf{J}_{0\ h,v}(x) = K \frac{1}{\upsilon} \cdot \frac{1}{1 + \frac{\Delta}{\upsilon}},$$ (3.51)

where K is some constant parameter and

$$\upsilon = \begin{cases} \frac{1}{\eta \cos \theta^i} + 1 & \text{for } \mathbf{J}_{0h}(x), \\ \frac{\cos \theta^i}{\eta} + 1 & \text{for } \mathbf{J}_{0v}(x). \end{cases}$$ (3.52)

The Taylor Series expansion of (3.51) will converge uniformly for all $\Delta < \upsilon$, which indicates that the radius of convergence for low impedance surfaces can be very high.

3.4   Validation & Results: Perturbation Technique

In this section analytic results based on the perturbation solution are validated and are compared with those obtained from independent techniques where possible. The impedance values of the soil are again derived from the values of permittivity and conductivity given by Hipp [1] for San Antonio Gray Loam with a density of 1.4 g/cm^3 and shown in Table 1.1, with the impedance values of the water derived from the equations for complex permittivity given by Ulaby, *et al.* [5], as previously stated. Once the impedance values for the soil and water are determined, the perturbation parameter Δ can be calculated from (3.13).

To validate the perturbation method the case of plane wave excitation is first examined. Results are generated for the case of scattering from an abrupt impedance discontinuity or impedance step insert, which is representative of a river. Effects of varying the perturbation parameter Δ (equivalent to varying soil moisture) are investigated and compared to a GTD solution. Scattering for oblique incidence angles is also analyzed, as well as the effect of varying the insert width. A comparison is made between the scattered fields from an abrupt

discontinuity (insert) to those from a more gradual transition, which can better represent an actual land/water transition. As previously mentioned the effect of a land/sea transition on the total fields of an infinitesimal dipole is then examined.

Note that Figure 3.1, shown previously, describes the scattering coordinates for both types of excitation.

3.4.1   Plane Wave Excitation

In this section results will be shown and discussed for plane wave excitation of the impedance surface. As mentioned, the the impedance transition will initially be modeled as an abrupt discontinuity, or impedance step insert. The step insert will be used to validate and characterize the method by comparing with a GTD solution, normal incidence ($\beta = \pi/2$). Results will then be shown for various oblique incidence angles. A more gradual impedance transition function, which better represents an actual riverbed, will then be described and results compared with that of the step insert. Also the effect of varying the insert width will be discussed. Note that all results for plane wave excitation, show the normalized scattering width, σ^s/λ, around the specular scattering cone, with $\sigma^s = 2\pi\rho(|\mathbf{E}^s|/|\mathbf{E}^i|)$ as $\rho \to \infty$.

As a validation of the proposed technique, it is important to know for what values of Δ a first order solution will give desirable accuracy. With this in mind results were generated for first and second order scattered fields using the perturbation method and compared to a third order GTD solution for the step impedance function, for the 2-D case of excitation across the insert ($\phi^i = 180°$). The order of the GTD solution describes to what degree diffracted fields are accounted for, i.e., first order are the diffracted fields generated by the incident wave, second order are the diffracted fields generated by these initial diffracted fields interacting with the diffracting edges, etc. All results shown for plane wave excitation are for a step insert 5λ wide, excited at 30MHz and normal incidence ($\beta = \pi/2$). The insert is assumed to have a normalized complex impedance of $0.0369 - i0.0308$, represen-

tative of saline water, with a salt content of $4pp/1000$, and results are shown for varying soil moistures (gravimetric moisture content). Figures 3.2 and 3.3 show results from the first and second order perturbation solution, compared to the mentioned GTD solution, for TE and TM cases, respectively (TE, TM, transverse electric and magnetic to z) and for gravimetric soil moistures of 20, 10, and 5%, equivalent to normalized impedance η of $0.12 - i0.07$, $0.15 - i0.09$, $0.3 - i0.1$, and $|\Delta| = 0.6529$, 0.7263, 0.8594, respectively, with incidence angle θ^i at $45°$. As soil moisture is varied from 20% to 5% the first and second

(a) Moisture Content = 20%, $|\Delta| = 0.6529$

(b) Moisture Content = 10%, $|\Delta| = 0.7263$

(c) Moisture Content = 5%, $|\Delta| = 0.8594$
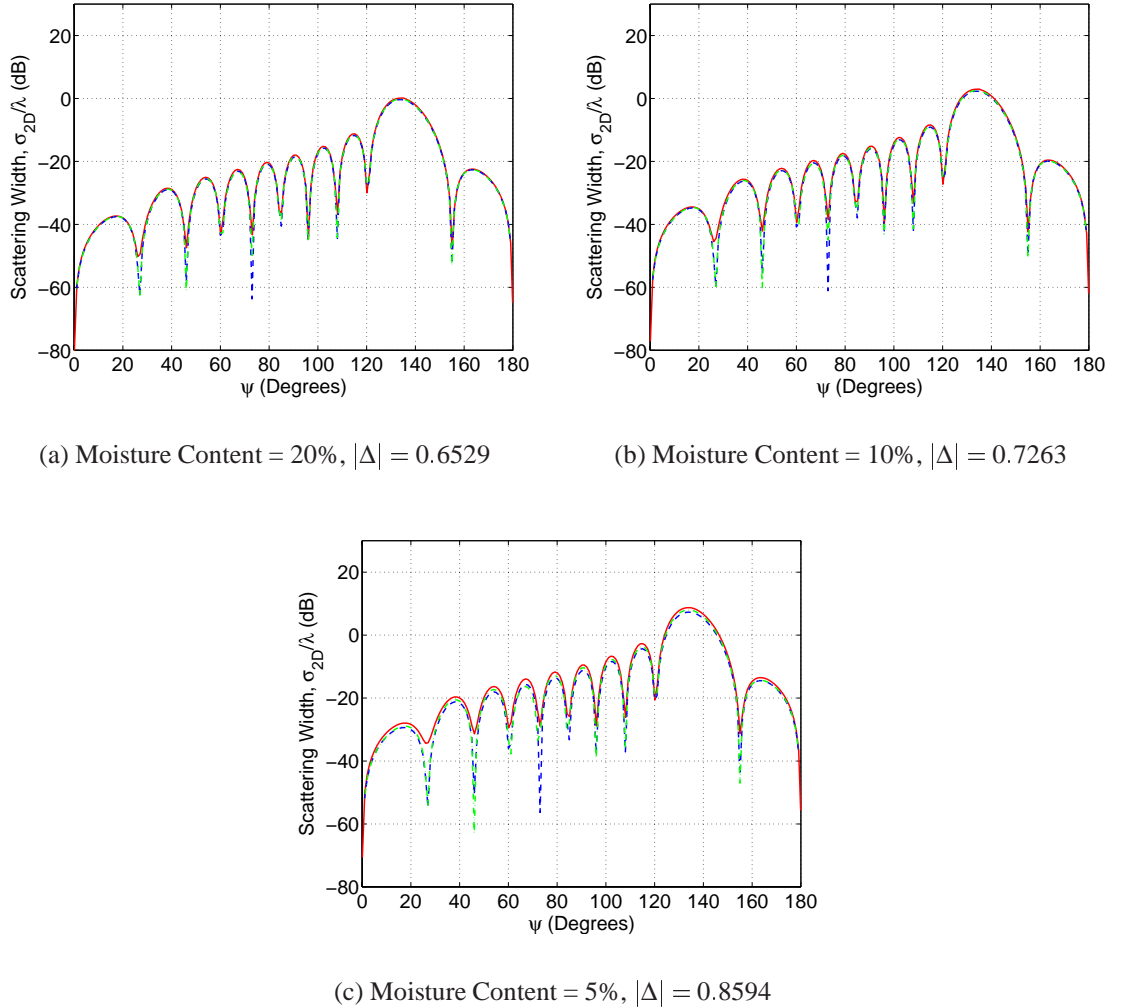
Figure 3.2: TE case, normalized bistatic echo width (σ^s/λ) of an impedance step insert, 5λ wide, equivalent to slightly saline water ($4pp/1000$ salt content, $\eta = 0.0369 - i0.0308$). $\theta^i = 45°$, $\phi^i = 180°$, first (- - - - -) and second order ($-\cdot-\cdot-$) perturbation technique compared with GTD (———) for varying soil moisture.

order perturbation solutions begin to degrade in accuracy. The degradation is especially significant for the TM case and near grazing observation.

The convergence property of the perturbation solution as a function of the width of the insert step function was also observed. The insert width was varied from 1 to 20λ with the accuracy of both the TM and TE results essentially insensitive to insert width variations.

(a) Moisture Content $= 20\%$, $|\Delta| = 0.6529$

(b) Moisture Content $= 10\%$, $|\Delta| = 0.7263$

(c) Moisture Content $= 5\%$, $|\Delta| = 0.8594$
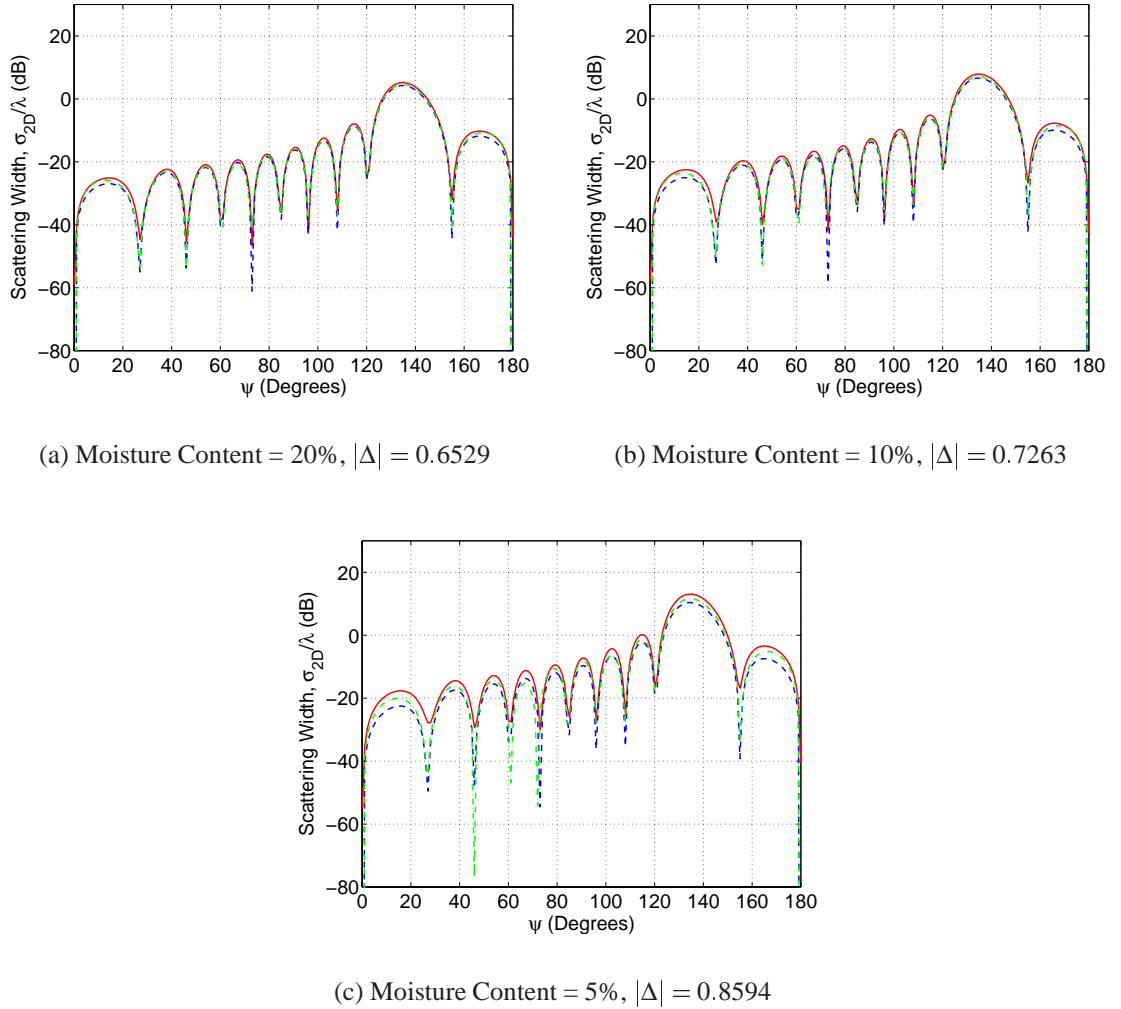
Figure 3.3: TM case, normalized bistatic echo width (σ^s/λ) of an impedance step insert, 5λ wide, equivalent to slightly saline water ($4pp/1000$ salt content, $\eta = 0.0369 - i0.0308$). $\theta^i = 45°$, $\phi^i = 180°$, first (- - - - -) and second order ($- \cdot - \cdot -$) perturbation technique compared with GTD (————) for varying soil moisture.

The effect of oblique incidence on the scattered wave was also examined for the case of the impedance step insert when excited by a plane wave. First order perturbation re-

sults were generated with the insert again representative of slightly saline water and the surrounding impedance representative of the same San Antonio gray loam, with a moisture content of 10%. Figure 3.4 shows the bistatic scattering width for co-polarization results, with 3.4a showing the TE case and 3.4b the TM case. Figure 3.5 shows the cross-polarization results for oblique incidence. Again $\theta^i = 45°$, with ϕ^i rotated at the oblique angles, $180°, 135°$, and $90°$. Referring to Figure 3.4a and Figure 3.4b, the peak scattering
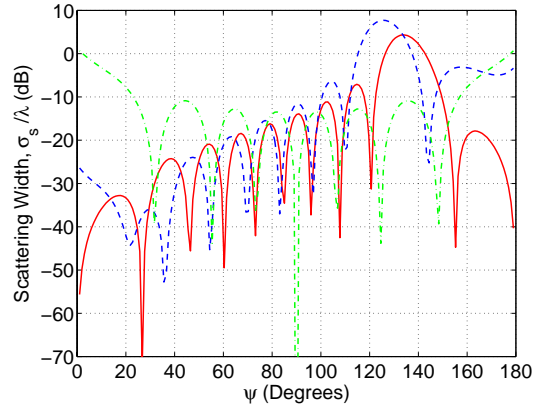
(a) TE case, $\phi^i = 180$ (————), 135 (- - - - -), and $90°$ ($-\,\cdot\,-\,\cdot\,-$).
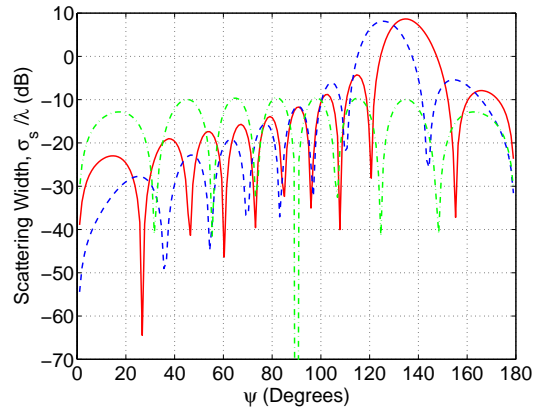
(b) TM case, $\phi^i = 180$ (————), 135 (- - - - -), and $90°$ ($-\,\cdot\,-\,\cdot\,-$).

Figure 3.4: Normalized bistatic echo width, (σ^s/λ), of an impedance step insert of width 5λ, equivalent to slightly saline water ($4pp/1000$ salt content, $\eta = 0.0369 - i0.0308$). Surrounding soil has a gravimetric moisture contend of 10% ($|\Delta| = 0.7263$). Incidence is at $\theta^i = 45°$, first order perturbation technique.

for, $\phi^i = 180°$, is shown to be at approximately the specular angle of $\psi = 45°$. At $\phi^i = 90°$ the incident wave is along the step insert and the scattering pattern is symmetric in the $x - z$ plane as expected.

Theoretically no cross-polarization results can exist for an incidence angle of $\phi^i = 180$. As ϕ^i is rotated towards $90°$ cross-polarization levels become more significant. Figure 3.5 shows cross-polarization results, again in terms of normalized scattering width, for plane wave excitation with $\theta^i = 45°$ and $\phi^i = 90°$. Note that as the incident field is rotated to a position along the step insert, $\phi^i = 90°$, the cross-polarization levels rise and in fact the cross-polarization for TE_{TM} with $\phi^i = 90°$ is the highest level for all results including co-polarization curves. This indicates that receiver polarization (measuring the scattered field) need be adjusted, for optimum polarization matching, as the incident field propagation vector moves about the step insert.
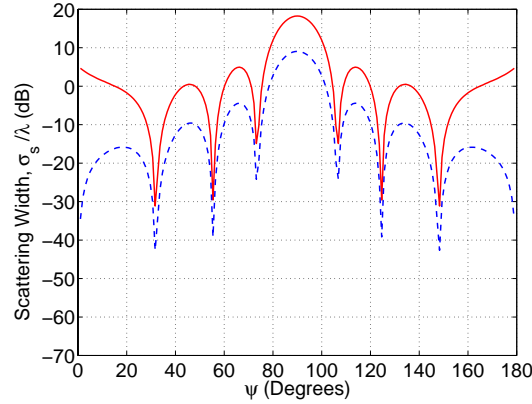
Figure 3.5: Normalized bistatic echo width, (σ^s/λ), of an impedance step insert of width 5λ, equivalent to slightly saline water ($4pp/1000$ salt content, $\eta = 0.0369 - i0.0308$). Surrounding soil has a gravimetric moisture contend of 10% ($|\Delta| = 0.7263$). Incidence is at $\theta^i = 45°$, $\phi^i = 90°$, first order perturbation technique. TE_{TM} (———), TM_{TE} (- - - - -).

In order to more accurately represent an actual riverbed an impedance function with a more gradual transition than the step function was generated and results compared to those generated by the step insert at normal incidence. The transition is made over a distance of $\lambda/2$ and and the width of the gradual impedance function set at 5λ, the same as the step

insert. The width of the gradual impedance function is defined as the distance between points where the function is 3 dB below maximum. Again first order perturbation results are shown with the transition representative of slightly saline water and the surrounding soil having a moisture content of 10%. The results for the step insert, shown previously with $\phi^i = 180°$ are overlayed with those of the gradual impedance transition and are seen in Figure 3.6a and Figure 3.6b for TE and TM polarizations, respectively. As can be seen in
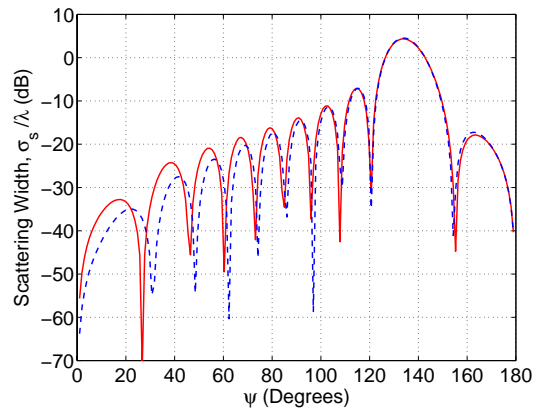
(a) TE case
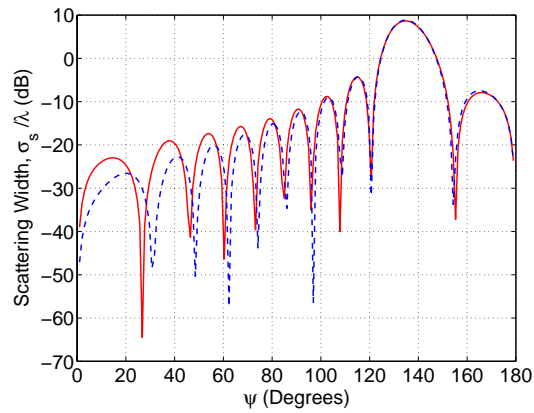
(b) TM case

Figure 3.6: Normalized bistatic echo width, (σ^s/λ), of an impedance step insert of width 5λ, equivalent to slightly saline water ($4pp/1000$ salt content, $\eta = 0.0369 - i0.0308$). Surrounding soil has a gravimetric moisture contend of 10% ($|\Delta| = 0.7263$). Incidence is at $\theta^i = 45°$, $\phi^i = 180°$, first order perturbation technique. Step insert (———) compared to gradual transition (- - - - -).

these figures, the gradual impedance transition tends to lower and pull the side lobe levels towards the specular scattering direction of $\psi = 135°$. This is as expected since a more gradual transition disturbs the induced surface currents less and in the limit should reduce to case of specular scattering only.

3.4.2   Dipole Excitation: Land/Sea Interface

In this section the effect on the total fields of an infinitesimal dipole by an impedance transition will be analyzed. For the case of an impedance step insert, examined in the previous section, the effects of the transition are highly localized to the immediate vicinity of the transition and has little effect on the total dipole fields away from the transition, i.e., the effects of the homogeneous surface dominate here. Instead the case of a seashore, or land/sea transition, which can have a significant effect on the total dipole fields distant from the transition, will be examined. For all results presented in this section the impedance of the land or ground, defined as Z_g will be the usual San Antonio gray loam, with 10% gravimetric moisture content, and equivalent normalized impedance η_g, of $0.15 - i0.09$, while the impedance of the water or sea, defined as Z_w will have a salt content of $4\ pp/1000$ and normalized impedance $\eta_w = 0.0369 - i0.0308$, as previously described. In this section all field quantities shown are defined in terms of path loss, where path loss is the field quantity normalized to the magnitude of the incident dipole field, $\mathbf{E}/|\mathbf{E}^i|$.

To analyze the land/sea transition we will begin with the case of an abrupt transition and then modify the resulting expressions to include the case of a more gradual transition. Referring to Figure 3.7, the impedance transition function for an abrupt land/sea transition can be represented by a signum ($sgn(x)$) function with an offset, where the $sgn(x)$ function

66

is defined as,

$$sgn(x) = \begin{cases} -\frac{1}{2} & \textbf{for } x < 0 \\ \\ \frac{1}{2} & \textbf{for } x > 0, \end{cases} \tag{3.53}$$

Due to the offset of the impedance transition function in the spatial domain, its Fourier
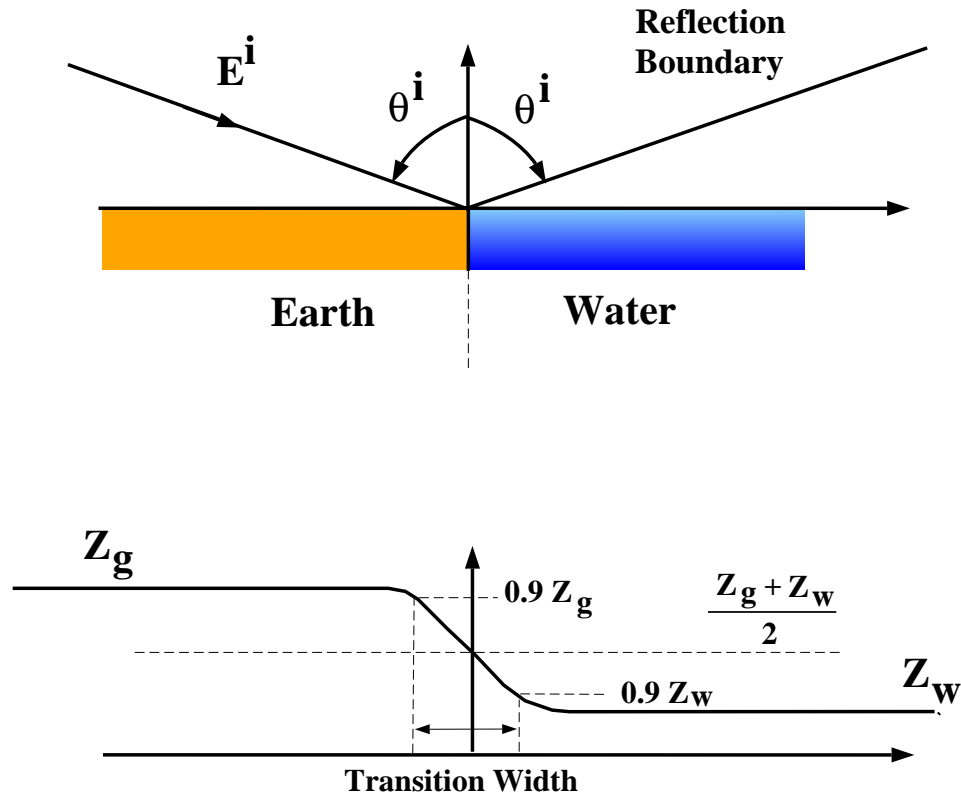
Figure 3.7: Geometry of a Land/Sea Interface

transform contains a δ function, and the perturbation technique described cannot be imme-
diately applied. In order to apply the perturbation technique the impedance transition will
be dealt with in a mean sense, i.e., we assume that the unperturbed impedance Z_1, in (3.13),
is the mean value of the impedance transition function or

$$Z_1 = \frac{Z_g + Z_w}{2}, \tag{3.54}$$

as seen in Figure 3.7. The assumption of a mean impedance as the unperturbed impedance is a valid assumption in terms of the first order and higher fields in the perturbation series. For source and observation near the impedance surface and distant from both each other and the transition the assumption of a mean impedance for the homogeneous surface should also produce the appropriate zero*th* order (diffracted) fields. For this situation, the observation is in the immediate vicinity of the Geometrical Optics (GO) reflection boundary (boundary between GO fields reflected from land and GO fields reflected from the sea, see Figure 3.7) and as in this region higher order terms in the asymptotic expansion of the diffracted fields are dominate (Norton surface wave), there is no sharp transition at the reflection boundary between the fields diffracted from the land and those diffracted from the sea (GO component of the diffracted field is not dominate), and thus the assumption of a mean impedance for the homogeneous surface is valid. As observation and or source are moved away from the impedance surface the dominate component of the diffracted fields is the specular component, and the reflection boundary becomes more sharply defined. In this region the mean impedance assumption, is invalid and the perturbation solution will not produce the correct diffracted fields. For this case however, the space wave (direct+diffracted) is the dominate contributor to the total fields and the diffracted fields can be recovered by simply assuming a sharp reflection boundary and calculating the diffracted fields from land or sea respectively, on either side of this boundary.

The impedance transition function, $h(x)$, can now be written directly as,

$$h(x) = -sgn(x), \tag{3.55}$$

$$\tilde{h}(\alpha) = \frac{i}{\alpha}, \tag{3.56}$$

in the spatial and Fourier domain, respectively. To find the appropriate Δ, (3.54) and (3.55)

68

are substituted into (3.13). Solving for Δ gives,

$$\Delta = \frac{Z_g - Z_w}{Z_1}. \tag{3.57}$$

In order to represent a more gradual transition function, (3.55) is modified to,

$$h(x) = -sgn(x)\left(1 - e^{-\kappa|x|}\right), \tag{3.58}$$

which in the Fourier domain becomes,

$$\tilde{h}(\alpha) = \frac{i}{\alpha} - \frac{i\alpha}{\alpha^2 + \kappa^2}. \tag{3.59}$$

In (3.58) κ is a constant parameter, where $\kappa \to \infty$ as the width of the transition goes to zero, i.e., an abrupt transition.

Before beginning analysis of the land/sea transition it is appropriate to note the introduction of a simple pole in the impedance transition function of (3.56), and therefore in the scattered field integral of (3.30). This pole occurs at the reflection boundary of the GO fields and while it can be shown this is a non-contributing pole care must be taken when evaluating the integral of (3.30) asymptotically. As the stationary point approaches the pole (observation approaches the reflection boundary) the effect of the stationary point cannot be separated from the effect of the pole and modified asymptotic approaches must be employed. In the literature two approaches are discussed, the additive, and multiplicative method [37, 15]. In the additive method the integrand is regularized by subtracting and adding an appropriate factor and the resulting expression expanded in an asymptotic fashion. In the multiplicative method the integrand is regularized, appropriately by a multiplicative factor and also expanded into an asymptotic series. While both expansions can be shown to be equivalent, the equivalence holds only for the complete asymptotic series of both expansions [38]. When the series are truncated the equivalence does not hold and the

truncated series may produce different results. In the analysis of the land/sea problem only the first order term in the asymptotic series is retained and it was observed that the multiplicative method produced proper results, while the additive method did not sufficiently compensate for the immediate presence of the pole, thus implying that higher order terms in the asymptotic expansion are required to utilize this method.

To begin analysis of the land/sea transition we first examine the effect of a gradual transition on the scattered fields. A vertical electric dipole, operating at 30MHz, is placed 100λ from the impedance transition, along the negative x axis and 100λ above the impedance surface ($x_0 = -100\lambda, y_0 = 0, z_0 = 100\lambda$). Observation is across the transition ($y = 0$) at a fixed radial distance of 50λ. Note that for all results in this section the z component of the scattered field is shown. For source and observation near the impedance surface the z scattered field component from a vertical electric dipole is the dominate scattered field component for any dipole orientation, and thus is of most interest in this analysis. Figure 3.8 shows the path loss for transition widths of 0 (abrupt transition), 1, and 10λ, where the transition width is defined as the distance between the points where the transition function is 0.9 that of Z_g or Z_w, over land or sea, respectively (see Figure 3.7). As can be seen in Figure 3.8, the effect of widening the transition is to focus the scattered energy in the specular direction ($\psi' = 135°$, note that $\psi' = (\pi - \psi)$ in the figures shown, $\phi^i = 0$). However, in the neighborhood of the specular direction the transition width has little effect on the field levels. This is a significant observation as it indicates that for source and observation near the surface, and again distant from each other and the transition, the width of the transition will have negligible effect on the scattered fields as in this region the specular angle is pushed to near-grazing observation, i.e., observation is always near the specular point. This makes intuitive sense also as the width of the transition is less apparent as it approaches the horizon of an observer.

In Figure 3.9 a similar problem is analyzed but for this case the transition width is fixed at 1λ and the radial observation distance ρ is varied from 50 to 10 to 1λ. As can be seen in
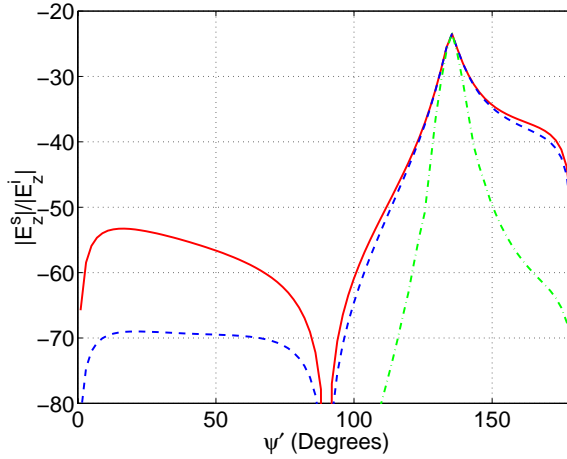
Figure 3.8: Magnitude (dB), Path loss, land/sea transition located at $x = 0$, z component of the scattered fields for a vertical (z-directed) electric dipole. Observation ρ is fixed at 50λ, observation $y = 0$, for dipole position of $x_0 = -100\lambda$, $y_0 = 0$, $z_0 = 100\lambda$. Ground moisture is 10% ($\eta_g = 0.15 - i0.09$), Sea is saline water ($4pp/1000$ salt content, $\eta_w = 0.0369 - i0.0308$, $|\Delta| = 1.14$). Results for transition widths of 0 (———), 1 (- - - - -), and 10λ (— · — · —). Note that $\psi' = \pi - \psi$ in curves.

Figure 3.9 this has the effect of spreading the energy out, around the specular direction. The is indicative of the fact that for far-field observation the induced surface currents around the transition look like a line source, while as observation is moved from far-field to near-field the current distribution begins to look more like a distributed source.

In Figure 3.10 the transition width is fixed at 1λ, observation is fixed at a radial distance of 100λ, with the three curves reflecting an offset of 0, 50, and 100λ in the y dimension (oblique incidence). As can be seen in Figure 3.10 the effect of the obliquity across the transition is to increase the amount of energy in the backscatter direction. This again makes intuitive sense as the energy from the incident wave is coupled into a component along the transition.

As a final analysis of the effects of a land/sea transition on the fields of an infinitesimal dipole, we place a vertical electric dipole at $x_0 = -100\lambda$, $y_0 = 0$, move the source and observation heights to 1, 5, and 10λ (for these examples source and observation are at same height above surface), and compare the path loss of the space wave to that of the total
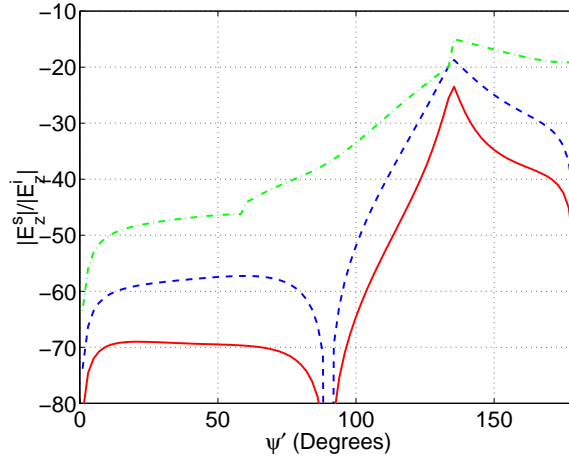
Figure 3.9: Magnitude (dB), Path loss, land/sea transition, located at $x = 0$, z component of the scattered fields for a vertical (z-directed) electric dipole. Transition width is fixed at 1λ, observation $y = 0$, for dipole position of $x_0 = -100\lambda, y_0 = 0, z_0 = 100\lambda$. Ground moisture is 10% ($\eta_g = 0.15 - i0.09$), Sea is saline water ($4pp/1000$ salt content, $\eta_w = 0.0369 - i0.0308$, $|\Delta| = 1.14$). Results for radial observation distance ρ of 50λ (———), 10λ (- - - - -), and 1λ ($- \cdot - \cdot -$). Note that $\psi' = \pi - \psi$ in curves.

fields. Observation is on a radial line between source and observation, from $x = -50\lambda$ to $x = 150\lambda$. Note that other parameters are the same as for previous results in this section, with the transition width at zero (abrupt transition). The results are seen in Figure 3.11, with Figure 3.11a, b, and c, comparing the space wave (direct+diffracted) to the total fields (including the effects of the transition) and showing the results for source/observation heights of 1, 5, and 10λ, respectively. As mentioned for this case of source and observation near the impedance surface the Norton surface wave, which decays at a rate of $1/R^2$, is the dominate component of the diffracted fields. Noting that the scattered fields also decay at this rate it is expected that the effect of the land/sea interface will have a significant effect on the total dipole fields and as is seen in these figures, the effect of the land/sea transition on the total fields is significant even at distances far from the transition. An additional note on the plots in Figure 3.11. An abrupt discontinuity is observed at the reflection boundary ($x = 100\lambda$), where the diffracted fields transition from ground reflections to reflections from the sea. Normally it would be expected that the addition of the scattered fields to the total

Figure 3.10: Magnitude (dB), Path loss, land/sea transition, located at $x = 0$, z component of the scattered fields for a vertical (z-directed) electric dipole. Transition width is fixed at 1λ, Radial observation ρ is fixed at 10λ, for varying y offset between source and observation (oblique incidence), and for dipole position of $x_0 = -100\lambda$, $z_0 = 100\lambda$. Ground moisture is 10% ($\eta_g = 0.15 - i0.09$), Sea is saline water ($4pp/1000$ salt content, $\eta_w = 0.0369 - i0.0308$, $|\Delta| = 1.14$). Results for offset in y of 0 (———), 50 (- - - - -), and 100λ ($- \cdot - \cdot -$). Note that $\psi' = \pi - \psi$ in curves.

fields should produce uniform results across the reflection boundary, i.e., a smooth transition between the fields diffracted from land and those diffracted from water. The abrupt transition observed in these results can be explained by observing the transition function seen in Figure 3.7 and its Fourier transform. The transition function is infinite in extent, and as it is assumed that only one spectral component of the dipole fields excites the transition uniformly across the entire extent of the impedance surface, the transition function contains infinite energy. Thus while its Fourier transform exists, it is not finite in energy, at the reflection boundary. To show this we weight the transition function of (3.55) with a dampening factor, or

$$h(x) = -sgn(x)e^{-\kappa|x|} \qquad (3.60)$$

73

whose Fourier transform is given by,

$$\tilde{h}(\alpha) = \frac{i\alpha}{\alpha^2 + \kappa^2},$$

(3.61)

The scattered fields produced by this transition function are compared to those from the original abrupt transition, for source and observation heights of 1λ, and the results are shown in Figure 3.12. As expected the effect of a dampened transition, with finite energy smoothes the transition in the scattered fields over the reflection boundary. While this result explains the apparent discontinuity in the fields across the reflection boundary it is not apparent that this modification will produce acceptable results. Questions arise as to the appropriate dampening factor to produce physical results. A more appropriate adjustment may be made to the direct dipole fields. In implementing the perturbation technique it is assumed that the dipole source is distant from the transition and that only one spectral component excites the transition. While this is a valid assumption it assumes that one plane wave illuminates the entire impedance surface (infinite energy across the surface), and does not account for the pattern and decay of the dipole fields away from the transition. A more proper solution may be to expand the dipole fields in a way which accounts for the dipole field pattern across the impedance surface. In any case while the abrupt discontinuity across the reflection boundary observed in Figure 3.11 is not in fact physical, the fields on either side of the boundary are proper.

Finally, for the same test case the dipole is placed 1λ above the impedance surface and path loss is observed in a rectangular grid, 1λ above the surface. Note that the transition is located at $x = 0$ in these figures (abrupt transition). Figures 3.13 shows the path loss, with Figures 3.13a showing the space wave and Figures 3.13b showing the total fields. As can be seen in comparing the field plots, the land/sea transition has a significant effect on the total dipole fields.

3.5   Chapter Summary: Impedance Transition

In this chapter the model for scattering and diffraction from an impedance half-space, representing a locally flat, lossy Earth was extended to include an impedance transition such as caused by a river or land/sea interface. Using the field equivalence principle, the problem is formulated in terms of an integral equation for a fictitious electric current induced on the variable impedance surface. A perturbation technique was used to derive a recursive solution for any order surface currents in the perturbation series, in terms of the previous order. An error bound was established to give some sense of the radius of convergence of the perturbation series. Stationary phase techniques were used to evaluate far-field expressions for both plane wave and short dipole excitations. Initial results were shown for plane wave excitation to characterize and validate the perturbation technique. Examining the case of an impedance step insert, results from the perturbation model, for the 2-D case were compared to those of a GTD solution. It was shown that for impedances representative of a river surrounded by moist soil, that the first order perturbation results produced acceptable accuracy when the soil moisture content was at or above 10%. Even for soil moisture levels below 10% the first order perturbation results were acceptable for TE incidence with TM showing a degradation at near-grazing observation angles of 5 or 6 dB. It was observed that, for oblique incidence angles, the cross-polarization levels for a TM polarized field, incident along the river, dominated the scattering levels. Effects of a more realistic, gradual impedance transition were also examined. The effects on the total fields of an infinitesimal electric dipole by a land/sea transition were then examined. Noting that the $\hat{z}$ component of the received electric fields from a vertical dipole are dominate for source and observation near the impedance surface this case was examined. To implement the transition in the Fourier domain the impedance transition was dealt with in a mean sense, which is an acceptable approximation for source and observation near the impedance surface. Results from an abrupt transition were generated and compared to those from a more gradual transition. It was shown that the while a more gradual transition tends to fo-

cus the scattered field energy in the specular direction, the field levels in the neighborhood around specular scattering was essentially unaffected, thus indicating that for source and observation near the impedance surface the effects of the transition width are negligible. Observation of the path loss in the total fields when compared with the path loss of the space wave (direct+diffracted) showed that the land/sea transition has a significant effect on the total dipole fields, even distant from the seashore.

Having developed a complete model in the last two chapters to account for the effects of an impedance half-space, which can contain a general one-dimensional impedance variation, on the propagating radio wave, it is now desired to include the effects of natural obstacles on the propagating wave. With this in mind, in the next two chapters a diffraction model is developed which accounts for the effects on propagation of mountains, hills, or ridgelines, which can be modeled as single curved, convex surface. For obstacles with a large local radius of curvature, diffraction effects can be modeled locally by a right circular cylinder. In the next chapter a somewhat novel model to predict scattering and diffraction from right circular cylinders, when excited by a plane wave at oblique angles is developed. In the chapter that follows the model is extended to include scattering and diffraction from a general, singly curved, convex surfaces.

(a) $z_0 = z = 1\lambda$

(b) $z_0 = z = 5\lambda$

(c) $z_0 = z = 10\lambda$
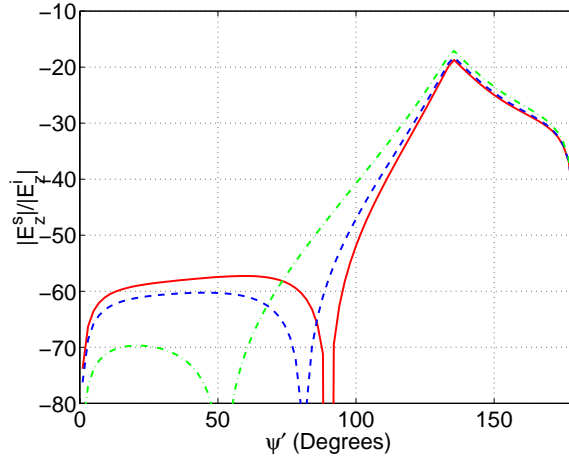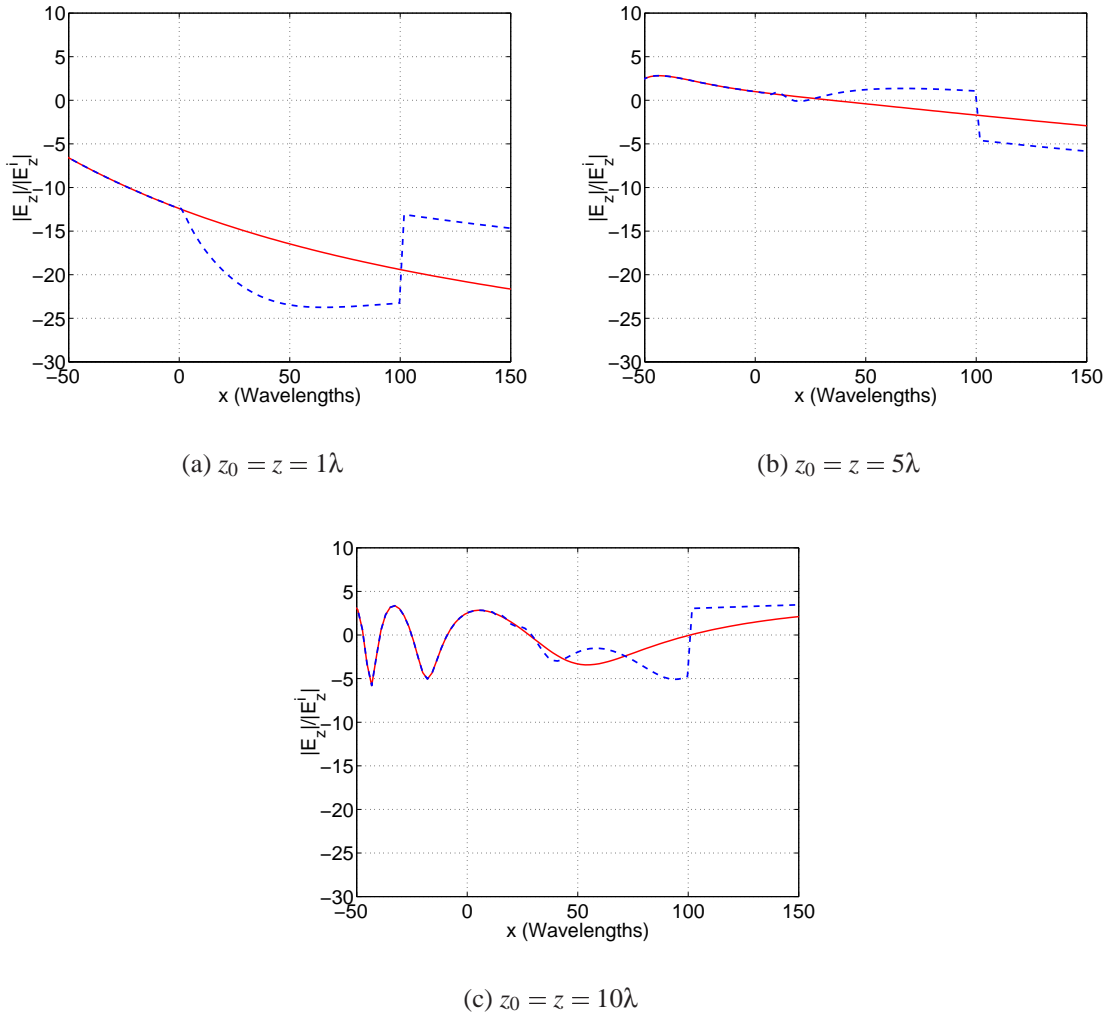
Figure 3.11: Magnitude (dB), Path loss, land/sea transition, located at $x = 0$, z component of the scattered fields for a vertical (z-directed) electric dipole. Transition width is 0λ (abrupt), observation $y = 0$, observation x from -50λ to 150λ. Dipole position is at $x_0 = -100\lambda, y_0 = 0\lambda$. for varying source/observation heights. Ground moisture is 10% ($\eta_g = 0.15 - i0.09$), Sea is saline water ($4pp/1000$ salt content, $\eta_w = 0.0369 - i0.0308, |\Delta| = 1.14$). Results for space wave (———), and total dipole fields (- - - - -).

77
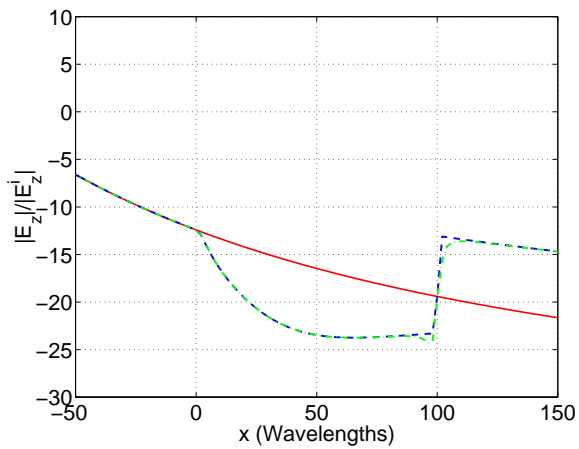
Figure 3.12: Magnitude (dB), Path loss, land/sea transition, located at $x = 0$, z component of the scattered fields for a vertical (z-directed) electric dipole. Transition width is 0λ (abrupt), observation $y = 0$, observation x from -50λ to 150λ. Dipole position is at $x_0 = -100\lambda, y_0 = 0\lambda$. Source/observation height $z_0 = z = 1\lambda$. Ground moisture is 10% ($\eta_g = 0.15 - i0.09$), Sea is saline water ($4pp/1000$ salt content, $\eta_w = 0.0369 - i0.0308, |\Delta| = 1.14$). Results for space wave (———), total dipole fields, infinite transition function (- - - - -), total dipole fields, weighted transition function ($- \cdot - \cdot -$).
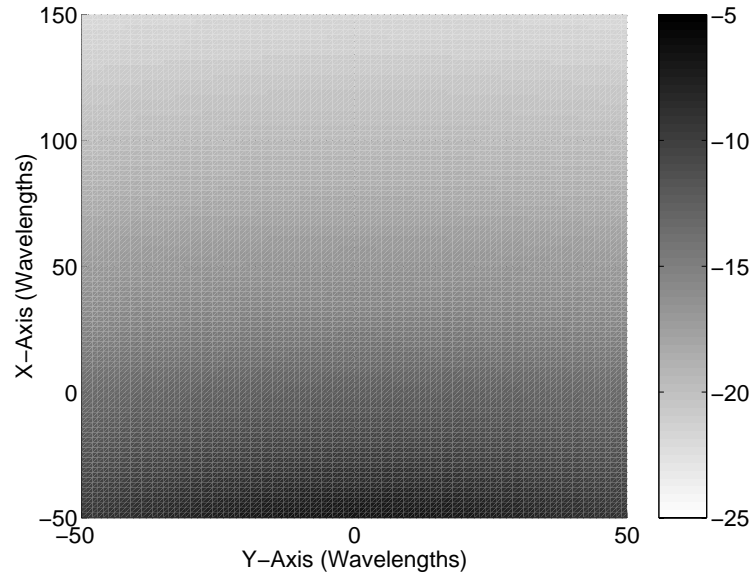
(a) Space wave (direct+diffracted)
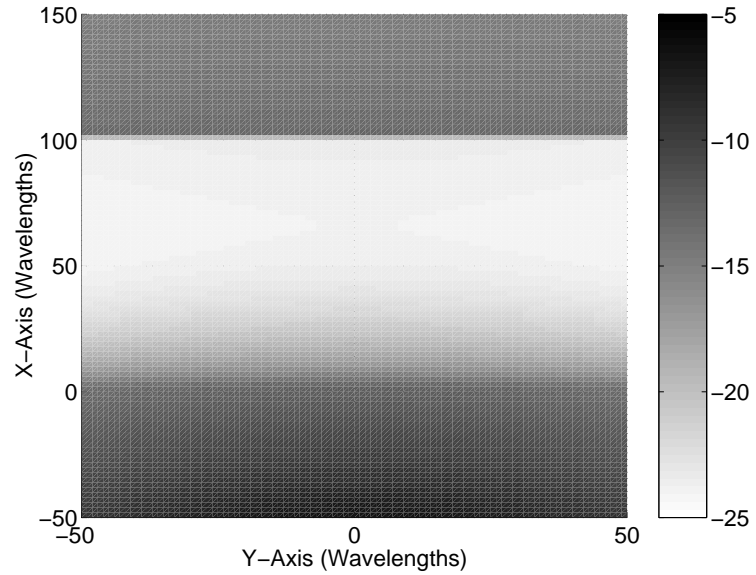
(b) Total fields (direct+diffracted+scattered)

Figure 3.13: Magnitude(dB), Path loss, land/sea transition, located at $x = 0$, z component of the scattered fields for a vertical (z-directed) electric dipole. Transition width is 0λ (abrupt), observation x from -50λ to 150λ, observation y from -50λ to 50λ. Dipole position is at $x_0 = -100\lambda$, $y_0 = 0\lambda$. Source/observation are at $z_0 = z = 1\lambda$. Ground moisture is 10% ($\eta_g = 0.15 - i0.09$), Sea is saline water ($4pp/1000$ salt content, $\eta_w = 0.0369 - i0.0308$, $|\Delta| = 1.14$).

CHAPTER 4

Diffraction from Convex Surfaces: Right Circular Cylinders

In a rural or semi-rural propagation environment, natural obstacles such as hills, mountains, or ridgelines can have a significant effect on the propagating radio wave. Many natural terrain features exhibit both curved and doubly curved surfaces. Ridge lines in mountainous areas exhibit the features of a long curved cylinder which is essentially infinite in one dimension at high-frequencies. These lines may be the result of the natural formation of the mountain chain or a feature of erosion. Geologically recent mountain chains, while exhibiting sharp edged features, still have electrically large radii of curvature even at HF bands. This indicates that the radius of curvature must be accounted for, and that diffraction from curved surfaces, as opposed to knife edge diffraction, is the appropriate prediction tool.

Because of the numerical complexity associated with high frequency methods for convex surfaces, simpler approaches are taken which do not account for the radius of curvature of the diffracting obstacle. One of the most commonly used methods of prediction is knife-edge or Kirchhoff diffraction. This method is an application of Huygens principle in which the diffracting obstacle is replaced by an impenetrable screen and the field distribution in the plane of the screen (aperture) is integrated to produce the fields at the desired

observation point. These integrals are usually in the form of either Fresnel type integrals (intermediate range) or Fourier transforms (far-field observation). This method is simple to implement, and for very narrow hills (small radius of curvature at the shadow boundary) produces acceptable results in the far-field, away from the transition region (transition between light and shadow), however it does not produce acceptable results for near-field observation or in the shadow or transition regions. The method also does not account for polarization effects, nor the shape of the obstacle (does not account for reflections from the obstacle), and it is a 2-D method and therefore does not account for the effects of oblique incidence. Luebbers [39] modeled diffracting obstacles as an impedance wedge and showed a significant improvement over knife-edge techniques. The method is somewhat simple to implement and is extendible to the oblique incidence case, however the accuracy of the method is based on the assumption that the local radius of curvature at the shadow boundary is less than $1/100$ of a wavelength ($r_c \ll \lambda/100$), which as mentioned tends not to occur in nature. In addition the wedge is not a suitable representation for many natural features. These features have a radius of curvature which makes a more gradual transition away from the shadow boundary and creeping wave effects, which the wedge shape does not predict, must be accounted for. For these obstacles, with a more gradual transition in radius near the shadow boundary, wedge diffraction will not produce accurate results in the near-field of the obstacle, especially in the deep shadow region.

With this as a motivation, in the next two chapters a somewhat novel method for the prediction of diffraction and scattering from singly curved convex surfaces, with large, slowly varying radii of curvature is developed. To avoid the aforementioned numerical complexities associated with high-frequency techniques for convex surfaces, a much simpler method is developed, which retains a high degree of accuracy, while avoiding the numerical integration inherent in the existing techniques. The proposed method calculates induced surface currents and thus through the radiation integrals gives accurate fields in all regions around the surface. The induced surface currents on a general convex surface,

81

again of large, slowly varying radius of curvature, can be modeled locally by the currents on a circular cylinder and in this chapter a macromodel for the surface currents induced on right circular cylinders, when excited by a plane wave at oblique angles, is developed. In the next chapter the method is extended to account for the induced currents on a general convex surface by application of known techniques.

In order to develop a macromodel for the induced surface currents on a right circular cylinder of large radius a heuristic approach is applied, based on the Physical Theory of Diffraction (PTD) and Fock analysis. The currents are separated in the fashion of the Physical Theory of Diffraction (PTD) in terms of a uniform or Physical Optics (PO) component and a non-uniform or diffraction component which is highly localized to the shadow boundary. The case of the 2D perfectly electric conducting (PEC) circular cylinder, excited by a plane wave at normal incidence is developed first, and then extended to that of oblique incidence analytically. The resulting expressions for the induced current are algebraic and are shown to be highly accurate for cylinders having radii of curvature larger than a wavelength. Total near fields generated by this macromodeled current are in good agreement with those of the exact solution everywhere.

4.1   Introduction: Diffraction from Convex Surfaces

Current methods for the prediction of scattering and diffraction from convex surfaces can be divided into two categories, those which are valid away from the surface (regions I, II, III in Figure 4.1) and those which are valid near the surface of the object (regions IV, V, VI in Figure 4.1). All of these methods treat the problem of high frequency scattering and diffraction from a general convex surface by applying a solution for a circular cylinder locally, on the convex surface. While the exact solution for a circular cylinder is known [40] the convergence properties of the resulting eigenseries deteriorate as cylinder radius increases, making it impractical for problems of large electrical size and thus alternate

solutions are sought. The convergence properties of this series can be improved by applying a Watson type integral transform [41] and the resulting expressions are the basis for many of the high frequency techniques in use.
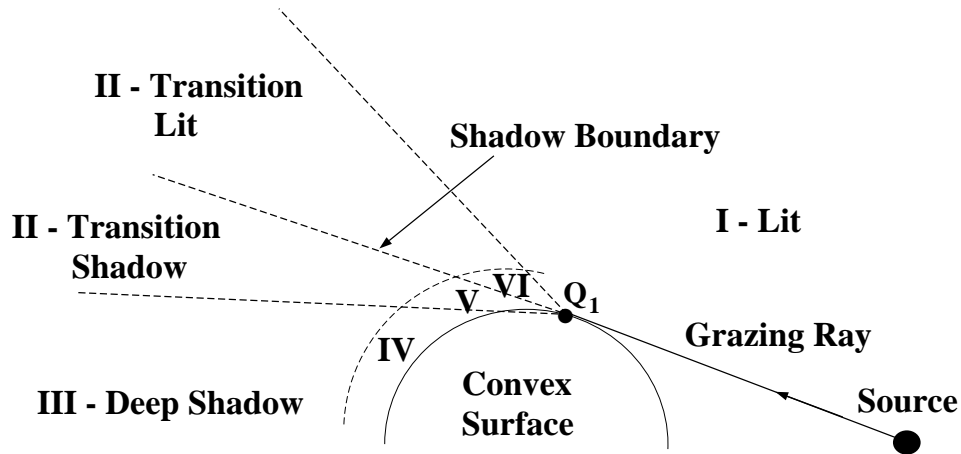
Figure 4.1: Definition of regions around a convex surface.

Geometrical Theory of Diffraction (GTD) and Uniform Geometrical Theory of Diffraction (UTD) solutions are field solutions, valid away from the convex surface. GTD, developed by Keller [42] in the 1950's is valid in the deep lit and deep shadow regions (regions I and III in Figure 4.1), but not in the transition region between shadow and illuminated (region II in the same figure). In his UTD solution for plane wave incidence, Pathak developed a method which accounts for the fields in the transition region (region II) [43]. In this approach a Watson type transform is applied to the exact solution for a circular cylinder [41] and the resulting integrals solved by making appropriate approximations depending on the point of observation. The resulting expressions consist of a Fresnel type integral which dominates in the transition region and a Pekeris function which dominates in the deep lit region and should dominate in the deep shadow region. Hussar *et. al* have shown that the Fresnel term in the UTD solution does not decay in the predicted fashion in the shadow region and thus the Pekeris term does not dominate as expected in this region [44]. For source and/or observation in the near zone of the cylinder the UTD solution is not asymp-

totic (in terms of cylinder radius) and significant error is observed in field calculations as cylinder radius increases. Examples in [44] show an error of greater than 10 dB in the shadow region near transition (the boundary between region II and III in Figure 4.1), which increases to near 40 dB in the deep shadow region. Hussar *et. al* adjust the Pathak formulation with a correction consisting of an infinite series which produces very accurate results. Unfortunately, as in the case of the exact solution for circular cylinders, the convergence properties of the resulting series deteriorates as cylinder radius is increased.

For observation points near or on the cylinder surface, asymptotic field solutions based on Fock theory [45] are usually applied. These solutions in general consist of solving the canonical Fock type integrals, which are functions of a universal variable, in either a numerical fashion or by referencing tabulated data. In the deep lit and deep shadow regions these integrals reduce to an asymptotic and residue series, respectively. These integrals are highly oscillatory in nature and difficult to evaluate numerically, although a method has been proposed by Pearson [46] to improve the convergence properties of integrals of this type. Logan, in his extensive work on diffraction theory, has published tabulated data on the Fock integrals [47]. As the tabulated data is a function of a universal variable, the extent to which this data extends into the lit or shadow regions decreases as cylinder radius increases. At the point where the tabulated data ends a transition must be made to the residue (deep shadow) or asymptotic (deep lit) series. As cylinder radius is increased this transition occurs at a point closer to the shadow boundary, in the lit region. For large cylinders the asymptotic series does not converge well here and a significant discontinuity in the surface current occurs. This effect can also be seen when directly evaluating the Fock integrals numerically and will be discussed in further detail in Section 4.3.1.

Because of the aforementioned problems associated with GTD/UTD methods for field calculations away from the surface of the cylinder and because none of the described methods are valid in all regions around a cylinder, induced surface currents will be used to calculate the scattered fields everywhere. The induced surface currents can be calculated from

the Fock integrals with the obvious advantage of calculating these integrals for specific data points as opposed to using tabulated data. While methods for numerical evaluation of these integrals in an efficient fashion [46] exist in the literature, a technique to evaluate the Fock functions efficiently, without the need for numerical integration is sought.

With this as a motivation a heuristic method is developed to predict the behavior of the induced surface currents on a perfect electric conducting (PEC) circular cylinder, when excited by a plane wave at oblique incidence angles. The induced surface currents are decomposed in the manner of the Physical Theory of Diffraction (PTD) [6] in terms of a uniform or physical optics (PO) component and a non-uniform or diffraction component. In using this decomposition, the proposed method can be described as a form of PTD for convex surfaces. To predict these diffraction currents a set of macromodels are developed using a combination of the asymptotic behavior of the Fock currents [41, 43, 45] and the exact solution for oblique incidence. These macromodels are used to predict the high frequency behavior of the diffraction current as a function of k_0a, where k_0 is the free space propagation constant and a the cylinder radius, to a very high degree of accuracy. To predict the induced surface diffraction currents these macromodels are simply applied to a set of reference data generated by the exact solution for a cylinder of moderate radius. These macromodels are valid for cylinders of radius $a > \lambda$ and the resulting total surface currents are highly accurate. The observed error in magnitude, $e_{||}$, is less than -60 dB, where $e_{||} = 20\log(||\mathbf{J}_{ex}| - |\mathbf{J}_{mm}||)$ and $\mathbf{J}_{ex}$ and $\mathbf{J}_{mm}$ are the exact and macromodeled total induced surface currents, respectively. The error in phase, $e_{\angle}$, is less than $0.1°$ everywhere except in the deep shadow region, where $e_{\angle} = \angle\mathbf{J}_{ex} - \angle\mathbf{J}_{mm}$.

Section 4.2 describes the development of the macromodel as well as all appropriate formulations. In Section 4.3 the macromodel is validated by comparison with currents generated by the exact solution for circular cylinders. Field results calculated from these approximate currents in the near zone of the cylinder are also compared with results from the exact solution. In Section 4.4 the procedure to implement the macromodel is outlined

in a concise fashion. Section 4.5 gives a brief description of other applications of the macromodel, including far-field results of a point source radiating in the presence of a cylinder, which can be used as a model for an aircraft fuselage. Section 4.6 summarizes this chapter.

4.2 Development of Macromodel

In this section the macromodel for calculation of the induced surface diffraction currents will be developed. The problem will be outlined, the Fock formulations for induced surface currents, which are a basis for the macromodel, will be discussed, and specifics of the macromodel development given subsequently. Considering an infinite right circular PEC cylinder, illuminated by a monochromatic plane wave, as shown in Figure 4.2. The cylinder is oriented along the z axis with θ^i defined from the z axis and confined to the $y - z$ plane and ϕ defined from the x axis and positive towards the y axis. The propagation constant of the plane wave $\mathbf{k}$ is defined as $\mathbf{k} = -k_0 \cos \theta^i \, \hat{z} - k_0 \sin \theta^i \, \hat{y}$. For the problem of an infinite cylinder the z component of the propagation constant of the scattered field must match that of the incidence field, requiring that scattered fields be confined to the specular cone, as shown in Figure 4.2.

Decomposing the induced surface current in the manner of PTD we write the diffraction current $\mathbf{J}_D$ as $\mathbf{J}_D = \mathbf{J}_{ex} - \mathbf{J}_{PO}$ where $\mathbf{J}_{PO}$ is the PO current given by,

$$\mathbf{J}_{PO} = \begin{cases} 2\, \hat{n} \times \mathbf{H}^i; & \text{in the illuminated region} \\ 0 & ; \text{ in the shadow region.} \end{cases} \tag{4.1}$$

Depending on the polarization of the incident field, on the cylinder surface,

$$\mathbf{H}^i = \begin{cases} -H_0\, \hat{x} \; ; & \text{for the TM case (transverse magnetic to } z \text{ axis),} \\ H_0(\sin \theta^i \, \hat{z} - \cos \theta^i \, \hat{y}); & \text{for the TE case (transverse electric to } z \text{ axis).} \end{cases} \tag{4.2}$$
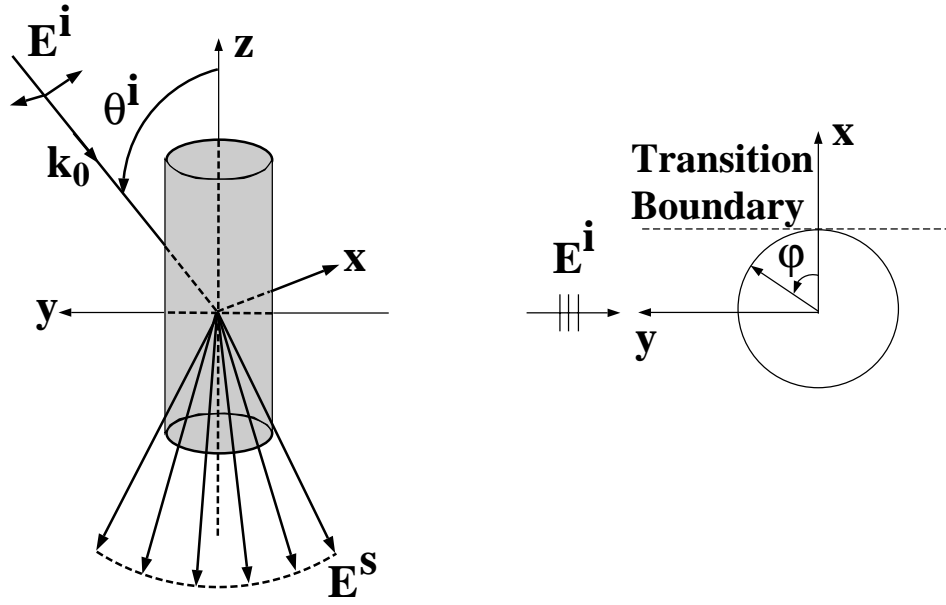
Figure 4.2: Scattering geometry of an infinite cylinder.

The objective is to macromodel $\mathbf{J}_D(\phi) = |\mathbf{J}_D(\phi)| \, e^{j\chi}$ in terms of $k_0 a$ for the general case of oblique incidence and arbitrary polarization. This is accomplished by simply applying appropriate scaling (expansion or contraction of argument ϕ) and weighting (multiplicative factor) functions to reference data consisting of the magnitude and phase components of the exact diffraction current. These are determined for a cylinder of moderate $k_0 a$ excited at normal incidence (2-D case). Subsequently, the Fock formulations for the generation of induced surface currents on a PEC cylinder are reviewed along with observations relevant to developing the macromodel. The macromodel will then be developed for the 2-D case (TM z and TE ϕ currents only are excited) in both the shadow and lit regions. The macromodel for the 2-D currents is then extended to the case of oblique incidence in a simple fashion. All macromodeled currents, including the additional z directed current excited at oblique incidence for the TE case, are generated from the reference data for a cylinder excited at normal incidence (2-D case). Also in all cases the macromodel is applied to generate the induced surface currents on a half cylinder $(-\pi/2 \leq \phi \leq \pi/2$ in Figure 4.2) and this current simply mirrored to generate currents around the full circumference of the cylinder.

87

4.2.1 Fock Theory

The macromodel of the diffraction current $\mathbf{J}_D$ predicts the behavior of this current as a function of $k_0 a$ by observing the asymptotic behavior in the analytical expressions for the Fock currents. These currents indicate the general behavior of the diffraction current as a function of $k_0 a$ for all regions on the cylinder surface. In this section Fock theory is reviewed and observations are made in the Fock formulations relevant to the development of the macromodel. The analytical expressions for currents on the surface of a PEC cylinder are given by Pathak [43]. These expressions are a special case of the Fock currents in which the canonical Fock integrals are approximated by a Taylor series expansion in the close neighborhood of the surface and reduce to the Fock solution on the cylinder surface. In the shadow region the Fock currents for TM and TE cases are given by

$$\mathbf{J}_s^{TM} \;=\; \frac{iU^i(Q_1)}{k_0 Z_0}\, e^{-ik_0 a\phi}\left(\frac{k_0}{m}\right)\tilde{g}(\zeta)\,\hat{z}, \tag{4.3}$$

$$\mathbf{J}_s^{TE} \;=\; -U^i(Q_1)\, e^{-ik_0 a\phi}\, g(\zeta)\,\hat{\phi}, \tag{4.4}$$

where the subscript s denotes the shadow region. In (4.3) and (4.4) $U^i(Q_1)$ is the incident electric field for the TM case and the incident magnetic field for the TE case evaluated on the cylinder surface at the shadow boundary (point Q_1), shown in Figure 4.1. Also in (4.3) and (4.4), $m = (k_0 a/2)^{1/3}$, Z_0 is the characteristic impedance of free space and $\tilde{g}(\zeta)$ and $g(\zeta)$ are the Fock functions given by

$$\tilde{g}(\zeta) = \frac{1}{\sqrt{\pi}}\int\limits_{-\infty}^{+\infty} d\tau\,\frac{e^{i\zeta\tau}}{w_1(\tau)} \tag{4.5}$$

$$g(\zeta) = \frac{1}{\sqrt{\pi}}\int\limits_{-\infty}^{+\infty} d\tau\,\frac{e^{i\zeta\tau}}{w_1'(\tau)}, \tag{4.6}$$

where $\zeta = -m\phi$ and is defined in the shadow region only, and w_1 is the Airy function as defined in [41]. In the lit region the Fock currents are given by

$$\mathbf{J}_l^{TM} = \frac{iU^i(P)}{k_0 Z_0} e^{i\frac{(\zeta')^3}{3}} \left(\frac{k_0}{m}\right) \tilde{g}(\zeta') \, \hat{z}, \tag{4.7}$$

$$\mathbf{J}_l^{TE} = -U^i(P) \, e^{i\frac{(\zeta')^3}{3}} g(\zeta') \, \hat{\phi}, \tag{4.8}$$

where the subscript l denotes the lit region and the incident field U^i is evaluated at the point P on the surface of the cylinder, in the lit region, where the value of the induced surface current is desired. In (4.7) and (4.8), $\tilde{g}$ and g are functions of ζ', where $\zeta' = -m\sin\phi$ and is defined in the lit region only. To construct the macromodel for the induced surface diffraction currents the following observations of the asymptotic behavior of the Fock currents are noted:

1. The factor m, implicit in both ζ (shadow region) and ζ' (lit region), is proportional to $(k_0 a)^{1/3}$.

2. In the shadow region the Fock functions for both the TM and TE cases can be evaluated in terms of a residue series which is a function of ζ. This indicates that the macromodel developed for the complex diffraction current in the shadow region is valid throughout the shadow region.

3. The TM current, given by (4.3) in the shadow region and (4.7) in the lit region, has a weighting factor of $\frac{k_0}{m}$.

4. In the deep lit region $\tilde{g}(\zeta')$ and $g(\zeta')$ can be expanded into an asymptotic series given by

$$\tilde{g}(\zeta') = 2i\zeta' e^{-i\frac{(\zeta')^3}{3}} \left\{ 1 - \frac{i}{4\zeta'^3} + \frac{1}{2\zeta'^6} \cdots \right\}, \tag{4.9}$$

$$g(\zeta') = 2e^{-i\frac{(\zeta')^3}{3}} \left\{ 1 + \frac{i}{4\zeta'^3} - \frac{1}{\zeta'^6} \cdots \right\}. \tag{4.10}$$

89

5. The phase component of the Fock currents can be decomposed into a highly oscilla-
   tory and slowly varying or gentle phase component. If we designate the exponential
   of the diffraction current by $e^{i\chi_h(k_0a,\phi)+i\chi_g(k_0a,\phi)}$ where the subscripts h and g indicate
   the highly oscillatory and gentle phase components of the current, respectively, the
   highly oscillatory phase terms are known in all regions. In the lit region $\chi_h(k_0a,\phi)$ is
   simply the phase of the incident field or

$$\chi_h(k_0a,\phi) = -k_0 a \sin\phi, \tag{4.11}$$

and in the shadow $\chi_h(k_0a,\phi)$ is a linear phase term given by

$$\chi_h(k_0a,\phi) = -k_0 a\phi. \tag{4.12}$$

The remaining gentle phase component $\chi_g(k_0a,\phi)$ is monotonic in both the lit and
shadow regions and this is the component of the phase which will be macromodeled.

4.2.2   2-D Case, Normal Incidence

In this section the macromodel will be developed for the magnitude of the TM $\hat{z}$ and
TE $\hat{\phi}$ diffraction currents in the shadow region, normal incidence. The macromodel for the
diffraction current magnitude will then be extended to the lit region. Finally, the gentle
phase component will be macromodeled.

As mentioned previously, to generate diffraction currents for cylinders of arbitrary ra-
dius, the macromodels will be applied to reference data consisting of the diffraction cur-
rents from a cylinder of moderate radius, generated from the exact solution. The macro-
models described in this section are developed using reference data for the TM case from a
cylinder of radius 20λ and for the TE case a cylinder of radius 50λ. Reasons for the choice
of these cylinder sizes to generate the reference currents will be given in more detail in

Section 4.3.

Magnitude, Shadow region

To begin development of the macromodel for the diffraction current magnitude in the shadow region we again note that the Fock currents in the shadow region can be evaluated in terms of a residue series and thus the macromodel developed is valid throughout the shadow region. Recall that the factor m is proportional to $(k_0 a)^{1/3}$ and is implicit in the argument ζ of both the $\tilde{g}(\zeta)$ and $g(\zeta)$ terms in equations (4.3) and (4.4). This implies a scaling of ϕ by $(k_0 a)^{1/3}$ for both the TM and TE cases. For the TM case, a factor of $(1/m)$ is observed in (4.3) implying a multiplicative or weighting factor for the TM current of $(k_0 a)^{-(1/3)}$. Observation of (4.4) shows no weighting of the TE currents in the shadow region. Examination of diffraction currents generated by the exact solution, however, shows that the TM weighting factor is approximate and that there is a small weighting of the TE currents. Empirical expressions are determined, which are functions of $k_0 a$, to adjust for this. Applying these scaling and weighting factors we now define the macromodel in the shadow region, relating the diffraction current magnitudes on a cylinder of arbitrary radius a_2 to that of the reference cylinder of radius a_1 by

$$|\mathbf{J}_D^{TM,TE}(k_0 a_2, \phi)| = \Phi_s^{TM,TE} |\mathbf{J}_D^{TM,TE}(k_0 a_1, \left(\frac{k_0 a_1}{k_0 a_2}\right)^{(1/3)} \phi)|. \tag{4.13}$$

The weighting factor $\Phi_s^{TM,TE}$ is given by

$$\Phi_s^{TM,TE} = \left(\frac{k_0 a_1}{k_0 a_2}\right)^{W_s^{TM,TE}(k_0 a_2)}, \tag{4.14}$$

where $W_s^{TM,TE}(k_0 a_2)$ is approximately equal to $(1/3)$ for the TM case and 0 for the TE case. Expressions for $W_s^{TM,TE}(k_0 a_2)$ are obtained empirically from the exact solution and

are given by

$$W_s^{TM}(k_0 a_2) =$$

$$
\begin{cases}
0.3373 + 0.009562 e^{-0.1176 k_0 a_2} + 0.0045531 e^{-0.04896 k_0 a_2} & 1\lambda < a_2 < 20\lambda \\
0.3348 + 0.005651 e^{-0.01103 k_0 a_2} + 0.001721 e^{-0.0024 k_0 a_2} & 15\lambda < a_2 < +\infty
\end{cases}
\tag{4.15}
$$

$$W_s^{TE}(k_0 a_2) =$$

$$
\begin{cases}
-0.02086 + 0.01708(1 - e^{-0.09979 k_0 a_2}) & \\
\qquad\qquad + 0.006827(1 - e^{-0.002576 k_0 a_2}) & 1\lambda < a_2 < 50\lambda \\
-|0.005987 - 0.007045(1 - e^{-0.006046 k_0 a_2})| & 20\lambda < a_2 < +\infty.
\end{cases}
\tag{4.16}
$$

Magnitude, Lit Region

To macromodel the magnitude of the TM $\hat{z}$ and TE $\hat{\phi}$ diffraction current in the lit region we note that the behavior of the diffraction current (as a function of $k_0 a$) transitions from the shadow boundary to the deep lit region. To macromodel this behavior the magnitude of the diffraction current is defined in the lit region, at and very near the shadow boundary, and also at the deep lit region. Sigmoidal functions are then used to model the transition from the shadow boundary to the deep lit region.

To define the magnitude of the diffraction current in the lit region at and very near the shadow boundary for the TM case we note that in the transition from shadow to lit regions the magnitude of the TM diffraction current is continuous across the shadow boundary therefore (4.13) and (4.14) apply in the lit region at and very near the shadow boundary. However, for the TE case the magnitude of the diffraction current across the transition from shadow to lit is discontinuous. The PO current for the TE case undergoes an abrupt transition from a constant in the lit region to zero at the shadow boundary. The exact TE current

transitions gradually and monotonically across the shadow boundary. Remembering that the diffraction current is defined as $\mathbf{J}_D = \mathbf{J}_{ex} - \mathbf{J}_{PO}$, the abrupt change in the PO current causes a phase reversal in the TE diffraction current and an abrupt change in the magnitude of the TE diffraction current across the shadow boundary. This can be seen in Figure 4.3b. It was determined empirically from the exact solution that near the shadow boundary in the lit region, (4.13) and (4.14) can be applied for the TE case if the factor $W_s^{TE}(k_0 a_2)$ is modified as follows:

$$W_{l,sb}^{TE}(k_0 a_2) = -2.25 W_s^{TE}(k_0 a_2), \tag{4.17}$$

where the subscript l, sb implies the lit region at the shadow boundary.

To define the magnitude of the diffraction currents in the deep lit region recall that in the deep lit region the surface currents are described by the asymptotic expansions of the Fock functions, $\tilde{g}(\zeta')$ and $g(\zeta')$ given in (4.9) and (4.10). The first terms in (4.9) and (4.10) are the PO currents, with higher order terms defining the non-uniform or diffraction currents. In the deep lit region only the second term in (4.9) and (4.10) are needed to evaluate the diffraction current. Substituting the second term in (4.9) and (4.10) for $\tilde{g}(\zeta')$ and $g(\zeta')$ in (4.7) and (4.8) and evaluating the resulting expressions indicates that the diffraction current in the deep lit region is weighted by a coefficient of $1/(k_0 a)$, implicit in the $(\zeta')^3$ term in the denominator of the second term in (4.9) and (4.10) (recall that, $m = (k_0 a / 2)^{1/3}$). There is no scaling of the argument ϕ in the deep lit region for either the TM or TE case.

Having established the behavior of the diffraction current magnitudes at the shadow boundary and in the very deep lit region, a function must be specified to transition from the shadow boundary to the deep lit region. In a manner similar to the shadow region we first define the relationship between the diffraction current magnitude in the lit region on a

93

cylinder of arbitrary radius a_2 and the reference cylinder of radius a_1 as

$$|\mathbf{J}_D^{TM,TE}(k_0 a_2, \phi)| = \Phi_l^{TM,TE} |\mathbf{J}_D^{TM,TE}(k_0 a_1, \left(\frac{k_0 a_1}{k_0 a_2}\right)^{S_l^{TM,TE}(\phi)} \phi)|, \quad (4.18)$$

where $\Phi_l^{TM,TE}$ is the weighting factor in the lit region given by

$$\Phi_l^{TM,TE}(k_0 a_2, \phi) = \left(\frac{k_0 a_1}{k_0 a_2}\right)^{W_l^{TM,TE}(\phi)}, \quad (4.19)$$

and the functions $S_l^{TM,TE}(\phi)$ and $W_l^{TM,TE}(\phi)$ in (4.18) and (4.19) are the powers of the scaling and weighting expressions for the TM and TE cases, and define the transition in the lit region. Recognizing that these functions ought to be very gentle, with known values at the shadow boundary ($\phi = 0$) and deep lit region ($\phi = \pi/2$) Sigmoidal functions are chosen to describe the transition. S_l and W_l are given by the following expressions:

$$S_l(\phi) = b - \frac{c}{1 + e^{-d(\frac{\phi}{2\pi} - \phi_0)}}, \quad (4.20)$$

and

$$W_l(\phi) = b + \frac{c}{1 + e^{-d(\frac{\phi}{2\pi} - \phi_0)}}, \quad (4.21)$$

where b, c, d, and ϕ_0 in (4.20) and (4.21) are constant parameters determined by optimization. To calculate the optimal values for these coefficients a simple search algorithm is employed. The algorithm searches through a range of values for d and ϕ_0 (b and c are defined in terms of d and ϕ_0) and determines the values which produce minimum error between diffraction current generated by the exact solution and diffraction current generated by the macromodel. On a test cylinder of radius $a = 200\lambda$ (as the transitional behavior of the diffraction currents through the lit region is a function of ϕ only, any cylinder of radius larger than the reference cylinders can be used as a test cylinder for optimization of these

94

parameters), the optimal values of b, c, d, ϕ_0 are determined and are given in Table 4.1, with the exception of the b and c coefficients for for $W_l^{TM,TE}$ defined as b_w^{TM}, b_w^{TE}, c_w^{TM} and c_w^{TE} in Table 4.1. At the shadow boundary W_l^{TM} is defined by W_s^{TM} and W_l^{TE} is defined by $W_{l,sb}^{TE}$ (W_l^{TE} defined at the shadow boundary given in (4.17)), making both functions of k_0a. These coefficients as functions of k_0a are given by

$$c_w^{TM} = (1 - W_s^{TM}) \left[\frac{1}{1 + e^{-d(1-\phi_0)}} - \frac{1}{1 + e^{d\phi_0}} \right]^{-1} \tag{4.22}$$

$$c_w^{TE} = (1 - W_{l,sb}^{TE}) \left[\frac{1}{1 + e^{-d(1-\phi_0)}} - \frac{1}{1 + e^{d\phi_0}} \right]^{-1} \tag{4.23}$$

$$b_w^{TM,TE} = 1 - c_w^{TM,TE} \left[\frac{1}{1 + e^{-d(1-\phi_0)}} \right]. \tag{4.24}$$

Table 4.1: Optimized parameters for Sigmoidal transition functions

	d	ϕ_0	b	c
$S_l^{TM}(\phi)$	9.903	0.5650	0.3346	0.3391
$S_l^{TE}(\phi)$	10.6	0.6630	0.3336	0.3430
$W_l^{TM}(k_0a, \phi)$	10.025	0.5268	b_w^{TM}	c_w^{TM}
$W_{l2}^{TE}(k_0a, \phi)$	8.5	0.610	b_w^{TE}	c_w^{TM}

Phase, All Regions

Having developed an accurate model for the magnitude of the complex diffraction current the next step is to macromodel the gentle phase component for the 2-D case. This gentle phase component, $\chi_g(k_0a, \phi)$, is monotonic for the TM case and piecewise monotonic for the TE case as shown in Figures 4.4a and 4.4b, respectively. The observed behavior

of the Fock currents again allows for prediction of the asymptotic behavior of this gentle phase factor in an accurate fashion. As already noted, in the shadow region a residue series is applied to calculate the complex surface currents. Recall that this residue series is a function of ζ which again implies a scaling of the argument ϕ, implicit in ζ, by $(k_0 a)^{(1/3)}$ for both the TM and TE cases. This scaling was determined to be valid for the gentle phase function in the shadow region. In addition, it was also determined empirically that this scaling is an acceptable approximation in the lit region. While no weighting of the gentle phase component is implied by observation of the Fock currents it was observed empirically that a small offset of $\chi_g(k_0 a, \phi)$ as a function of $k_0 a$ is necessary and this offset is determined by observation of the exact solution. Thus the expression relating the gentle phase component for a cylinder of radius a_2 to the reference cylinder of radius a_1 is

$$\chi_g^{TM,TE}(ka_2, \phi) = O^{TM,TE} + \chi_g^{TM,TE}\left(ka_1, \left(\frac{k_0 a_1}{k_0 a_2}\right)^{(1/3)} \phi\right), \tag{4.25}$$

where $O^{TM,TE}$ is the adjustment factor for the gentle phase term and is given for the TM case in all regions and the TE case in the shadow region by

$$O^{TM,TE}(k_0 a_2) =$$

$$\begin{cases} 0.07255 - 0.05857(1 - e^{-0.08778 k_0 a_2}) \\ \qquad - 0.01777(1 - e^{-0.01231 k_0 a_2}) & 1\lambda < a_2 < 20\lambda \\ 0.01608 - 0.01701(1 - e^{-0.01592 k_0 a_2}) \\ \qquad - 0.005747(1 - e^{-0.002158 k_0 a_2}) & 15\lambda < a_2 < +\infty, \end{cases} \tag{4.26}$$

As mentioned earlier the PO current for the TE case undergoes an abrupt transition at the shadow boundary causing a phase reversal in the diffraction current. Thus, χ_g^{TE} is discontinuous across the shadow boundary as can be seen in Figure 4.4b. Consequently, O^{TE} is also discontinuous across the shadow boundary. The relationship between O^{TE} in

the shadow and lit regions was determined empirically to be

$$O_l^{TE}(k_0 a_2) = -2\, O_s^{TE}(k_0 a_2). \tag{4.27}$$

4.2.3 Oblique Incidence

In this section the macromodel developed for the 2-D case will be extended to that of oblique incidence. In addition a procedure for macromodeling the additional TE z-directed current generated at oblique incidence will be given. The extension to oblique incidence is rather simple and can be done in an analytic fashion. The coordinates are as described by Figure 4.2 remembering that normal incidence corresponds to $\theta^i = \pi/2$. The exact solution, normal incidence, for the TM and TE currents on the surface of a PEC circular cylinder are in the form of an eigenfunction expansion and are given by [40]

$$J_z^{TM} = \frac{2E_0}{\pi Z_0 k_0 a} \sum_{n=-\infty}^{+\infty} i^n \frac{e^{-in\phi}}{H_n^{(2)}(k_0 a)} \tag{4.28}$$

$$J_\phi^{TE} = -i\, \frac{2H_0}{\pi k_0 a} \sum_{n=-\infty}^{+\infty} i^n \frac{e^{-in\phi}}{H_n^{(2)'}(k_0 a)}, \tag{4.29}$$

where E_0 and H_0 are the magnitude of the incident electric and magnetic fields, respectively. The exact solution for oblique incidence is given by [40]

$$J_z^{TM} = \frac{2E_0 e^{-ik_0 \cos\theta^i z}}{\pi Z_0 (k_0 a \sin\theta^i)} \sum_{n=-\infty}^{+\infty} i^n \frac{e^{-in\phi}}{H_n^{(2)}(k_0 a \sin\theta^i)} \tag{4.30}$$

$$J_\phi^{TE} = -i\, \frac{2H_0 \sin\theta^i e^{-ik_0 \cos\theta^i z}}{\pi k_0 a} \sum_{n=-\infty}^{+\infty} i^n \frac{e^{-in\phi}}{H_n^{(2)'}(k_0 a \sin\theta^i)}, \tag{4.31}$$

It is evident in the relation of (4.30) and (4.31) to (4.28) and (4.29) that surface currents for the case of oblique incidence can be obtained from those of normal incidence with the following modifications:

- $k_0 a \rightarrow k_0 a \sin \theta^i$, incident wave simply "sees" an effectively smaller cylinder

- a multiplicative, progressive phase factor, $e^{-ik_0 \cos \theta^i z}$ is added

- TE current is modified by $\sin \theta^i$ (projection factor)

An additional z - directed current is generated for the TE case at oblique incidence angles. This current is not independent and its dependence on $J_\phi^{TE}(k_0 a, \phi, \theta^i)$ is given by [40]

$$J_z^{TE}(k_0 a, \phi, \theta^i) = \frac{-i \cot \theta^i}{k_0 a \sin \theta^i} \frac{\partial}{\partial \phi} J_\phi^{TE}(k_0 a, \phi, \theta^i). \tag{4.32}$$

Having an expression for $J_\phi^{TE}(k_0 a, \phi, \theta^i)$, the expression for $J_z^{TE}(k_0 a, \phi, \theta^i)$ can be obtained. However, remembering that $J_\phi^{TE}(k_0 a, \phi, \theta^i)$ is composed of a PO component, $J_{PO\phi}^{TE}(k_0 a, \phi, \theta^i)$ and a diffraction component, $J_{D\phi}^{TE}(k_0 a, \phi, \theta^i)$, the magnitude and phase of $J_{D\phi}^{TE}(k_0 a, \phi, \theta^i)$ is macromodeled separately and evaluation of $\frac{\partial}{\partial \phi} J_{D\phi}^{TE}(k_0 a, \phi, \theta^i)$ is not straightforward. A procedure is outlined for the calculation of $\frac{\partial}{\partial \phi} J_{D\phi}^{TE}(k_0 a, \phi, \theta^i)$.

As mentioned, in order to generate $J_z^{TE}(k_0 a, \phi, \theta^i)$, the term $\frac{\partial}{\partial \phi} J_{D\phi}^{TE}(k_0 a, \phi, \theta^i)$ must be evaluated in terms of the macromodel. The expression for $J_{D\phi}^{TE}(k_0 a, \phi, \theta^i)$ in terms of the macromodel is of the form given by (4.13), (4.18) and (4.25) or

$$J_{D\phi}^{TE}(k_0 a_2, \phi) = \Phi^{TE} \left| J_{D\phi}^{TE}\left(k_0 a_1, \left(\frac{k_0 a_1}{k_0 a_2}\right)^{S^{TE}(k_0 a_2, \phi)} \phi\right) \right|$$

$$e^{\{iO^{TE}(k_0 a_2) + i\chi_g^{TE}(k_0 a_1, (\frac{k_0 a_1}{k_0 a_2})^{(1/3)} \phi)\}} e^{i\chi_h(k_0 a_2, \phi)}. \tag{4.33}$$

The derivative of (4.33) with respect to ϕ, in terms of the macromodel, is straightforward with the exception of two terms. These terms are the derivatives of the magnitude and gentle phase component of the reference cylinder, and their evaluation in terms of the macromodel is not obvious. These terms are given by:

$$\frac{\partial}{\partial \phi} |J_{D\phi}^{TE}(k_0 a_1, \left(\frac{k_0 a_1}{k_0 a_2}\right)^{S^{TE}(k_0 a_2, \phi)} \phi)| = \frac{\partial}{\partial \tilde{\phi}} |J_{D\phi}^{TE}(k_0 a_1, \tilde{\phi})| \cdot \frac{\partial \tilde{\phi}}{\partial \phi} \tag{4.34}$$

where

$$\tilde{\phi} = \left(\frac{k_0 a_1}{k_0 a_2}\right)^{S^{TE}(k_0 a_2, \phi)} \phi \tag{4.35}$$

and

$$\frac{\partial}{\partial \phi} \chi_g^{TE}(k_0 a_1, \left(\frac{k_0 a_1}{k_0 a_2}\right)^{(1/3)} \phi) = \left(\frac{k_0 a_1}{k_0 a_2}\right)^{(1/3)} \frac{\partial}{\partial \tilde{\phi}} \chi_g^{TE}(k_0 a_1, \tilde{\phi}) \tag{4.36}$$

where S^{TE} in (4.34) is the scaling factor for the TE case, given by $1/3$ in the shadow region and the Sigmoidal transition function S_l^{TE} in the lit region, as described previously. While evaluation of the $\frac{\partial \tilde{\phi}}{\partial \phi}$ in (4.34) is simple, evaluation of the other derivatives to the right of the equal sign in (4.34) and (4.36) is not. To evaluate these terms we note that $\frac{\partial}{\partial \tilde{\phi}} |J_{D\phi}^{TE}(k_0 a_1, \tilde{\phi})|$ and $\frac{\partial}{\partial \tilde{\phi}} \chi_g^{TE}(k_0 a_1, \tilde{\phi})$ in (4.34) and (4.36) are derivatives of the entire argument and are therefore independent of $k_0 a$. We can therefore calculate these terms directly from diffraction current in the reference data. To do this we simply define the diffraction current in terms of its real and imaginary parts or $J_{D\phi}^{TE} = X + iY$. The derivative of the magnitude is then given by

$$\frac{\partial}{\partial \tilde{\phi}} |J_{D\phi}^{TE}| = \frac{XX' + YY'}{\sqrt{X^2 + Y^2}}, \tag{4.37}$$

and the derivative of the phase by

$$\frac{\partial}{\partial \tilde{\phi}} \chi_g^{TE} = \frac{Y'X - YX'}{X^2 + Y^2}. \qquad (4.38)$$

4.3 Validation: PEC Cylinder

In the previous section a macromodel was developed which relates the diffraction current on a PEC cylinder of arbitrary radius a_2 to that of a reference cylinder of radius a_1, for plane wave excitation. In practice this macromodel allows the complex diffraction currents for any cylinder with radius a_2 illuminated by a plane wave at oblique incidence to be generated from the diffraction current for a reference cylinder of radius a_1 when excited at normal incidence. The reference data is generated using the exact solution for a cylinder with a moderate value of $k_0 a$. In this section the validity and accuracy of the macromodel is examined by comparing the surface currents and near fields generated by the eigensolution with those of the macromodel for cylinders of radii larger than 1λ. Figure 4.3 shows the macromodeled diffraction current magnitude for cylinders of radii 10λ and 100λ excited at normal incidence compared to the exact solution for the TM case (a) and the TE case (b). The horizontal axes in both figures are the normalized angular dimension or $\phi/2\pi$ with $\phi/2\pi = 0, 0.5$ corresponding to the top and bottom shadow boundaries respectively.

As mentioned previously, the reference cylinder radius a_1 was chosen to be 20λ for the TM case and 50λ for the TE case. The choice of radius for the reference cylinder is somewhat subjective but the main criteria was the negligible level of the ripple in the magnitude and gentle phase components of the exact diffraction current in the deep shadow. The diffraction current magnitude component in the deep shadow show a rapid oscillation (ripple) (as seen in Figure 4.3) which is due to the effects of higher order diffraction (multiple transitions of the creeping wave around the cylinder). The gentle phase component exhibits similar behavior but at a much lower level. As cylinder radius increases the

100

(a) $|J_{Dz}^{TM}|$ (b) $|J_{D\phi}^{TE}|$
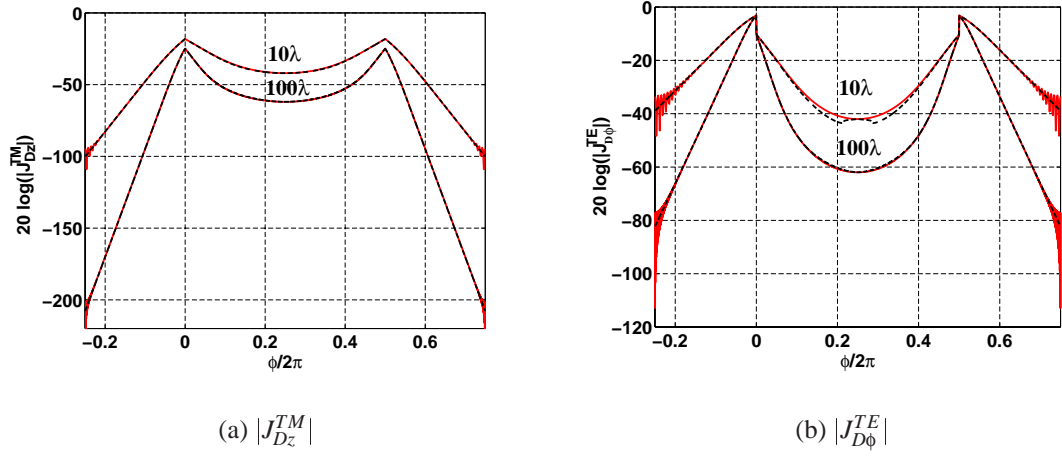
Figure 4.3: Diffraction current magnitude (dB) around full circumference of 10 and 100λ PEC cylinders excited at normal incidence angle, $\theta^i = \pi/2$, eigensolution current (———), compared with macromodeled current (- - - - - -), $\frac{\phi}{2\pi} = 0$ is equivalent to a point on top of the cylinder, perpendicular to the shadow boundary, with $\frac{\phi}{2\pi} = -0.25$ in the deep shadow region.

frequency of the ripple increases and becomes more localized to the deep shadow region ($\phi/2\pi = -0.25$ in Figure 4.3). It should be noted that the level of diffraction current at which this ripple takes place is very low and therefore it is unlikely that this ripple would affect the near field anywhere except perhaps very near the surface in the deep shadow. Because this ringing cannot be macromodeled a reference cylinder radius was chosen to minimize the error between the exact solution and the macromodel for any cylinder radius greater than 1λ. In the reference data this ripple is removed from both the magnitude and gentle phase components of the diffraction current and the remaining curve extended by assuming a continuation of the slope of the remaining data. The macromodeled diffraction current for the TE case (Figure 4.3b) shows noticeable error for the 10λ cylinder in the deep lit region ($\phi/2\pi = 0.25$) and is attributed to increasing error in the value of the weighting factor Φ, for decreasing $k_0 a$. In this region the PO current is dominant however and the error in the total current is still within the values described previously. In practice this has no effect on the accuracy of the total fields.

The error between the exact solution and the macromodel was investigated from a cylin-

101

(a) χ_g^{TM}

(b) χ_g^{TE}
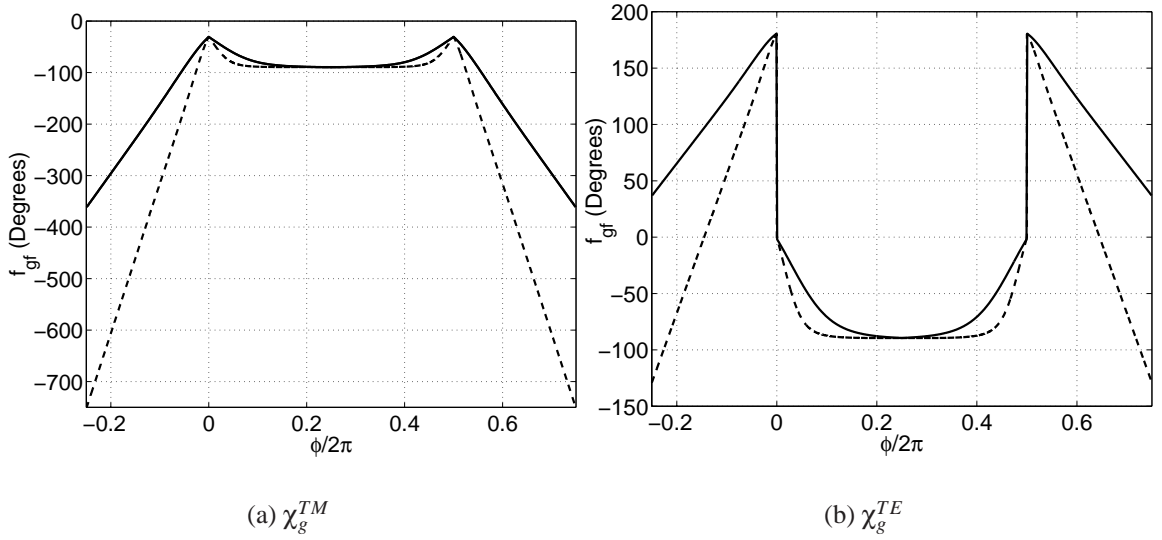
Figure 4.4: Gentle phase component (degrees) around full circumference of 10 and 100λ PEC cylinders excited at normal incidence angle, $\theta^i = \pi/2$, 10λ (———), 100λ (- - - - - -), $\frac{\phi}{2\pi} = 0$ is equivalent to a point on top of the cylinder, perpendicular to the shadow boundary, with $\frac{\phi}{2\pi} = -0.25$ in the deep shadow region.

der of 1λ radius up to a cylinder with radius of 200λ. In this range the maximum error in magnitude in the total current (PO + diffraction) was -60 dB where the magnitude error is as previously defined or, $e_{\parallel} = 20\log(||J_{ex}| - |J_{mm}||)$. The phase error over this range was found to be less than 0.1° near the shadow boundary. Figure 4.5 shows an example of the macromodeled total current for a 100λ PEC cylinder excited at oblique incidence $\theta^i = \pi/4$ as compared to the exact current. Figure 4.5a and Figure 4.5b show the magnitude and phase, respectively, of the total current for the TM case. Figure 4.5c shows the TE ϕ - directed current with Figure 4.5d showing the additional z - directed current for the TE case at oblique incidence angle. As can be seen the macromodel agrees very well with the exact solution in all cases.

The accuracy of the total fields (incident + scattered) generated by the macromodeled currents is shown in Figure 4.6a for the TM case and Figure 4.6b for the TE case. The data shown is for a 100λ cylinder excited at oblique incidence, $\theta^i = \pi/4$, with fields 1λ

off the cylinder surface plotted. Results from the macromodel are again compared with the exact solution. The scattered fields for both solutions are generated by applying the radiation integrals to the exact and macromodeled total currents. The fields generated by the macromodel are in good agreement over the entire range shown for both the TM and TE cases. The macromodel was shown to produce near fields which are highly accurate over a dynamic range of greater than 85 dB for cylinders of up to 200λ radius. The one exception to this is the TE ϕ - directed near fields at oblique incidence. As the incidence angle approaches grazing the TE PO current is attenuated by a $\sin\theta^i$ factor. As this happens the accuracy of the TE ϕ - directed near fields is degraded. In the near field however the TE ρ - directed field is the dominate field component and the total field retains the high degree of accuracy previously shown.

4.3.1   Direct Evaluation of Fock Type Integrals

As mentioned in the introductory section direct numerical evaluation of the Fock integrals is difficult due to their highly oscillatory nature. At this point it is relevant to compare results generated by direct numerical evaluation of these integrals to the proposed macromodel. We begin by observing the TM and TE current distributions, for cylinders of radius 10, 15, and 20λ, and generated by the Fock type integrals as seen in Figure 4.7. What is apparent in these curves is the convergence problems of the Fock type integrals in the deep lit region, and the increasing region of non-convergence as cylinder radius increases. As cylinder radius is increased the integrand becomes more oscillatory, and evaluation of the Airy type functions w_1, w_1' in (4.5) and (4.6), more difficult. Convergence of the integrand for larger radius requires evaluation of the integrand for larger argument of w_1. As the argument of w_1 increases it value increases exponentially (see [41]) and the numerical error in evaluating the integrand grows significantly, thus making convergence difficult. This correlates with the discontinuity between transitioning from tabulated data generated in the lit region towards the shadow boundary [47], to the asymptotic solution applied in the deep

lit region, discussed previously. Due to the discussed convergence problems, it becomes difficult to generate tabulated data to a point in the deep lit region where transition to the asymptotic series becomes practical.

Table 4.2 shows the speed-up in time for the macromodel to calulate the induced surface currents, over the time required for numerical evaluation of the Fock integrals (as before speed-up is the time in seconds required to calculate the Fock integrals divided by the time in seconds to calculate the currents using the macromodel). As can be seen evaluation of the macromodel is significantly faster, especially when noting that to achieve complete convergence of the Fock type integrals would require even more time. The scheme proposed by Pearson [46] would eliviate some on the problems in evaluating the Fock type integrals, but numerical integration is still required and while a speed up of 10 is reported over direct evaluation of the Fock solution, this is based on a nominal accuracy requirement of 10%, with higher accuracy requiring more computation time.

Table 4.2: Speed-up, Macromodel to Fock Integrals

Cylinder radius, a	Speed-up
10	13.0
15	18.8
20	34.7

A final note is the effect of the non-convergence of the Fock type integrals on the total electric fields. Figure 4.8 shows a comparison of the total TM fields generated by the macromodeled currents to those generated by the Fock type integrals, for a cylinder of radius 15λ. In Figure 4.7 is is apparent that the evaluation of the Fock integrals for a 15 radius cylinder did not converge properly near normal incidence, in the deep lit region. This discrepency is apparent in the accuracy of the total fields seen in Figure 4.8. It can be shown by asymptotic evaluation of the radiation integrals that in the deep lit and deep shadow regions the main contributor to the scattered fields is the current in the neighborhood around normal incidence, the same area where the convergence problems arise. This

is evident in Figure 4.8 as the most significant error between the total fields generated by the Fock integrals when compared to those generated by the macromodel can be seen in these regions.

4.4 Application of Macromodel

To summarize the techniques described in the previous sections, the following steps are applied to calculated the induced surface currents on a PEC cylinder using the proposed macromodel:

1. Generate reference data at normal incidence ($a = 20\lambda$ for TM, $a = 50\lambda$ for TE) using the exact solution. Remove oscillations in reference data in deep shadow and approximate by extending slope of remaining data.

2. Apply equations (4.13) through (4.16) and (4.17) through (4.24) to the magnitude of the reference data for normal incidence to generate the magnitude of the diffraction current in the shadow and lit regions, respectively, for a cylinder of the desired radius.

3. Apply equations (4.25) through (4.27) to the gentle phase component of the reference data for normal incidence to generate the gentle phase component in the shadow and lit regions, respectively.

4. To generate the TM $\hat{z}$ and TE $\hat{\phi}$ currents for oblique incidence simply apply the modifications given in Section 4.2.3. For the additional z directed current generated at oblique incidence for the TE case apply (4.32) through (4.38) to the reference data for normal incidence to generate the derivative of the ϕ directed current needed.

5. Reference cylinder data is compressed on ϕ axis when macromodeling surface diffraction current on cylinders of larger radius than that of the reference cylinder. Because of this the macromodeled data does not extend over full range of cylinder (deep

shadow to deep lit). To extend the macromodeled data to the full extent of the cylinder simply assume a continuation of the slope in the lit and shadow regions, respectively.

6. If higher sampling of diffraction currents is required apply simple linear interpolation to the magnitude and gentle phase component of the macromodeled current to generate additional data points.

4.5   Other Applications

The ability to accurately predict the scattered fields from a circular cylinder or any general convex surface has applications other than those of interest in this thesis and at this point it is appropriate to give some mention of them. In radar applications the proposed method could be used to evaluate the detectability of hidden targets behind a hill or knoll. In an extension to applications in wireless communication the macromodel can be applied to evaluate the field pattern of antennas mounted on structures of circular cross-section. As an example of this consider a small dipole mounted on an aircraft fuselage. By application of reciprocity [48] source and observation can be exchanged, and the case of plane wave incidence-near field observation, examined thus far, can be applied to evaluate the far-fields generated from a point source (small dipole) radiating in the presence of a convex surface. It can be shown through reciprocity that for identical point sources the following relationship holds:

$$\hat{l}_1 \cdot \mathbf{E}_2 = \hat{l}_2 \cdot \mathbf{E}_1, \tag{4.39}$$

where $\mathbf{E}_1$, $\mathbf{E}_2$ are electric fields caused by point sources with orientation $\hat{l}_1$, $\hat{l}_2$, respectively. If $\hat{l}_1$ is radiating in the far-field of the convex surface and the corresponding electric field $\mathbf{E}_1$ is observed in the near-field of the surface it is equivalent to the plane wave excitation

problem with the incident plane wave weighted by the dipole field coefficients given by

$$\mathbf{E}_d^i(\mathbf{r}) = \frac{-il_1 k_0 Z_0 I_0}{4\pi r} \, e^{ik_0 r} [\bar{\bar{I}} - \hat{k}_1^i \cdot \hat{l}_1 \hat{k}_1^i], \tag{4.40}$$

where the vector $\mathbf{r} = r\hat{r}$ is defined from the axis origin (always at the origin of the local radius of curvature) to the dipole position, l_1 is the dipole length, and I_0 is the dipole current magnitude. If l_2 is the orientation of a dipole radiating in the near-field of the convex surface and knowing the plane wave solution (4.39) can be solved for fields $\mathbf{E}_2$ which are the far-fields generated by an infinitesimal dipole radiating in the presence of a convex surface. Applying this technique, far-field results for the 2-D case were generated for an infinitesimal dipole radiating in the presence of a 20λ circular PEC cylinder which can represent the fuselage of an aircraft (12m diameter at 1 GHz). The dipole is positioned at the top of the fuselage (x axis, coordinates in Figure 4.2 apply), 0.1λ away from the surface. Figure 4.9 the shows the far-field patterns for three dipole orientations along with their corresponding positions. Figure 4.9a shows the result from a x - directed point source with Figures 4.9b and 4.9c showing the results from a y and z - directed dipole. Again the fields generated from the macromodel are in excellent agreement with those generated by the exact solution.

4.6 Chapter Summary: Diffraction from Right Circular Cylinders

Motivated by the shortcomings in existing high frequency techniques, an alternative method was sought to calculate the diffraction and scattering from general convex surfaces. In this chapter the case of right circular cylinders was examined and a macromodel developed, based on PTD and Fock analysis, which predicts the diffraction currents induced on the surface of electrically large cylinders when excited by a plane wave at oblique

angles. The case of a PEC cylinder was examined and an approach to determining these diffraction currents was presented which is based on the asymptotic behavior of the Fock currents. The method is highly accurate, producing total near fields with a dynamic range of over 85 dB. The macromodel developed is algebraic in nature and simple to implement.

In the next chapter the macromodel developed is extended to include the case of general convex surfaces, when excited at oblique angles. The macromodeled currents are extended to a convex surface in the standard manner of applying the currents induced on a circular cylinder locally on the convex surface.

(a) $|J_z^{TM}|$

(b) $\angle J_z^{TM}|$

(c) $|J_\phi^{TE}|$

(d) $|J_z^{TE}|$
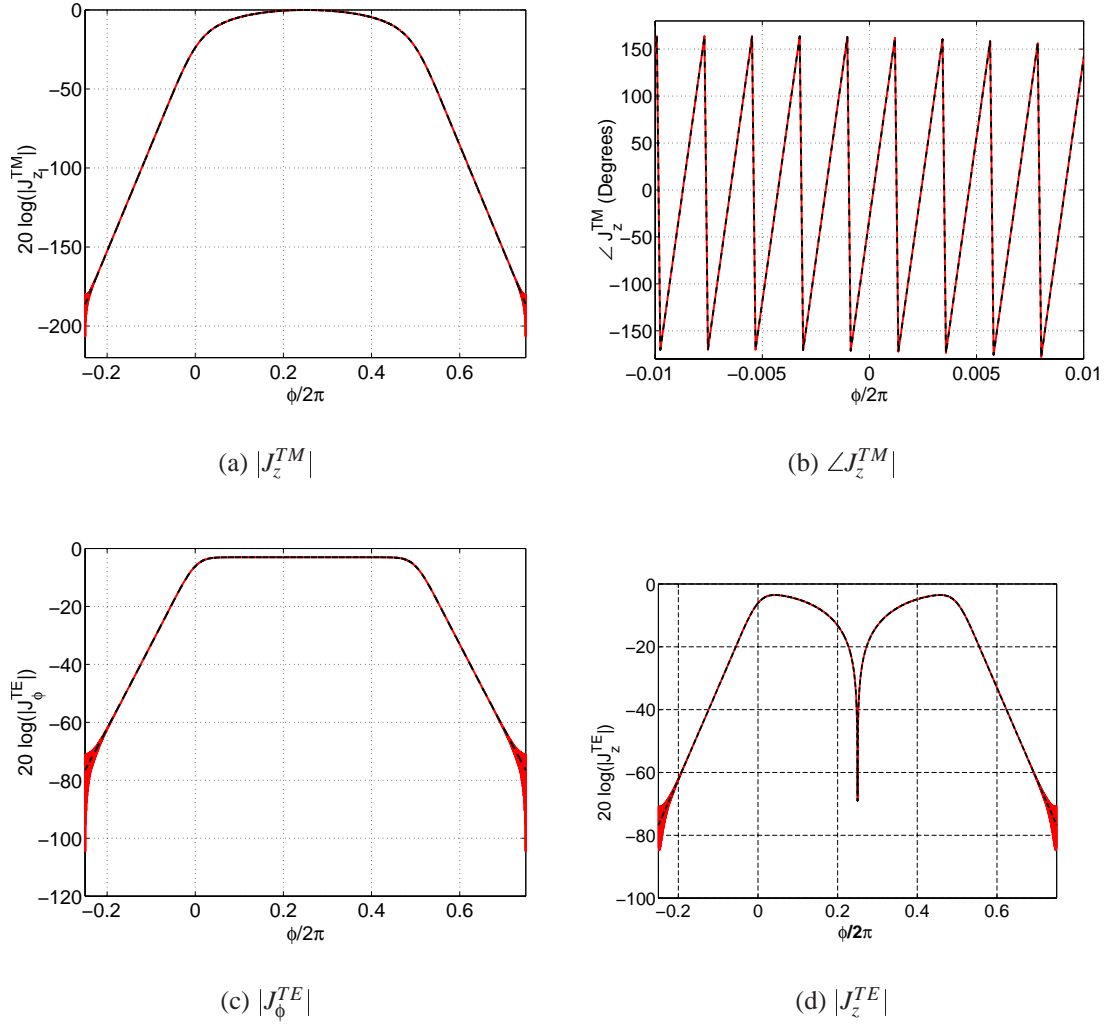
Figure 4.5: Total current, magnitude (dB) and phase (degrees) around full circumference of a 100λ PEC cylinder excited at oblique incidence angle, $\theta^i = \pi/4$, eigensolution current (——), compared with macromodeled current (- - - - - -), $\frac{\phi}{2\pi} = 0$ is equivalent to a point on top of the cylinder, perpendicular to the shadow boundary, with $\frac{\phi}{2\pi} = -0.25$ in the deep shadow region. (a) and (b) are magnitude and phase of TM z - directed current with (c) and (d) magnitude of TE ϕ and z - directed current respectively.
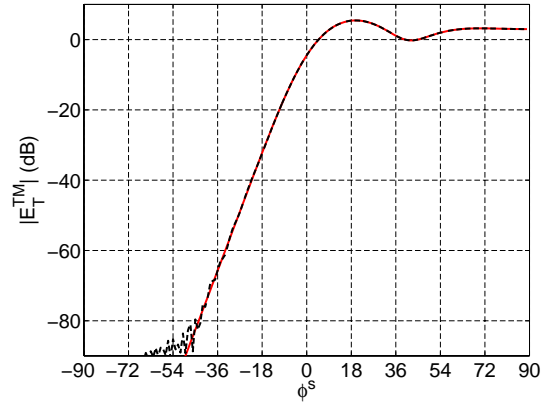
(a) $|E_T^{TM}|$
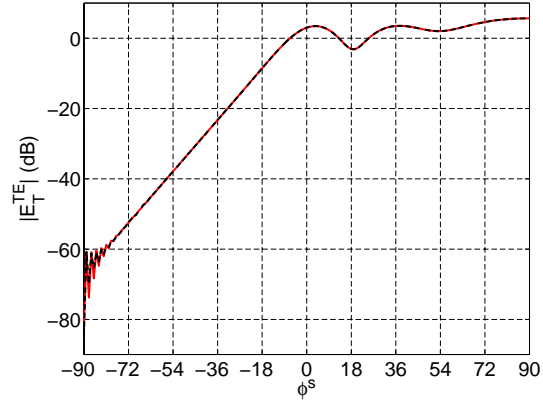
(b) $|E_T^{TE}|$

Figure 4.6: Magnitude (dB) of total E-fields 1λ off the surface of a 100λ PEC cylinder excited by a plane wave at oblique incidence angle, $\theta^i = \pi/4$, eigensolution (———), macromodel (- - - - - -) with $-90°$ corresponding to deep shadow and $90°$ corresponding to normal incidence (deep lit).
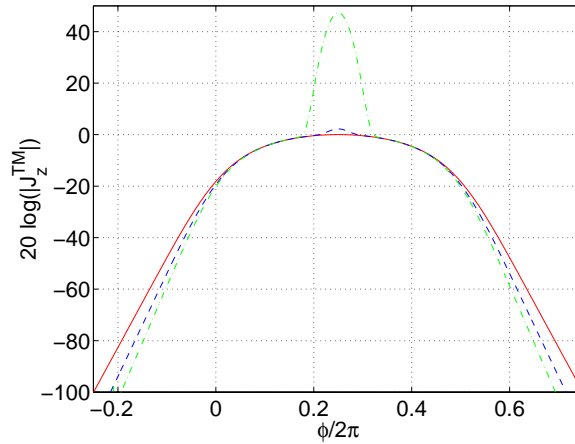
(a) $|J_z^{TM}|$
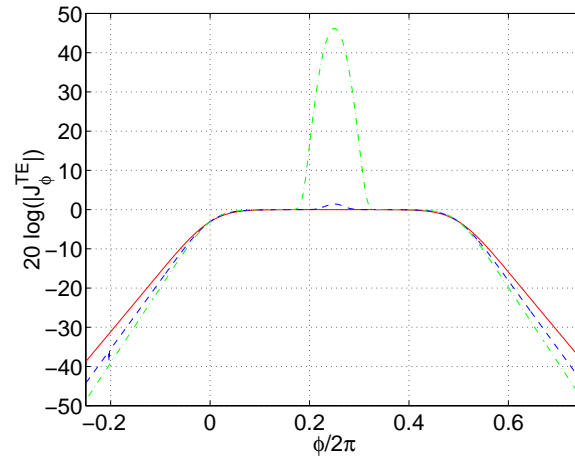
(b) $|J_\phi^{TE}|$

Figure 4.7: Total current magnitude (dB) of Fock currents around full circumference of a PEC cylinder excited at normal incidence angle, $\theta^i = \pi/2$, $a = 10\lambda$ (———), $a = 15\lambda$ (- - - - - -), $a = 20\lambda$ (— · — · —). $\frac{\phi}{2\pi} = 0$ is equivalent to a point on top of the cylinder, perpendicular to the shadow boundary, with $\frac{\phi}{2\pi} = -0.25$ in the deep shadow region.
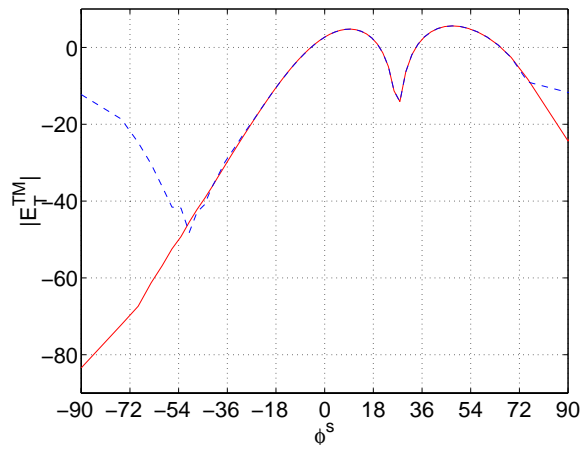
Figure 4.8: Magnitude (dB) of total TM E-fields 1λ off the surface of a 15λ PEC cylinder excited by a plane wave at normal incidencd $\theta^i = \pi/2$, macromodel (————), Fock integrals (- - - - - -) with $-90°$ corresponding to deep shadow and $90°$ corresponding to normal incidence (deep lit).
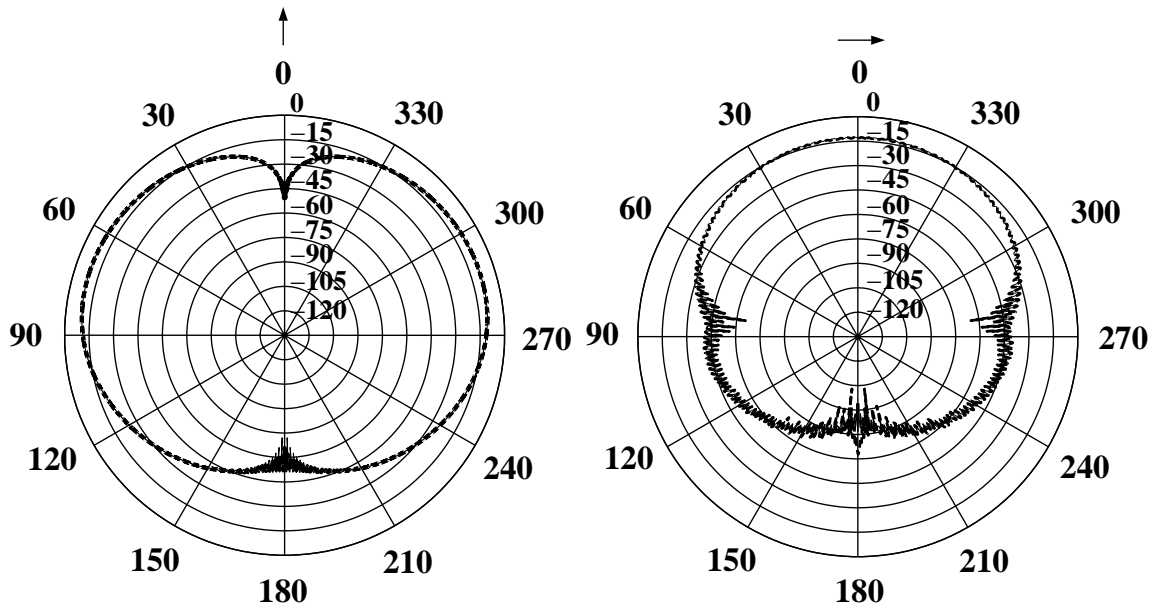
(a) $|E_\phi^s|$, Far-field, x - directed dipole

(b) $|E_\phi^s|$, Far-field, y - directed dipole
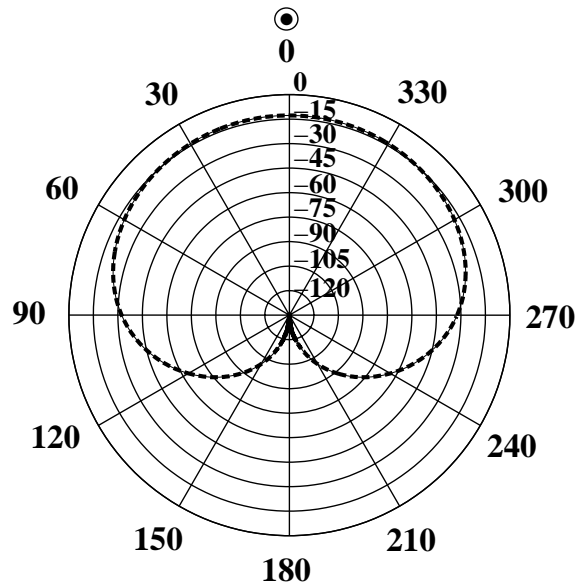
(c) $|E_z^s|$, Far-field, z - directed dipole

Figure 4.9: Magnitude (dB) of total far-fields generated by a point source (small dipole) radiating in the presence of a 20λ PEC cylinder positioned 0.1λ off cylinder surface along the x axis ($0°$ in plot) at $z = 0$. Observation is at $2(2a)^2/\lambda$ from cylinder center and in $x - y$ plane at $z = 0$, eigensolution (————), macromodel (- - - - - -).

113

CHAPTER 5

Diffraction from Convex Surfaces

In the preceding chapter a novel approach, based on the Physical Theory of Diffraction (PTD) and Fock theory was developed to macromodel the induced surface currents on a right circular, PEC cylinder, when excited by a plane wave. The proposed method generated highly accurate surface currents without the need for complex mathematical analysis, or numerical evaluation of integrals. For the case of a general convex surface, infinite in one dimension, and with large, slowly varying radius of curvature, the induced surface currents on a circular cylinder can be applied locally to approximate those induced on the convex surface. In this chapter the macromodel for the induced surface currents on a right circular PEC cylinder will be applied to approximate the currents induced on a general convex surface, infinite in one dimension, which can represent the effect of natural obstacles, such as hills, mountains, or ridgelines on the propagating radio wave. In the sections that follow the macromodel will be extended to a general convex surface in a standard way, as found in the literature [43], by applying the induced surface currents from a circular cylinder locally, on the convex surface. To validate the technique on a non-circular cylinder, results are generated for the fields scattered from an elliptical cylinder using the macromodeled currents and compared to those generated by a Method of Moments (MoM) numerical code. Curves are then shown for the fields scattered by a parabolic hill and compared to those generated using the Kirchhoff (knife-edge) diffraction method.

5.1 Introduction

As mentioned in the previous chapter, many natural terrain features exhibit both curved and doubly curved surfaces. Ridgelines in mountainous areas can exhibit the features of a long, singly curved surface (see Figure 5.1), which is essentially infinite in one dimension. Current methods of propagation prediction for natural obstacles tend to be either overly
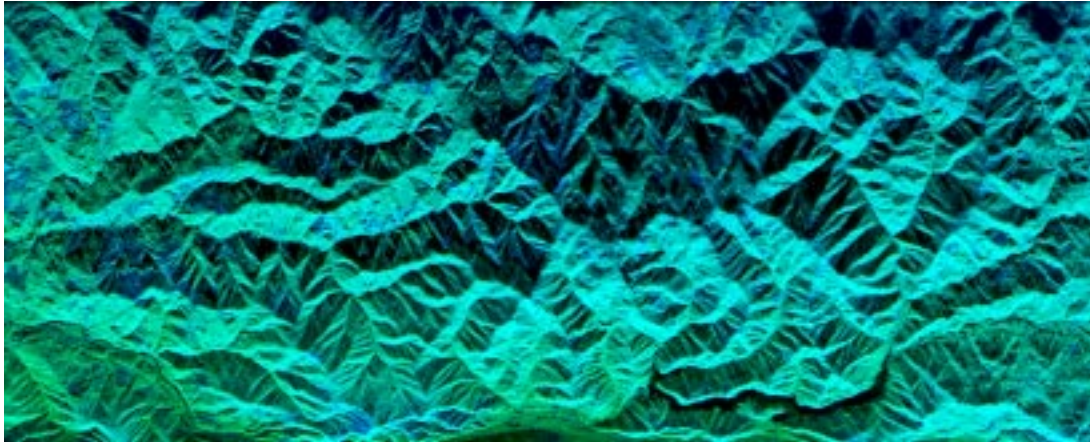
Figure 5.1: Ridgelines in Mountainous Region

simplistic, such as Kirchhoff (knife-edge) diffraction, or do not account for the curvature of the obstacle, such as wedge diffraction. High frequency techniques, while accounting for the radius of curvature of the obstacle, are mathematically complex, and can be numerically cumbersome, as was seen in the last chapter in evaluating the Fock type integrals for induced surface currents. In addition techniques such as the Uniform Theory of Diffraction (UTD) have been shown to have serious limitations in accuracy, and in essence are not asymptotic in the high frequency limit, as cylinder radius increases. Details of the problems and limitations of these techniques have been throughly discussed in the previous chapter and will not be repeated here. Suffice to say that the need for an alternate method to predict scattering and diffraction from convex surfaces of large radius of curvature is apparent. With this as a motivation a macromodel for the induced surface currents on a PEC right circular cylinder was developed in the last chapter. The proposed macromodel is simple, easy to implement, and most important, shown to be highly accurate. In this chapter the

macromodeled currents from the circular cylinder will be applied in a standard fashion, to approximate the induced surface currents on a singly curved (infinite in one dimension) convex surface, with large slowly varying radius of curvature.

5.2   Induced Surface Currents: General Convex Surface

The macromodel for the surface currents induced on a right circular PEC cylinder, when excited by a plane wave, are extended to that of a general convex surface by assuming that the surface currents induced on the convex surface can be approximated locally by those induced on a circular cylinder. This is a valid approximation provided that the convex surface is of large, slowly varying radius of curvature. To extend the macromodel to a general convex surface, and referring to the geometry as shown in Figure 5.2, modifications are made to the following parameters, defined in the previous chapter for the circular cylinder.
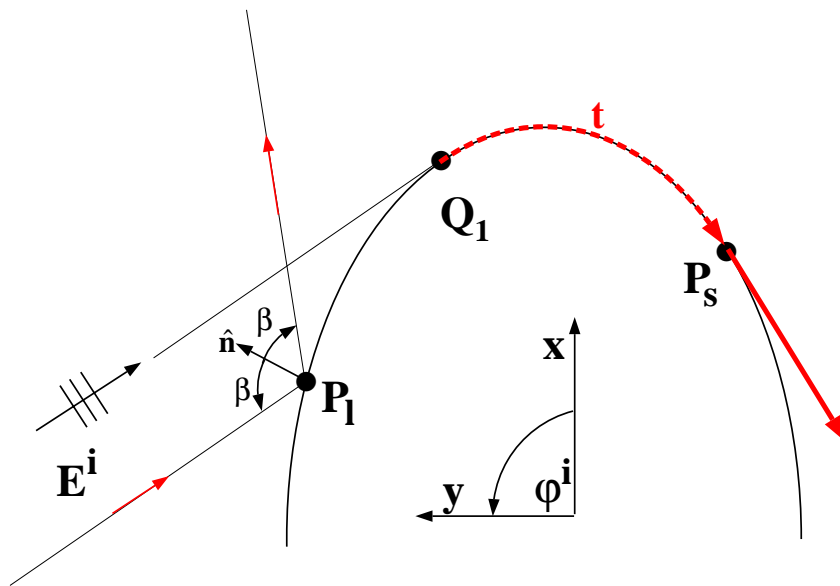
Figure 5.2: Geometry of a General Convex Surface

In all regions:

Circular Cylinder:

$$m = \left(\frac{k_0 a}{2}\right)^{(1/3)} \tag{5.1}$$

General Convex Surface:

$$m(r_c(P)) = \left(\frac{k_0 r_c(P)}{2}\right)^{(1/3)}, \tag{5.2}$$

where $r_c(P)$ is the local radius of curvature of the surface, evaluated at some point P on the surface, and where P_l and P_s indicate the point P evaluated in the lit region, or shadow region, respectively.

In the lit region:

Circular Cylinder:

$$Z' = -m\cos\phi \tag{5.3}$$

General Convex Surface:

$$Z' = -m\cos\beta, \tag{5.4}$$

where β is the angle between the incident ray and the surface normal.

In the shadow region:

Circular Cylinder:

$$Z = -m\phi \tag{5.5}$$

General Convex Surface:

$$Z = \int_{Q_1}^{P_s} \frac{m(r_c(\tau))}{r_c(\tau)} \, d\tau = \left(\frac{k_0}{2}\right)^{1/3} \int_{Q_1}^{P_s} \frac{d\tau}{r_c(\tau)^{2/3}}, \tag{5.6}$$

$$t = \int_{Q_1}^{P_s} d\tau, \tag{5.7}$$

$$\gamma = \left[\frac{r_c(P_s)}{r_c(Q_1)}\right]^{1/6}. \tag{5.8}$$

On a general convex surface the creeping wave sheds energy as a function of arclength (parameter τ in (5.6)), thus (5.6) is the more general equation, valid for any convex surface and reduces to (5.5) for the special case of a right circular cylinder. In (5.7) t is the arclength along the convex surface from the shadow boundary at point Q_1 to P_s, and γ in (5.8) is a multiplicative factor applied in the shadow region so that the Fock currents reduce to Keller's Geometrical Theory of Diffraction (GTD) formulation in the deep shadow region [42, 43]. It is not clear in the literature how the parameter γ is arrived at, either by derivation or empirically, only that it is necessary for the expressions in the deep shadow to uniformly reduce to Keller's solution.

5.3   Results: Diffraction from Convex Surfaces

5.3.1   Ellipse

To validate the extension of the macromodeled surface currents to a general convex surface, the technique will first be applied to an elliptical cylinder, for the 2-D case ($\theta^i =$

90°) and compared with results obtained from a MoM code. The geometry is as shown in Figure 5.3, with *a* and *b* describing the dimensions of the ellipse along the *y* and *x* axes respectively, with ϕ^i the incidence angle. Figure 5.4 shows the results for an ellipse with y-dimension $a = 10\lambda$ and x-dimension $b = 8\lambda$, with incident angle $\phi^i = 90^\circ$. The results shown are the total fields (direct + scattered) observed 1λ off the surface of the ellipse and observation is a function of the y-dimension in the figure. Figure 5.4a shows the TM *z*
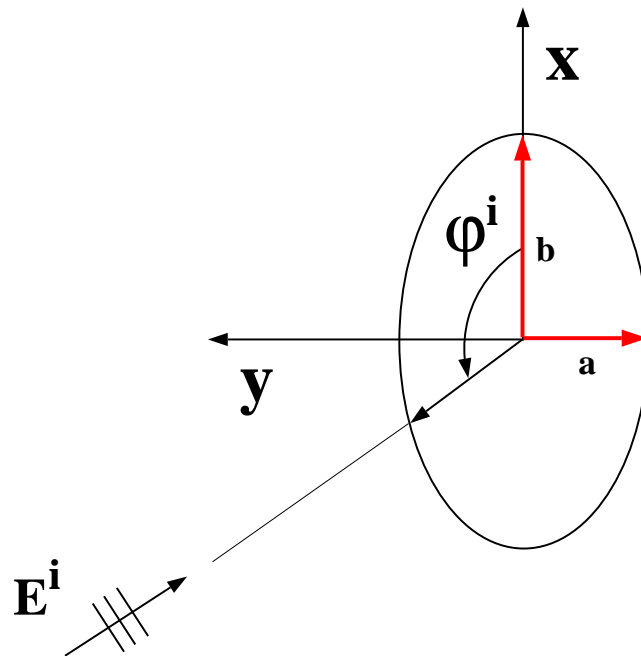
Figure 5.3: Geometry of Elliptical Cylinder

field component, with Figure 5.4b and Figure 5.4c showing the *x* and *y* components of TE polarization, respectively. As can be seen in Figure 5.4 the total fields generated by the macromodel are in good agreement with those generated by the MoM code. A note of interest about these results. The fields generated by the macromodeled surface currents as well as the fields generated by the MoM code for the TM case were done with a current sampling rate of 10 samples/wavelength. To produce acceptable results for the TE case the current sampling for the MoM code had to be increased to 30 samples/wavelength. This is due to the fact that the Green's function for the TE case contains higher order derivatives

and evaluation of these derivatives in the TE MoM code are done numerically instead of evaluation of the analytic expressions for the derivatives. Figure 5.5 shows results for the same test case but with the y and x dimensions of the ellipse interchanged, or $a = 8\lambda$ and $b = 10\lambda$. Again the total field results from the macromodeled current are in good agreement with those generated by the MoM code. In Figures 5.6 and 5.7 the results are shown for a similar test case, but with an increased axial ratio of the ellipse. Figure 5.6 shows results for ellipse dimensions of $a = 10\lambda$ and $b = 5\lambda$, with Figure 5.7 showing results for $a = 5\lambda$ and $b = 10\lambda$. Again for both cases incident angle $\phi^i = 90°$. As can be seen in all plots there is again good agreement between total fields generated by both methods.

In order to examine the effect of even more extreme axial ratio on the accuracy of the macromodel Figures 5.8 and 5.9 again compare the fields generated by the macromodel those generated by the MoM code for an ellipse with $a = 10\lambda$ and $b = 3.33\lambda$ and $a = 10\lambda$ and $b = 2.5\lambda$, respectively. As can be seen in these figures while the accuracy of the macromodel begins to degrade as expected, there is still reasonably good agreement between the curves except in the deep shadow for the TM z fields and the TE x fields.

Finally in this section results are generated with the incidence angle $\phi^i = 45°$. This is an interesting case as the surface currents on the ellipse are no longer symmetric about the shadow boundary. Figures 5.10 and 5.11 show results for an ellipse with $a = 10\lambda$ and $b = 8\lambda$ and $a = 8\lambda$ and $b = 10\lambda$, respectively. Note that observation in these plots is a function of angular dimension ϕ. Again good agreement is observed between the total fields generated with the macromodeled currents when compared to those generated by the MoM numerical code.

(a) $|E_z^{TM}|$

(b) $|E_x^{TE}|$

(c) $|E_y^{TE}|$

Figure 5.4: Magnitude (dB), total fields 1λ off the surface of an ellipse, with y-dimension $a = 10\lambda$, x-dimension $b = 8\lambda$. Incidence angle ϕ^i is at $90°$, MoM solution (————), compared with macromodel (- - - - - -).

(a) $\left|E_z^{TM}\right|$

(b) $\left|E_x^{TE}\right|$

(c) $\left|E_y^{TE}\right|$

Figure 5.5: Magnitude (dB), total fields 1λ off the surface of an ellipse, with y-dimension $a = 8\lambda$, x-dimension $b = 10\lambda$. Incidence angle ϕ^i is at $90°$, MoM solution (————), compared with macromodel (- - - - - -).

(a) $|E_z^{TM}|$

(b) $|E_x^{TE}|$

(c) $|E_y^{TE}|$
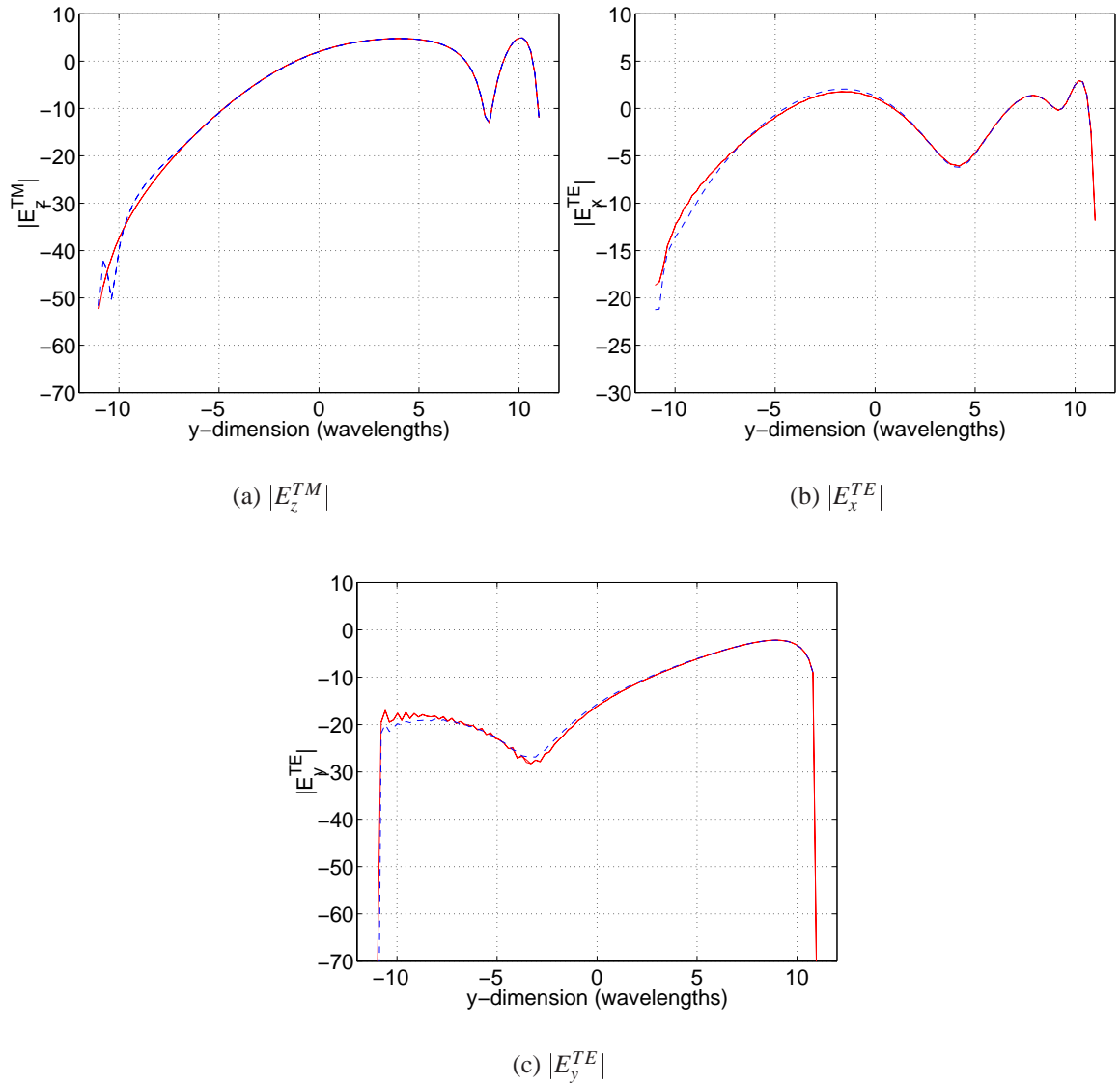
Figure 5.6: Magnitude (dB), total fields 1λ off the surface of an ellipse, with y-dimension $a = 10\lambda$, x-dimension $b = 5\lambda$. Incidence angle ϕ^i is at $90°$, MoM solution (————), compared with macromodel (- - - - - -).

(a) $|E_z^{TM}|$

(b) $|E_x^{TE}|$

(c) $|E_y^{TE}|$
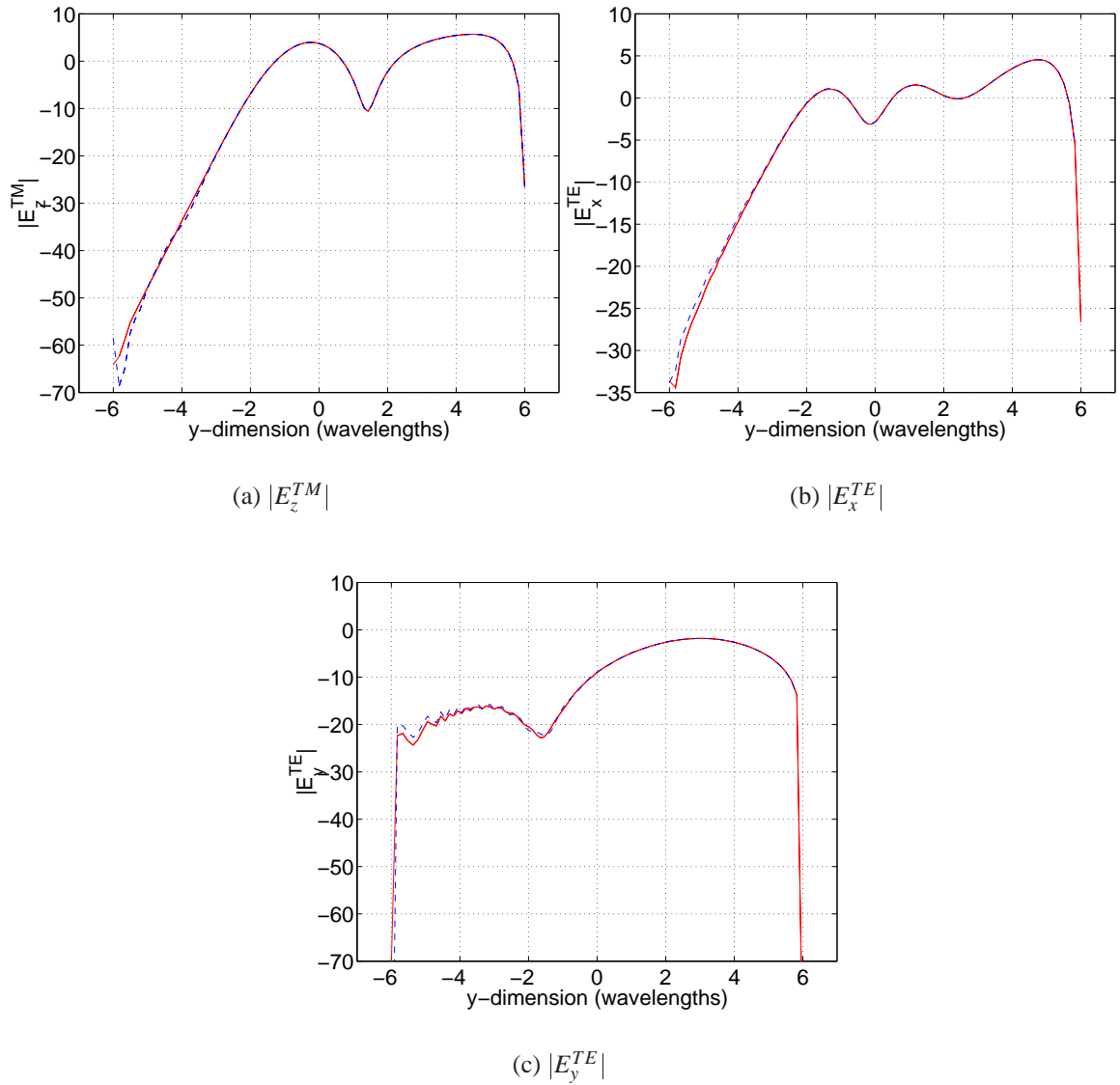
Figure 5.7: Magnitude (dB), total fields 1λ off the surface of an ellipse, with y-dimension $a = 5\lambda$, x-dimension $b = 10\lambda$. Incidence angle ϕ^i is at $90°$, MoM solution (———), compared with macromodel (- - - - - -).

(a) $|E_z^{TM}|$

(b) $|E_x^{TE}|$

(c) $|E_y^{TE}|$
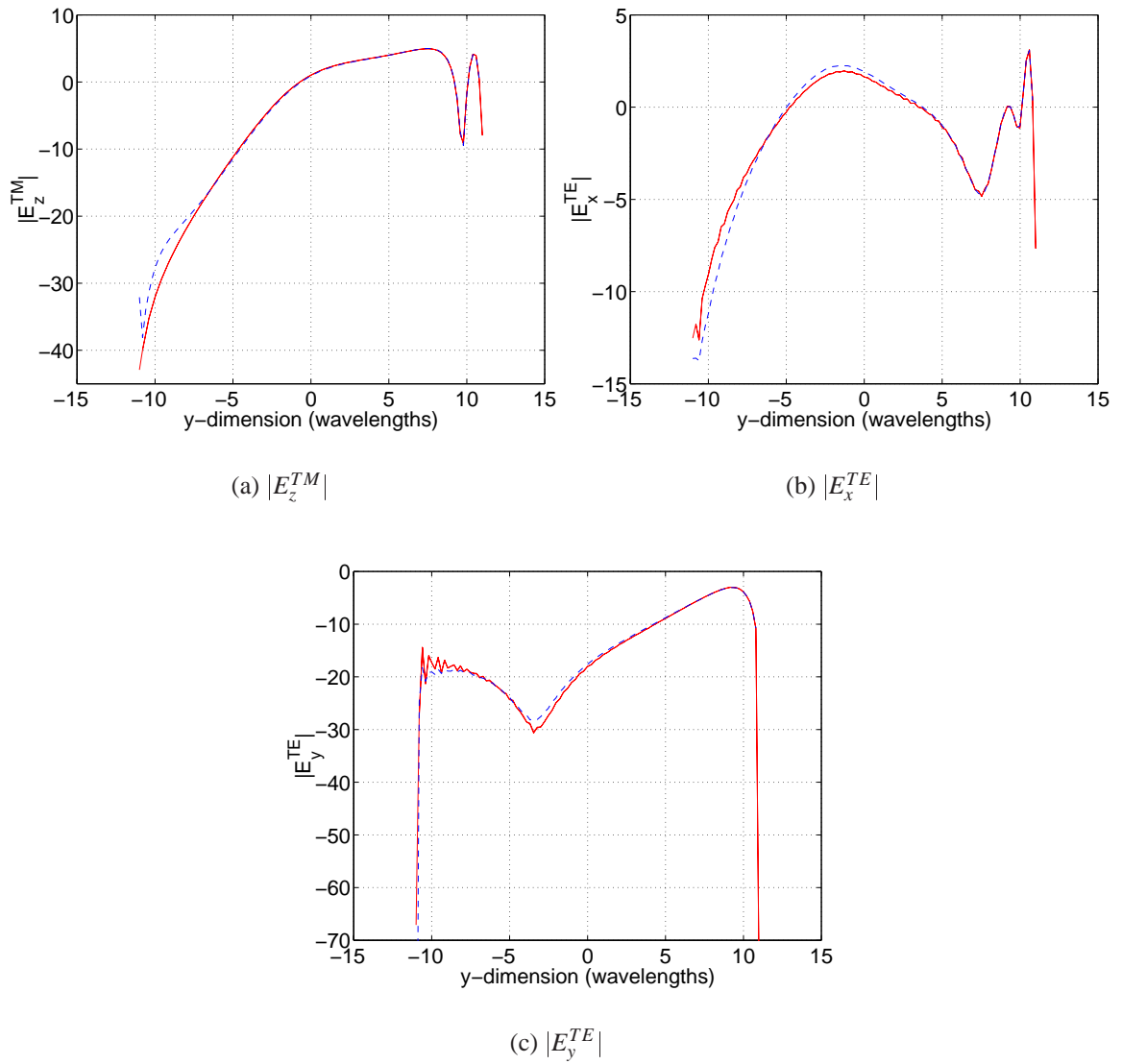
Figure 5.8: Magnitude (dB), total fields 1λ off the surface of an ellipse, with y-dimension $a = 10\lambda$, x-dimension $b = 3.33\lambda$. Incidence angle ϕ^i is at 90°, MoM solution (———), compared with macromodel (- - - - - -).

(a) $|E_z^{TM}|$

(b) $|E_x^{TE}|$

(c) $|E_y^{TE}|$
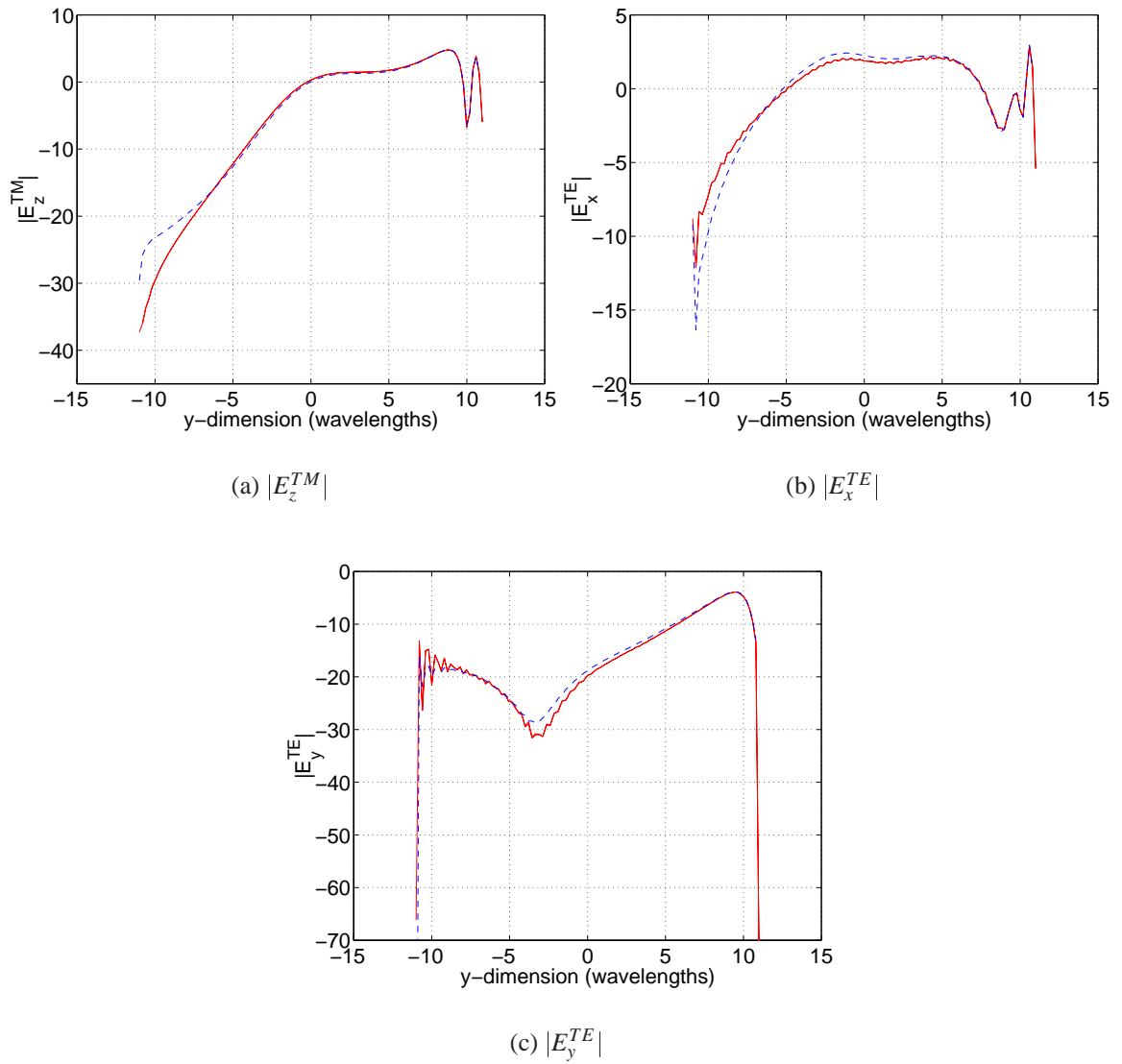
Figure 5.9: Magnitude (dB), total fields 1λ off the surface of an ellipse, with y-dimension $a = 10\lambda$, x-dimension $b = 2.5\lambda$. Incidence angle ϕ^i is at $90°$, MoM solution (————), compared with macromodel (- - - - - -).

(a) $|E_z^{TM}|$

(b) $|E_x^{TE}|$

(c) $|E_y^{TE}|$
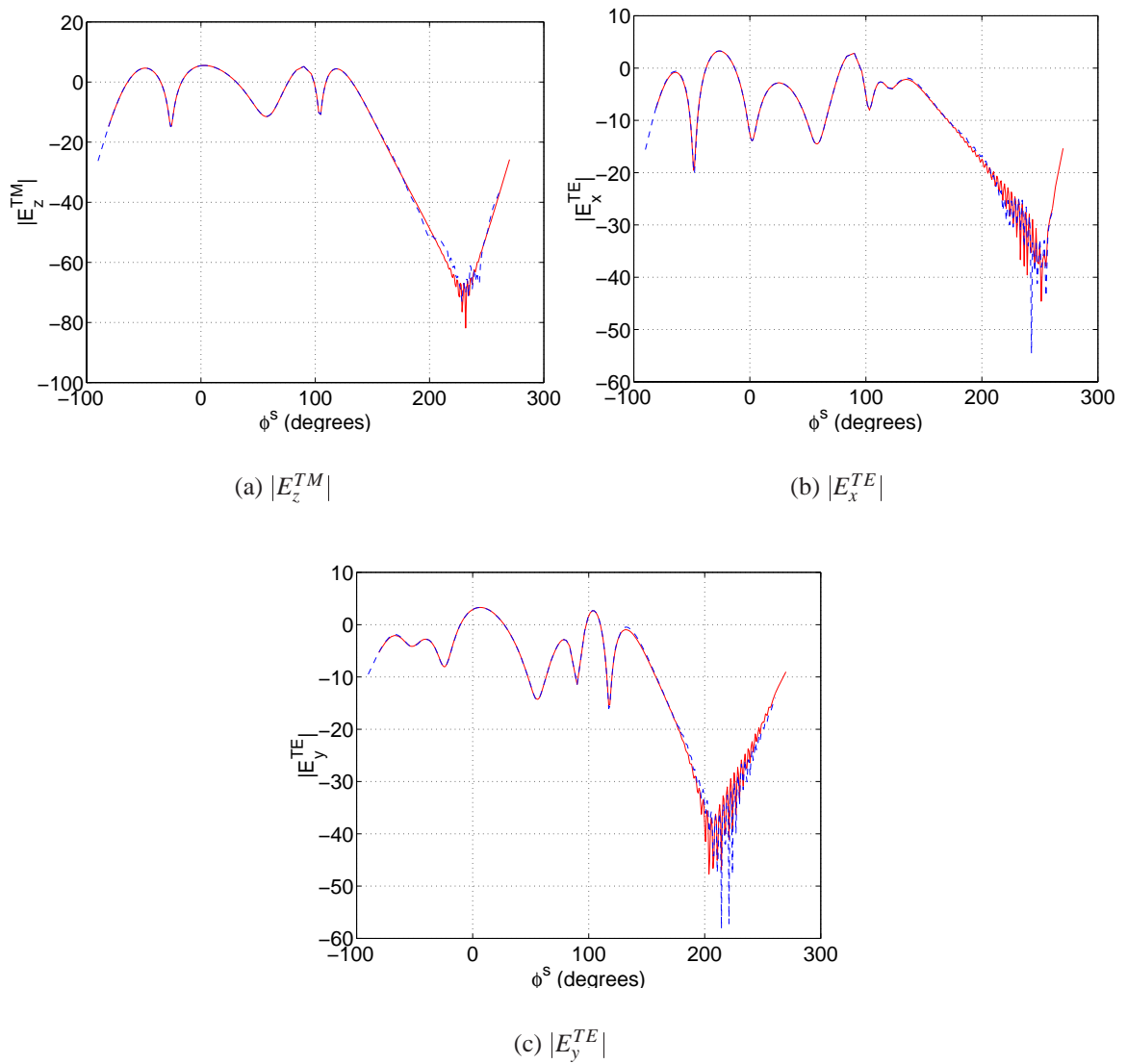
Figure 5.10: Magnitude (dB), total fields 1λ off the surface of an ellipse, with y-dimension $a = 10\lambda$, x-dimension $b = 8\lambda$. Incidence angle ϕ^i is at 45°, MoM solution (————), compared with macromodel (- - - - - -).
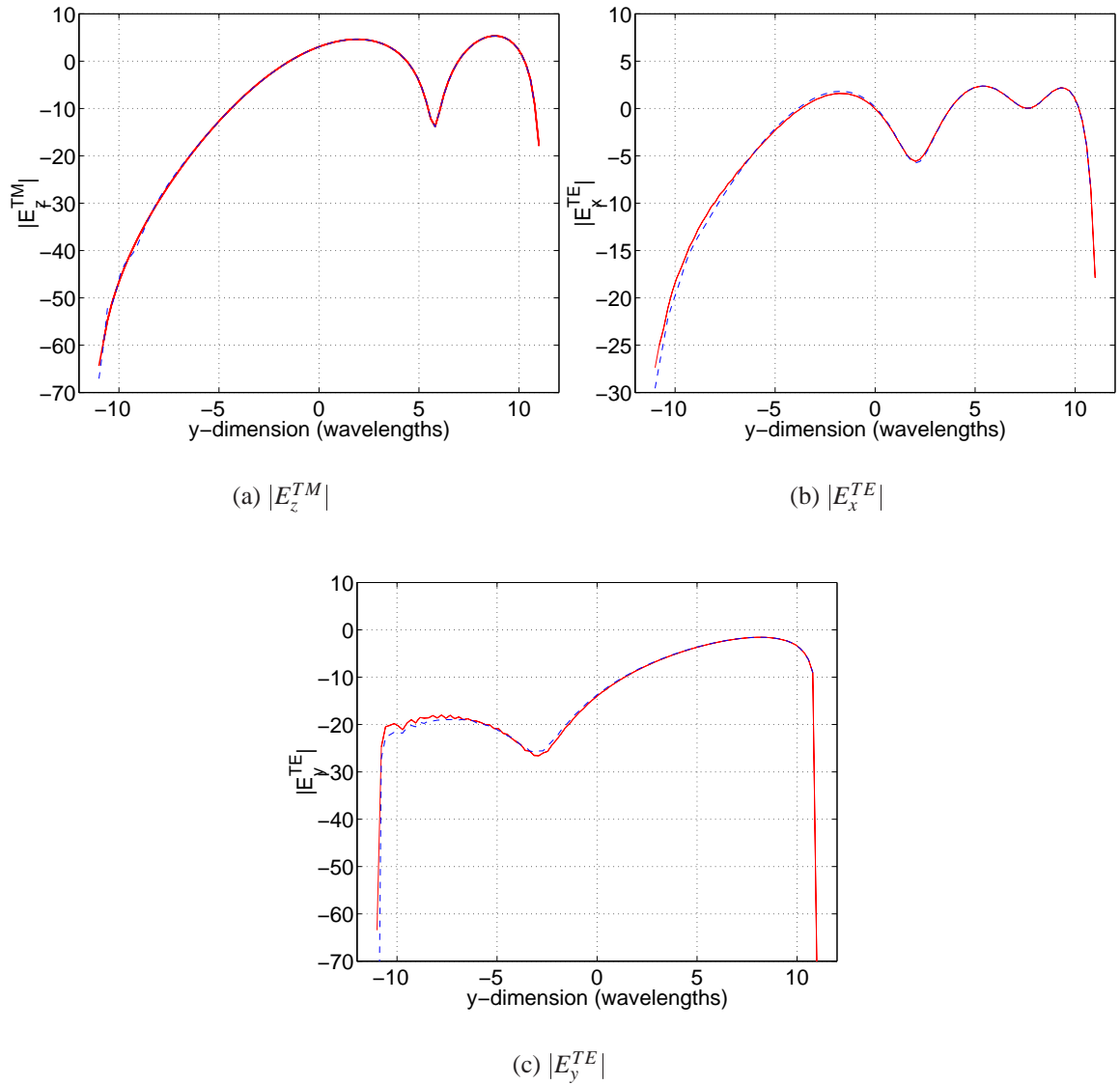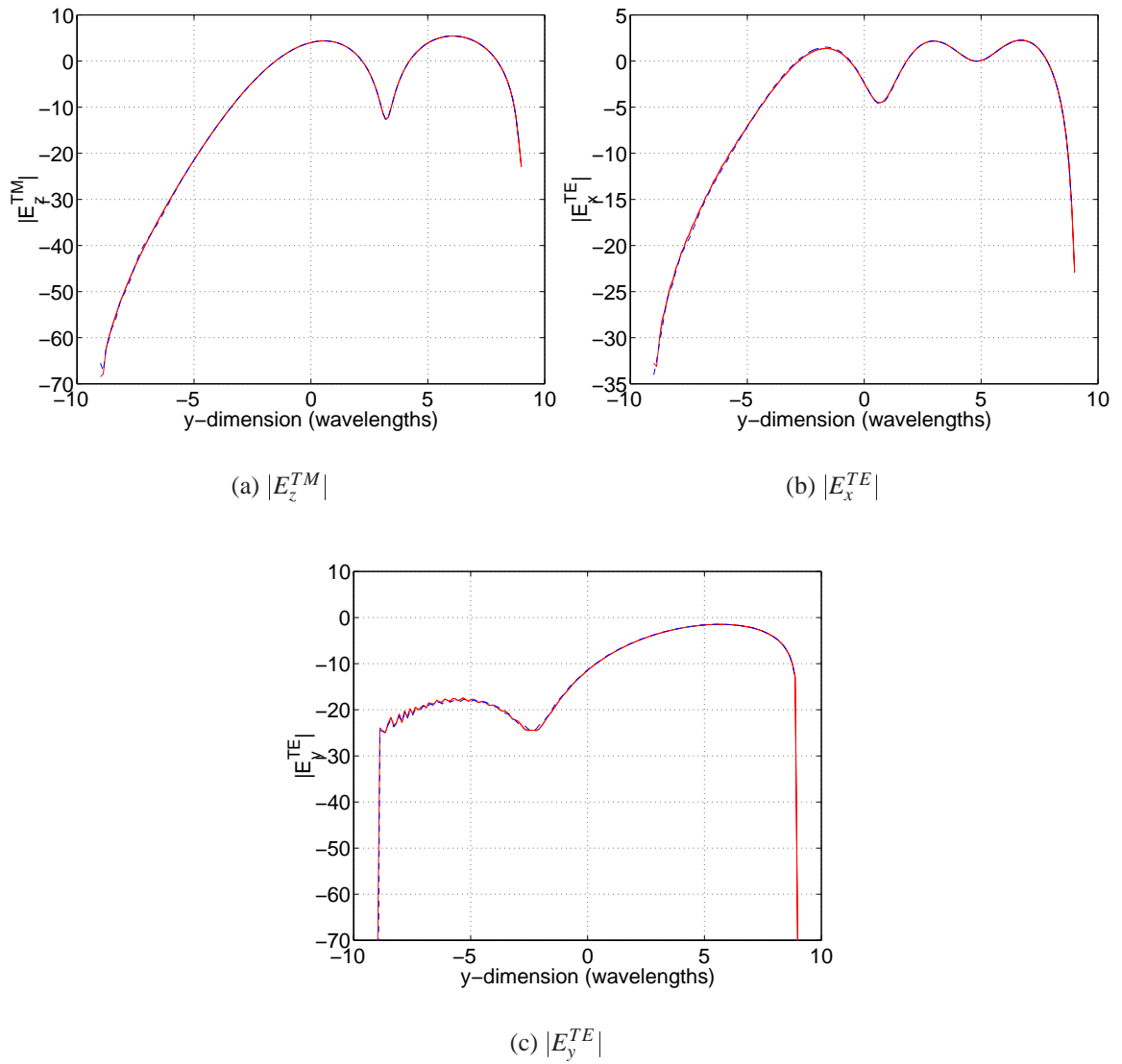
(a) $|E_z^{TM}|$

(b) $|E_x^{TE}|$

(c) $|E_y^{TE}|$
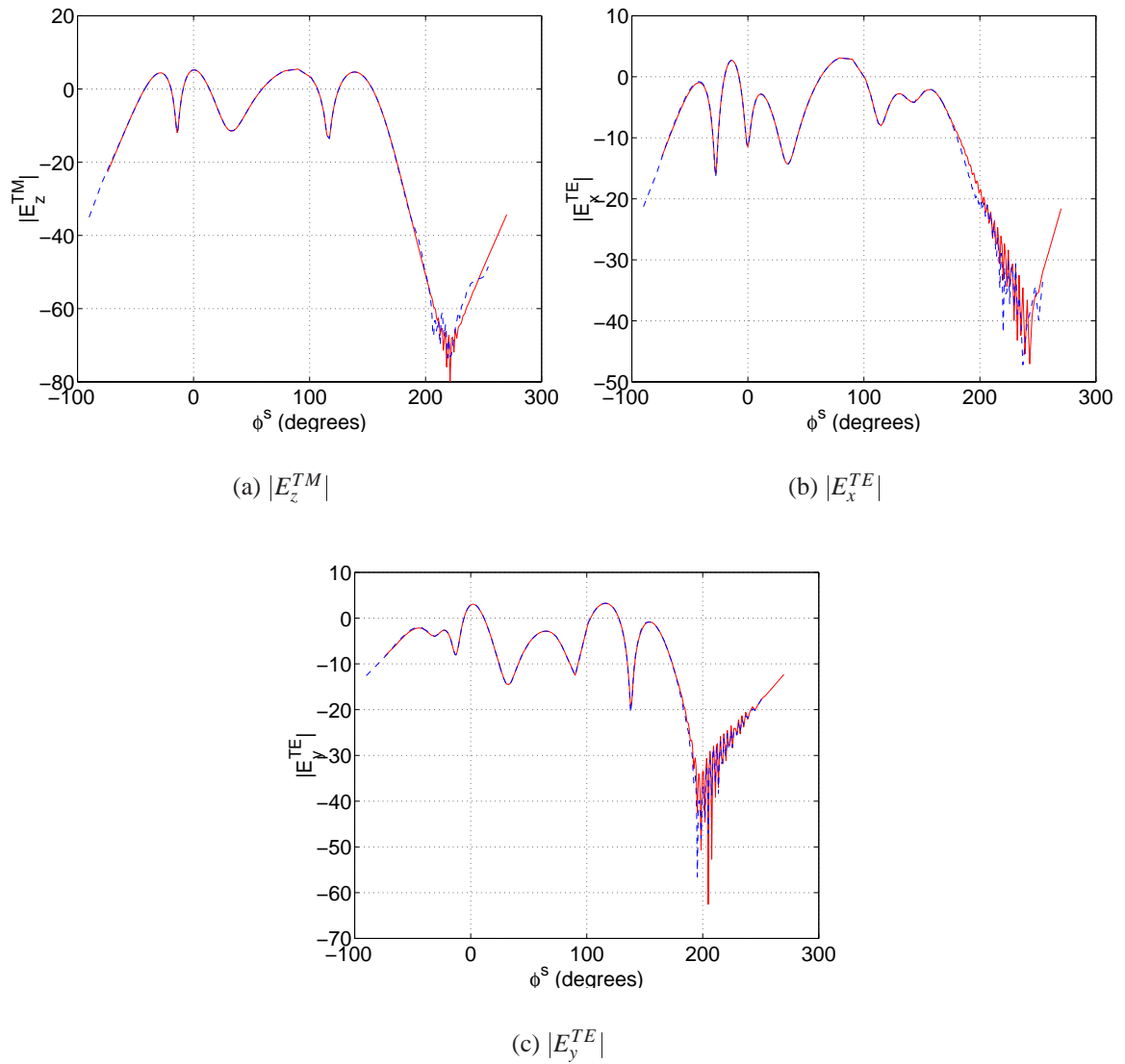
Figure 5.11: Magnitude (dB), total fields 1λ off the surface of an ellipse, with y-dimension $a = 8\lambda$, x-dimension $b = 10\lambda$. Incidence angle ϕ^i is at $45°$, MoM solution (————), compared with macromodel (- - - - - -).

5.3.2 Knife-edge (Kirchhoff) Diffraction

A commonly used technique in predicting path loss from terrain obstacles is knife-edge or Kirchhoff diffraction. Based on Huygen's principle, the obstacle is represented by a blocking screen and the field distribution across the resulting aperture (from the top of the screen, vertically to infinity) integrated to produce the diffracted fields. The technique is a 2-D method (does not account for oblique incidence) and assumes that both the source and observation are very distant from the obstacle. It is a scalar method (does not account for polarization effects) and cannot account for surface effects such as reflected fields or creeping waves. Also it does not account for the impedance of the surface. Based on the assumption that both source and observation are distant from the obstacle the following expression, in the form of a Fresnel integral, can be derived for path loss by applying knife-edge diffraction techniques, [49].

$$\textbf{Path loss} = \frac{\sqrt{2}}{2} \left| \int_{-H_c}^{\infty} e^{-i\pi u^2/2} \, du \right|, \tag{5.9}$$

where,

$$H_c = \left(\frac{2(R_0 + |y|)}{\lambda R_0 |y|} - \frac{2i}{\pi \gamma^2} \right)^{1/2} h_o. \tag{5.10}$$

In (5.10) R_0 is the horizontal distance from source to the blocking screen (perpendicular to screen), y the horizontal distance from observation to screen, λ the free space wavelength, γ a decay factor, representing a Gaussian field distribution across the aperture, and h_o the vertical distance from observation to the top of the screen (see Figure 5.12 for geometry details). Note that H_c in (5.9) and (5.10) is positive when observation is above the screen and negative below. The geometry of the problem for both the convex surface and knife-edge are shown in Figure 5.12. The convex obstacle is represented by a parabolic surface of height h and width w, defined at the base of the surface ($x = 0$ in Figure 5.12). To minimize
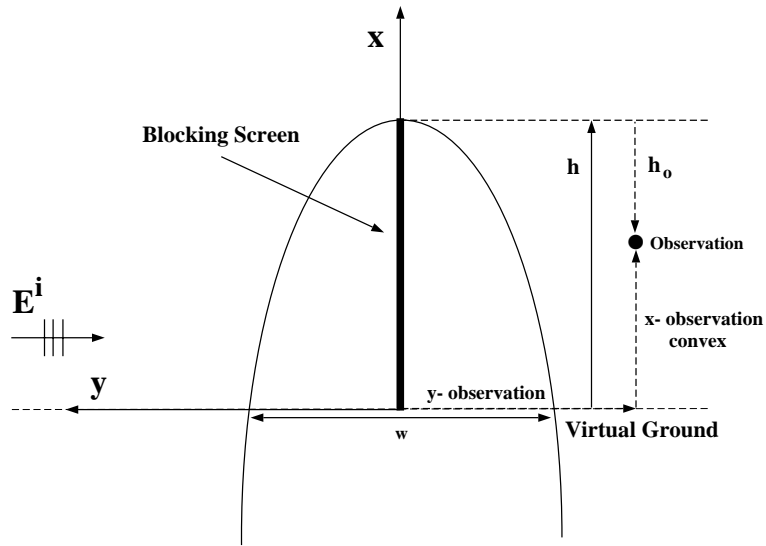
Figure 5.12: Scattering Geometry, Knife-edge and Convex Surface

edge effects the parabolic surface is extended below a virtual ground ($x < 0$) and the surface currents tapered by a cosine function below this point. For all results that follow the angle of incidence for the convex surface is $\phi^i = 90°$ (normal to the screen, see Figure 5.2) and the source position, R_o for the knife edge is assumed to be distant so that plane wave incidence can be assumed. Also the weighting parameter γ in (5.10) is set at 1000λ or essentially a uniform aperture distribution.

If the blocking obstacle is much narrower in width than height it is assumed that knife-edge diffraction should produce somewhat acceptable results provided that the observation point in the shadow region is distant from the actual obstacle, although since knife-edge diffraction is scalar diffraction, it will not properly predict the location of the ringing positions in the lit regions. As the width of the obstacle is increased these results should begin to degrade even further when compared with results from the macromodel for convex surfaces, especially in the deep shadow of the obstacle. This can be seen in Figures 5.13 through 5.15. To generate these results the observation position was placed at $y = -51\lambda$ (see Figure 5.12) and moved vertically from $x = 0$ to $x = 100\lambda$. The height of the obstacle was set at 50λ. Figure 5.13 shows results from the macromodel, with width of the convex

surface set at $w = 6\lambda$, compared with the knife-edge results (note that this width produces a radius of curvature at the shadow boundary of approximately 1λ, the minimum radius of curvature for which the macromodel can be assumed to be accurate). Figure 5.13a shows a comparison of the z-component of the TM fields (total fields) with the knife-edge results, with Figure 5.13b comparing the knife-edge results to the x-component of the TE fields. As can be seen in Figure 5.13a, for the TM case, the knife-edge calculations produced somewhat acceptable in the lit region and through the transition region (again without properly predicting the position of the ringing in the lit region) for this case of a very narrow obstacle, although its accuracy begins to degrade in the deep shadow region as expected. The results for the TE case, in Figure 5.13b, shows similar discrepancies. Figure 5.14 and Figure 5.15 show similar results, with the width of the obstacle widened to 50 and 100λ respectively. As expected the knife-edge results begin to degrade in the shadow region as the width of the obstacle is increased, and the degradation tends to approach the transition region and shadow boundary.

(a) $|E_z^{TM}|$ (b) $|E_x^{TE}|$
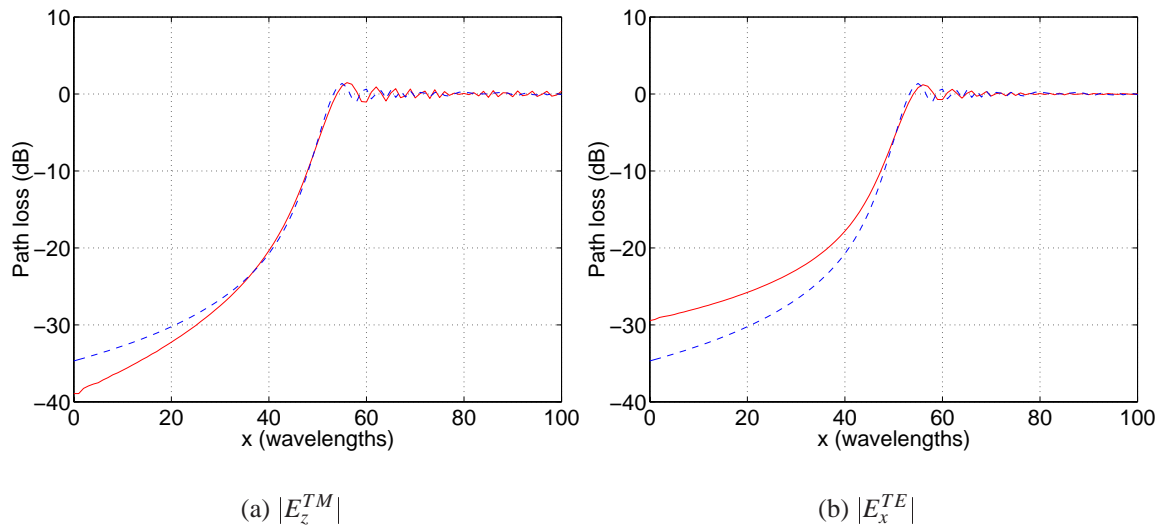
Figure 5.13: Path loss (dB), total fields from an obstacle of height $h = 50\lambda$, and width $w = 6\lambda$. Observation is at $y = -51\lambda$ and incident angle is at $\phi^i = 90°$ (normal to the screen). Macromodel (————), compared with knife-edge (Kirchhoff) diffraction (- - - - - -).

(a) $|E_z^{TM}|$

(b) $|E_x^{TE}|$
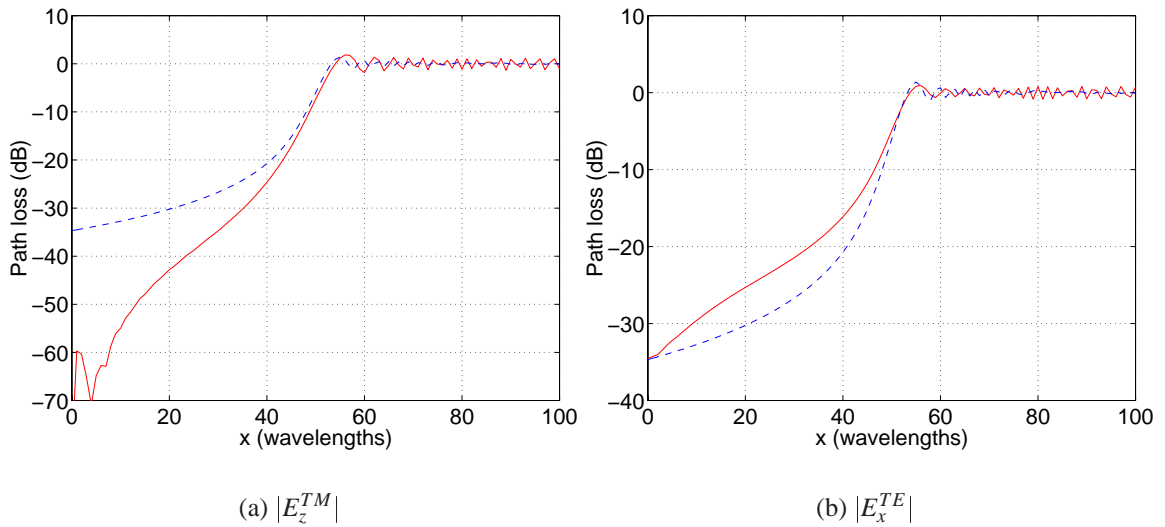
Figure 5.14: Path loss (dB), total fields from an obstacle of height $h = 50\lambda$, and width $w = 50\lambda$. Observation is at $y = -51\lambda$ and incident angle is at $\phi^i = 90°$ (normal to the screen). Macromodel (———), compared with knife-edge (Kirchhoff) diffraction (- - - - - -).

(a) $|E_z^{TM}|$

(b) $|E_x^{TE}|$
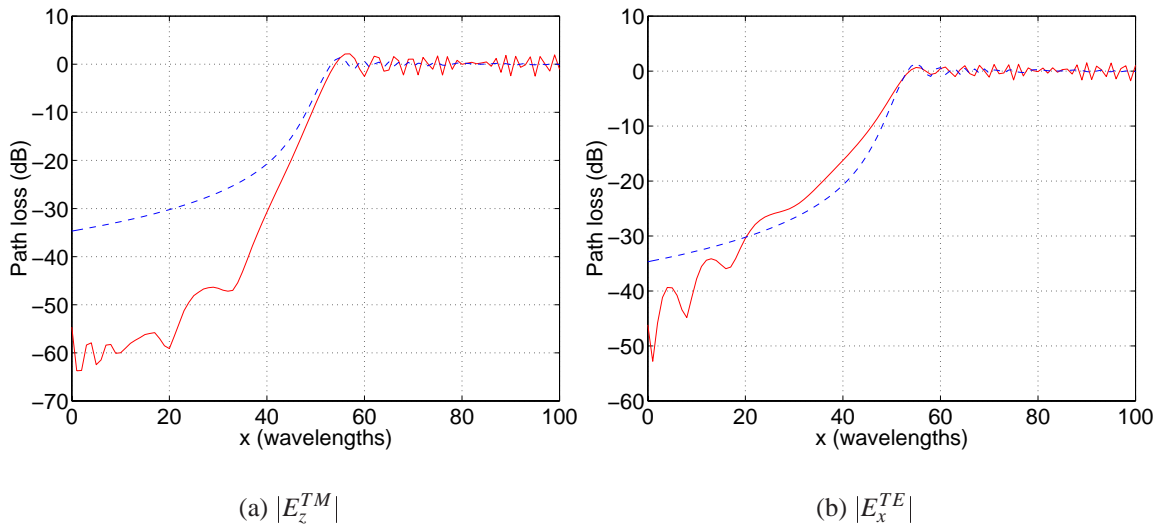
Figure 5.15: Path loss (dB), total fields from an obstacle of height $h = 50\lambda$, and width $w = 100\lambda$. Observation is at $y = -51\lambda$ and incident angle is at $\phi^i = 90°$ (normal to the screen). Macromodel (———), compared with knife-edge (Kirchhoff) diffraction (- - - - - -).

5.4   Chapter Summary: Diffraction from Convex Surfaces

In this chapter the macromodel developed in Chapter 4, for predicting the induced surface currents on a right circular PEC cylinder, when excited by a plane wave at oblique angles, was extended to the case of a general convex surface. Recognizing that the induced surface currents on a circular cylinder can be applied locally on a surface with large, slowly varying radius of curvature, the method was extended to a general convex surface by application of standard methods found in the literature. The case of an elliptical cylinder was first examined and the proposed macromodel showed good agreement when compared to results generated by a MoM numerical code. The macromodel was then applied to a parabolic surface and compared to results generated by using knife-edge or Kirchhoff diffraction. As expected the knife-edge method produced somewhat acceptable results for a very narrow obstacle, but as the obstacle was widened, results from the knife-edge method began to degrade, especially in the shadow region and into the transition region.

CHAPTER 6

Summary & Future Work

As previously discussed, the ability to predict the propagation of radio waves in an accurate and general fashion is essential in the performance analysis and optimal design of a communications system. Without an accurate and general model, system issues such as coherency, field variations, multipath, and path delay effects cannot be properly addressed. Existing methods in propagation or channel modeling tend to be heuristic or overly simplistic and do not adequately address the relevant issues for optimal system design. Due to the discussed shortcomings in current techniques for the prediction of radio wave propagation, a more general approach or methodology, directly based on the physics of the propagation problem is defined. The basis of the methodology is, through the application of electromagnetic wave theory, to develop a series of canonical scattering and diffraction models which represent the effects of various mechanisms in the propagation environment, on the radio wave. Depending on the problem at hand the appropriate technique is applied whether it be analytic, numeric, or a hybrid technique. Relevant approximations are made, based on the physics of the problem, which improve computational efficiency while retaining the required accuracy. Eventual merger of these canonical models with a satellite terrain database will provide the system designer with an accurate and general model to simulate the propagation environment.

Within the framework of this physics-based methodology the initial concentration or

134

focus of this thesis work was defined. It is intended that the work in this thesis be a basis for expansion into an overall propagation model, and with that in mind it was decided that the concentration of this work would be on predicting propagation in a rural environment, in the frequency range of HF to L-band, which can include point to point communication on the ground or perhaps from an unmanned aerial vehicle (UAV) to/from ground. Included in a rural environment can be the effects of a lossy earth on radio wave propagation as well as scattering and diffraction from natural obstacles such as hills, mountains, or ridgelines. In this thesis two diffraction models were developed. The first accounts for the effects of a lossy earth on the fields of a small dipole, which can include the effects of some type of impedance transition, representative of a river or land/sea transition. The second model developed determines scattering and diffraction from a general convex surface, representative of a hill, mountain, or ridgeline. In this chapter this work will be summarized as well as a discussion of future work presented.

6.1 Summary: Scattering & Diffraction from Impedance Surfaces

The prediction of radio wave propagation over the Earth's surface is important in the characterization of a communications channel. Locally the Earth can be modeled as a flat, impenetrable, impedance surface and the standard impedance boundary condition (SIBC) applied. The problem can be decomposed into the effects of the homogeneous surface and the effects of an impedance transition in the surface, such as caused by a river or land/sea interface. In Chapter 2 the effects of the homogeneous surface were addressed with the model extended to include that of an impedance transition in Chapter 3.

6.1.1 Fields of a Small Dipole Above an Impedance Surface

The fields of an infinitesimal dipole, of arbitrary orientation, above a homogeneous impedance surface is the classic Sommerfeld problem, with field expressions in the form of Sommerfeld type integrals. These integrals are highly oscillatory and difficult to evaluate numerically and the time taken to compute them discourages their application as Green's functions in integral equation techniques. With this in mind, in Chapter 2, a technique was presented to significantly improve the convergence properties of these Sommerfeld type integrals. By application of an integral transform technique known as exact image theory the Sommerfeld type integrals were transformed into a form more conducive to numerical evaluation. As no approximations are made the resulting expressions are exact in the analytic sense. Starting with a spectral domain representation of the dipole fields, and by application of appropriate identities, the expressions are modified to consist of Bessel functions of the first kind, of order zero, only. Reflection coefficients are then cast in the form of the Laplace transform of an exponential function. The spectral domain integration can then be performed analytically and the remaining integrals in the Laplace domain converge extremely rapidly, up to several orders of magnitude faster than the original Sommerfeld type expressions. Expressions for a horizontal dipole show a diverging exponential term not previously discussed in the literature. The integrand for this case however, is still dominated by a decaying exponential term and the rapid convergence properties are maintained.

6.1.2 Scattering from an Impedance Transition

Having developed a technique for efficient calculation of the fields of a dipole above a homogeneous impedance surface, the model, in Chapter 3, was extended to include the effects of a one-dimensional impedance transition in the surface, which can represent the effects of a river or land/sea transition. Current methods in use, such as the Geometrical Theory of Diffraction (GTD), are only valid for an abrupt transition and a method was

sought which is valid for any arbitrary, one-dimensional, impedance transition function. A perturbation technique is applied in which the impedance transition is represented as a perturbation in the surrounding impedance half-space. An integral equation is defined on the impedance surface and the unknown surface currents in the resulting expression expanded in terms of a perturbation parameter. For ease of analysis the resulting expressions are solved in the Fourier domain for the unknown surface currents and recursive expressions are obtained, relating higher order currents in the perturbation series to lower order in the form of multi-fold convolution. An error bound was established which shows the perturbation series to converge for a lossy surface, even for a very large perturbation parameter. All field integrals were solved by application of stationary phase techniques producing field expressions which are algebraic to first order in the perturbation series.

The technique was than applied to calculate the scattering effects of a land/sea transition on the total dipole fields. For this problem the impedance transition function was dealt with in a mean sense, i.e., the unperturbed impedance (homogeneous surface) is the mean value of the transition function. The perturbation technique inherently deals with the unperturbed impedance in this way and the assumption of a mean impedance is valid for source and observation near the impedance surface, the case of interest to us. In this case the Geometrical Optics (GO) and direct fields tend to cancel and higher order terms dominate the total dipole fields (Norton surface wave). The fields scattered from the impedance transition are now comparable to those from the homogeneous surface and thus it was shown that the transition has a significant effect even distant from the land/sea interface. For this same case, and when source and observation are also distant from each other, the observation is near grazing and tends to be near the specular direction. Analysis presented shows that the effects of the width of the land/sea transition are negligible in the specular direction and thus the transition width has no effect on the fields when source and observation are near the impedance surface. It was also shown in Chapter 3 that an apparent discontinuity in the total fields at the GO reflection boundary was an artifact of applying stationary phase

to determine the dominate spectral component or plane wave of the dipole fields which excites the transition. This single plane wave contains infinite energy across the extent of the impedance surface and therefore the Fourier transform of the impedance transition function contains infinite energy. Analysis showed that while the field levels through the reflection boundary are not discontinuous they do transition very rapidly and the fields on each side of the reflection boundary are correct.

6.2 Summary: Diffraction from Convex Surfaces

In a rural environment natural obstacles such as hills, mountains, or ridgelines can exhibit the features of a long, slowly varying curved surface, which is essentially infinite in one-dimension and can have a significant effect on radio wave propagation. Even at HF frequencies these obstacles exhibit a finite radius of curvature which must be accounted for, and currently applied techniques such as knife-edge (Kirchhoff) diffraction and wedge diffraction do not address this. To address the issue of diffraction from convex surfaces high frequency techniques are the appropriate tool, however as was shown they are mathematically complex, and can be highly inaccurate (Uniform Theory of Diffraction (UTD)). As no one high frequency technique is valid in all regions around the obstacle it was decided to work with the induced surface currents, which through the radiation integrals produce fields in all regions. For surfaces with large, slowly varying radii of curvature, the currents excited on a circular cylinder are a valid approximation to those induced on a general convex surface. While the Fock integrals can be used to calculate these induced surface currents they were shown to be numerically cumbersome and in fact impractical for calculating the currents on cylinders of even moderate radius. With this as a motivation a novel technique was introduced and developed in Chapter 4 to approximate the currents induced on the surface of a PEC right circular cylinder, when excited by a plane wave.

The induced surface currents on a cylinder can be decomposed, in the manner of the

Physical Theory of Diffraction (PTD), into a uniform or Physical Optics (PO) component and a non-uniform or diffraction component which is a correction to the PO currents. The PO currents are a form of the incident field and are know, thus the objective is to determine a model for the diffraction currents. In Chapter 4 a macromodel for the diffraction currents is developed which is simple, yet highly accurate and requires no numerical integration. Based on Fock analysis, the high frequency behavior of the induced surface currents, as a function of cylinder radius, is predicted. As shown in Chapter 4 this in practice means applying simple scaling and weighting factors to the induced surface currents for a cylinder of moderate radius in order to generate the surface currents for cylinders of any radius above one wavelength. The resulting currents produce total fields with a dynamic range of over 85 dB.

In Chapter 5 the induced surface currents from the right circular cylinder were applied locally, in a standard fashion to approximate the currents induced on a general convex surface. To validate the method on a non-circular cylinder results were first generated for an elliptical cylinder using the macromodeled currents and compared to those generated with a Method of Moments (MoM) code, showing good agreement for all cases. Results from the macromodel when applied to a parabolic surface were then generated and compared to results from knife-edge diffraction. As expected the knife-edge results degraded in the shadow region and as the parabolic surface became less narrow in width.

6.3 Future Work

The propagation problem is an open ended one and it is an understatement to say that there is still a significant amount of research to be pursued. There are several things that still need to be addressed in further development of the models described in this thesis and that will be discussed in the sections that follow. It it appropriate beforehand however to discuss recommendations for future work in terms of the overall context of the propagation

problem. Having developed a basis for an overall propagation model both in this thesis and in the work of other students involved in the project the next logical step in the process is to address the issues of integration of the canonical geometries into a coherent propagation model, including the statistical nature of the propagation environment and relevant interactions between the individual models. A parallel effort should include the integration of a remote sensing satellite data base to model the physical environment within the overall propagation scenario. Currently available remote sensing databases include all relevant parameters including the topography of the terrain (digital elevation maps (DEM)) as well as statistical variations of the propagation environment such as soil moisture, snow cover, vegetation classification, etc. In addition an obvious step would be the investigation and application of these diffraction and scattering models to an urban environment. The urban environment is of significant interest in the prediction of propagation for mobile systems and no techniques developed to date address the relevant issues inherent in an urban environment. Finally and as should be obvious validation of the propagation model by comparison with measured data should be pursued.

6.3.1   Future Work: Fields of a Dipole Above an Impedance Surface

To complete the model for the fields of a small dipole above an impedance surface several issues can be investigated. The current model applies stationary phase techniques to evaluate the field integrals and because of this approximation the dipole must be distant from the impedance transition. A more rigorous evaluation of the field integrals can be examined which allows arbitrary placement of both the dipole and observation, while maintaining the computational efficiency required. The perturbation method applied to calculate scattering from a general impedance transition can determine the scattered fields for any transition for which the Fourier transform exists. As an additional investigation other types of transitions can be investigated including a swamp/dry land transition or a small trough or depression in the terrain.

6.3.2 Future Work: Diffraction From Convex Surfaces

The macromodel developed in Chapters 4 and 5 is for the case of a PEC surface when excited by a plane wave and is intended to serve as a basis for determining the effects of natural obstacles on radio wave propagation. There are two obvious extensions to the work that must be developed in order to make the model of practical use. The first is to extend the model to include dipole excitation. An initial step in this extension could be to restrict the dipole location to be distant from the obstacle and thus only one spectral component of the dipole expansion need be accounted for. The second is to extend the macromodel to the case of a general impedance surface. As a significant amount of time was invested into investigating this problem, some further discussion is in order.

It was initially believe that the macromodel for a PEC cylinder could be extended to that of an impedance cylinder in a simple fashion by assuming that the currents on an impedance cylinder could be represented as a perturbation from the PEC case. For the TM case this assumption in fact proved to be true. If each term of the eigenseries for an impedance cylinder is expanded into a Taylor series, for which the lowest order term represents the PEC case it is observed that the convergence properties of the Taylor series improve as cylinder radius increases. If the limiting case of an cylinder of infinite radius is examined and the expressions for the induced surface currents similarly expanded into a Taylor series, it can be shown that the series will always converge, for the TM case. A similar analysis of the eigenseries for the TE case however shows a degradation in the convergence of the the embedded Taylor series for increasing cylinder radius. Again looking at the limiting case of a cylinder of infinite radius it can be shown that, for the TE case, the Taylor series expansion will never converge for incident angles beyond Brewster's angle. This analysis indicates that in fact the approach of representing the impedance currents as a perturbation from the PEC currents is not a valid one and alternate approaches need be investigated.

APPENDICES

Appendix A

Alternate Spectral Domain Representation the Fields of a Small Dipole Above an Impedance Half-Space

In this appendix an alternate spectral domain representation for the electric fields of an infinitesimal electric dipole radiating above a homogeneous, infinite impedance half-space is derived. The geometry of the problem is as shown in Figure A.1. Starting with the the standard spectral domain representation for the fields of a dipole above an impedance half-space (Green's function) an appropriate change of variables is then applied. Application of Bessel identities will result in the final form of the spectral domain representation of the dipole fields.

The standard spectral representation for the fields of a small dipole above an impedance half-space (Green's function), of length l, orientation $\hat{l}$ and carrying current I_0, is given by
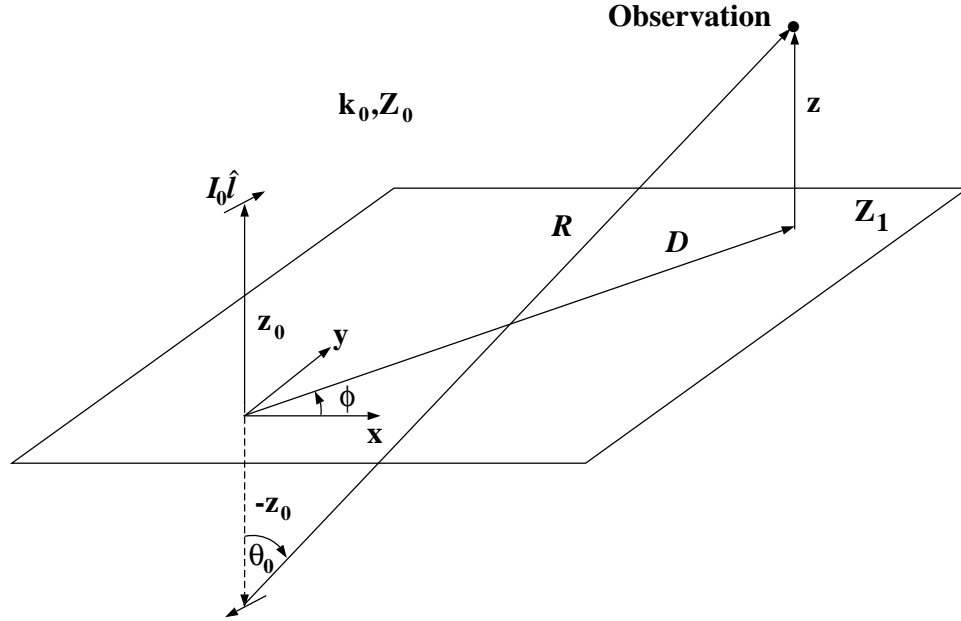
Figure A.1: Problem geometry, dipole above an impedance plane

[34],

$$\mathbf{E}^T(\mathbf{r}, \mathbf{r}_0) = -\frac{iI_0 Z_0 l}{k_0}(\hat{l} \cdot \hat{z})\hat{z}\, \delta(\mathbf{r} - \mathbf{r}_0)$$

$$- \begin{cases} \dfrac{k_0 Z_0 I_0 l}{8\pi^2} \displaystyle\iint\limits_{-\infty}^{+\infty} dk_x\, dk_y\, \dfrac{e^{i(k_x(x-x_0)+k_y(y-y_0))}}{k_z} \\[2mm] \qquad \{\hat{h}(k_z)\,[\Gamma_h(\hat{h}(k_z)\cdot\hat{l})\,e^{ik_z z_0} + (\hat{h}(k_z)\cdot\hat{l})\,e^{-ik_z z_0}] \\[2mm] \qquad + \hat{v}(k_z)\,[\Gamma_v(\hat{v}(-k_z)\cdot\hat{l})\,e^{ik_z z_0} + (\hat{v}(k_z)\cdot\hat{l})\,e^{-ik_z z_0}]\}\,e^{ik_z z} \quad \textbf{for } \mathbf{z > z_0} \\[6mm] \dfrac{k_0 Z_0 I_0 l}{8\pi^2} \displaystyle\iint\limits_{-\infty}^{+\infty} dk_x\, dk_y\, \dfrac{e^{i(k_x(x-x_0)+k_y(y-y_0))}}{k_z} \\[2mm] \qquad \{[\hat{h}(k_z)\Gamma_h\,e^{ik_z z} + \hat{h}(k_z)\,e^{-ik_z z}]\,(\hat{h}(k_z)\cdot\hat{l}) \\[2mm] \qquad + [\hat{v}(k_z)\Gamma_v\,e^{ik_z z} + \hat{v}(-k_z)\,e^{-ik_z z}](\hat{v}(-k_z)\cdot\hat{l})\}\,e^{ik_z z_0} \quad \textbf{for } \mathbf{0 < z < z_0}. \end{cases}$$

$$(A.1)$$

In (A.1) $\mathbf{k} = k_x\hat{x} + k_y\hat{y} + k_z\hat{z}$ with dependent variable, k_z defined as $k_z = \sqrt{k_0^2 - k_x^2 - k_y^2}$, and

144

the branch cut defined as $i = \sqrt{-1}$. The polarization unit vectors $\hat{h}$ and $\hat{v}$ are given by

$$\hat{h}(k_z) = \frac{\mathbf{k} \times \hat{z}}{|\mathbf{k} \times \hat{z}|}, \qquad\qquad \hat{v}(k_z) = \frac{\hat{h}(k_z) \times \mathbf{k}}{k_0}, \qquad\qquad (A.2)$$

and,

$$\hat{h}(-k_z) = \frac{\mathbf{K} \times \hat{z}}{|\mathbf{K} \times \hat{z}|}, \qquad\qquad \hat{v}(-k_z) = \frac{\hat{h}(-k_z) \times \mathbf{K}}{k_0}, \qquad\qquad (A.3)$$

where $\hat{h}$ indicates horizontal polarization (transverse electric (TE) to z) and $\hat{v}$ indicates vertical polarization (transverse magnetic (TM) to z), and $\mathbf{K} = \mathbf{k} - 2(\mathbf{k} \cdot \hat{z})\hat{z} = k_x\hat{x} + k_y\hat{y} - k_z\hat{z}$. The reflection coefficients Γ_h and Γ_v (horizontal and vertical reflection coefficients respectively) in (A.1) are defined as,

$$\Gamma_h = \frac{\eta - k_0/k_z}{\eta + k_0/k_z}, \qquad\qquad \Gamma_v = \frac{-\eta + k_z/k_0}{\eta + k_z/k_0}, \qquad\qquad (A.4)$$

where η is the normalized surface impedance, $\eta = Z_1/Z_0$. The terms containing Γ_h and Γ_v in (A.1) represent the effects of the impedance surface on the total field and are designated as the diffracted fields, with the the other terms representing the direct dipole fields. The direct dipole electric fields are more convieniently evaluated in the spatial domain and are given in dyadic form by

$$\mathbf{E}_d^i(\mathbf{r},\mathbf{r}_0) = \frac{-ik_0 Z_0 I_0 l}{4\pi} \left[\mathbf{I} + \frac{1}{k_0^2} \nabla \nabla \right] \frac{e^{ik_0|\mathbf{r}-\mathbf{r}_0|}}{4\pi} \cdot \hat{l}, \qquad\qquad (A.5)$$

where $\mathbf{r} = \sqrt{x^2 + y^2 + z^2}$ is the distance to the observation point and $\mathbf{r}_0 = \sqrt{x_0^2 + y_0^2 + z_0^2}$ is the distance to the source location. Expanding (A.5) gives the more useful form of the

direct dipole fields or

$$\mathbf{E}^i(\mathbf{r}, \mathbf{r}_0) = i k_0 Z_0 I_0 l \left\{ \left(\frac{3}{k_0^2 R_0^2} - \frac{3i}{k_0 R_0} - 1 \right) \hat{R}_0 (\hat{l} \cdot \hat{R}_0) \right.$$
$$\left. + \left(1 + \frac{i}{k_0 R_0} - \frac{1}{k_0^2 R_0^2} \right) \hat{l} \right\} \frac{e^{i k_0 R_0}}{4 \pi R_0}, \tag{A.6}$$

where $R_0 = |\mathbf{r} - \mathbf{r}_0| = \sqrt{(x - x_0)^2 + (y - y_0)^2 + (z - z_0)^2}$ and $\hat{R}_0 = \frac{\mathbf{r} - \mathbf{r}_0}{|\mathbf{r} - \mathbf{r}_0|}$.

To derive an alternate representation for the diffracted dipole fields in the spectral domain, the standard change of variables is first applied to (A.1),

$$k_x = k_\rho \cos v, \qquad\qquad x - x_0 = D \cos \phi,$$
$$k_y = k_\rho \sin v, \qquad\qquad y - y_0 = D \sin \phi, \tag{A.7}$$

resulting in the following expression for the diffracted dipole fields,

$$\mathbf{E}^d(\mathbf{r}, \mathbf{r}_0) = \frac{k_0 Z_0 I_0 l}{8 \pi^2} \int_0^{2\pi} \int_0^\infty \frac{k_\rho}{k_z} [\Gamma_h (\hat{h} \cdot \hat{l}) \hat{h} + \Gamma_v (\hat{v}(-k_z) \cdot \hat{l}) \hat{v}(k_z)]$$
$$e^{i k_z (z + z_0)} e^{i k_\rho D \cos(v - \phi)} \, dv \, dk_\rho, \tag{A.8}$$

In (A.8), $(\hat{h} \cdot \hat{l}) \hat{h}$ and $(\hat{v}(-k_z) \cdot \hat{l}) \hat{v}(k_z)$ can be rewritten in terms of the new variables as

$$(\hat{h} \cdot \hat{l}) \hat{h} = (l_x \sin^2 v - l_y \sin v \cos v) \hat{x} + (-l_x \sin v \cos v + l_y \cos^2 v) \hat{y}, \tag{A.9}$$

and

$$(\hat{v}(-k_z) \cdot \hat{l}) \hat{v}(k_z) = \frac{1}{k_0^2} \{ -k_z \cos v [k_\rho l_z + k_z (l_x \cos v + l_y \sin v] \hat{x}$$
$$- k_z \sin v [k_\rho l_z + k_z (l_x \cos v + l_y \sin v)] \hat{y} \tag{A.10}$$
$$+ k_\rho [k_\rho l_z + k_z (l_x \cos v + l_y \sin v)] \hat{z} \}.$$

Substituting (A.9) and (A.10) into (A.8) and recognizing that $\cos^2 v = (1 + \cos 2v)/2$, $\sin^2 v = (1 - \cos 2v)/2$, and $\sin v \cos v = (1/2) \sin 2v$ and by applying the following two

146

identities

$$\int\limits_0^{2\pi} \cos(n\nu)\, e^{ik_\rho D\cos(\nu-\phi)}\, d\nu = 2\pi(i)^n \cos(n\phi)\, J_n(k_\rho D), \qquad (A.11)$$

$$\int\limits_0^{2\pi} \sin(n\nu)\, e^{ik_\rho D\cos(\nu-\phi)}\, d\nu = 2\pi(i)^n \sin(n\phi)\, J_n(k_\rho D). \qquad (A.12)$$

the diffracted electric fields in (A.8) can be rewritten as

$$
\begin{aligned}
\mathbf{E}^d(\mathbf{r},\mathbf{r}_0) = \frac{k_0 Z_0 I_0 l}{4\pi} \Bigg\{ &\hat{x} \int\limits_0^\infty \frac{k_\rho}{2k_z} \{\Gamma_h[-l_x(J_2(k_\rho D)\cos 2\phi + J_0(k_\rho D)) - l_y J_2(k_\rho D)\sin 2\phi)] \\
&+\Gamma_v[\frac{2ik_z k_\rho}{k_0^2} l_z \cos\phi J_1(k_\rho D) + \frac{k_z^2}{k_0^2} l_x(J_0(k_\rho D) - J_2(k_\rho D)\cos 2\phi) \\
&-\frac{k_z^2}{k_0^2} l_y J_2(k_\rho D)\sin 2\phi]\}\, e^{ik_z(z+z_0)}\, dk_\rho \\
&+\hat{y} \int\limits_0^\infty \frac{k_\rho}{2k_z} \{\Gamma_h[-l_x J_2(k_\rho D)\sin 2\phi - l_y(J_0(k_\rho D) - J_2(k_\rho D)\cos 2\phi)] \\
&+\Gamma_v[\frac{2ik_z k_\rho}{k_0^2} l_z \sin\phi J_1(k_\rho D) - \frac{k_z^2}{k_0^2} l_x J_2(k_\rho D)\sin 2\phi \\
&+\frac{k_z^2}{k_0^2} l_y(J_0(k_\rho D) + J_2(k_\rho D)\cos 2\phi)]\}\, e^{ik_z(z+z_0)}\, dk_\rho \\
&-\hat{z} \int\limits_0^\infty \frac{k_\rho}{k_z} \Gamma_v[\frac{k_\rho^2}{k_0^2} l_z J_0(k_\rho D) + \frac{ik_z k_\rho}{k_0^2} (l_x \cos\phi \\
&+l_y \sin\phi)J_1(k_\rho D)]\, e^{ik_z(z+z_0)}\, dk_\rho \Bigg\},
\end{aligned}
$$

$$(A.13)$$

(A.13) is an alternate spectral domain representation for the fields of a small dipole above

an impedance half-space and the integrals contained within are Sommerfeld type integrals.

Appendix B

Derivation of 2-D Dyadic Green's Function

In this appendix the spectral representation of the 2-D dyadic Green's function will be derived. The geometry of the problem is as shown in Figure B.1. Observe that θ and ϕ are defined as in standard spherical coordinates with angle β defined from the $\hat{y}$ axis and is used for projection into the $\hat{x} - \hat{z}$ plane. Note that the geometry is not a function of $\hat{y}$ and thus the induced current along $\hat{y}$, and the scattered field, are of the form, $e^{k_y^i y}$ or are in phase with the incident field. The incident field vector $\mathbf{k}^i$ is defined as,

$$\mathbf{k}^i = k_x^i \hat{x} + k_y^i \hat{y} + k_z^i \hat{z} \tag{B.1}$$

where, $k_x^i = k_0 \sin\theta^i \cos\phi^i$, $k_y^i = k_0 \sin\theta^i \sin\phi^i$, and $k_z^i = k_0 \cos\theta^i$.

First we start with the free space dyadic Green's function which has the following form in the spectral domain,

$$\overline{\overline{G}}(\mathbf{r},\mathbf{r}') = -\hat{z}\hat{z}\frac{\delta(r-r')}{k_0^2}$$

$$+ \begin{cases} \frac{i}{8\pi^2} \iint \frac{1}{k_z}[\overline{\overline{I}} - \frac{\mathbf{kk}}{k_0^2}] \, e^{i(k_x(x-x')+k_y(y-y')+k_z(z-z'))} \, dk_x \, dk_y & \textbf{for } \mathbf{z} > \mathbf{z}', \\ \frac{i}{8\pi^2} \iint \frac{1}{k_z}[\overline{\overline{I}} - \frac{\mathbf{KK}}{k_0^2}] \, e^{i(k_x(x-x')+k_y(y-y')-k_z(z-z'))} \, dk_x \, dk_y & \textbf{for } \mathbf{z} < \mathbf{z}', \end{cases} \tag{B.2}$$

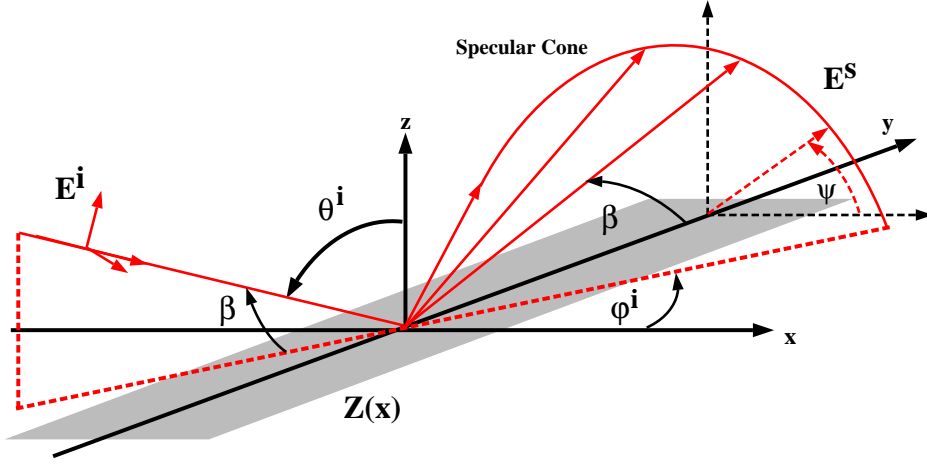where $\mathbf{K} = \mathbf{k} - 2(\mathbf{k}\cdot\hat{z})\hat{z}$.

Figure B.1: Scattering geometry for variable impedance surface.

Since the dependence of the induced currents and fields on y is known ($e^{ik_y^i y}$), the 2-D Green's function can evaluated from (B.2) by integrating out the y dimension to arrive at,

$$
\begin{aligned}
G_{2D}(\rho,\rho') &= -\hat{z}\hat{z}\frac{\delta(\rho-\rho')}{k_0^2}\, e^{ik_y^i y} \\
&+ e^{ik_y^i y}
\begin{cases}
\frac{i}{4\pi} \int \frac{1}{k_z}[\bar{\bar{I}} - \hat{k}\hat{k}]\, e^{i(k_x(x-x')+k_z(z-z'))}\, dk_x & \textbf{for } \mathbf{z > z'}, \\
\frac{i}{4\pi} \int \frac{1}{k_z}[\bar{\bar{I}} - \hat{K}\hat{K}]\, e^{i(k_x(x-x')-k_z(z-z'))}\, dk_x & \textbf{for } \mathbf{z < z'},
\end{cases}
\end{aligned}
\tag{B.3}
$$

where $\rho = x\hat{x} + z\hat{z}$ and $k_z = \sqrt{k_0^2 - k_y^{i\,2} - k_x^2} = \sqrt{k_0^2 \sin^2\beta - k_x^2}$. Here β is defined by $\hat{k}^i \cdot \hat{y} = \cos\beta = \sin\theta^i \sin\phi^i$.

Noting that $[\bar{\bar{I}} - \hat{k}\hat{k}] = \hat{e}\hat{e} + \hat{m}\hat{m}$, the 2-D Green's function in the spectral domain is given in its final form by

$$
G_{2D\perp}(\rho,\rho') = e^{ik_y^i y}\frac{i}{4\pi}\int \frac{1}{k_z}[\hat{e}\hat{e} + \hat{m}\hat{m}]\, e^{i(k_x(x-x')+k_z(z-z'))}\, dk_x,
\tag{B.4}
$$

where $\hat{e}$ and $\hat{m}$ correspond to the TE and TM cases, respectively, and are given by

$$
\hat{e} = \hat{k} \times \hat{y} \quad \text{and} \quad \hat{m} = \hat{e} \times \hat{k}.
\tag{B.5}
$$

149

Noting that, $\hat{k} = [k_x \hat{x} + k_y \hat{y} + k_z \hat{z}]/k_0$, simplified expressions for $\hat{e}$ and $\hat{m}$ are given by,

$$\hat{e} = \frac{k_x \hat{z} - k_z \hat{x}}{k_0 \sin \beta} \qquad \text{and} \qquad \hat{m} = \frac{\hat{y} - \cos \beta \; \hat{k}}{\sin \beta}. \qquad (B.6)$$

BIBLIOGRAPHY

BIBLIOGRAPHY

[1] J. E. Hipp, "Soil Electromagnetic Parameters as Functions of Frequency, Soil Density, and Soil Moisture," *Proceedings of the IEEE*, vol. 62, no. 1, pp. 98–103, January 1974.

[2] Y. Okumura, E. Ohmori, T. Kawano, and K. Fukuda, "Field Strength and its Variability in VHF and UHF Land Mobile Service," *Rev. Elec. Comm. Lab*, vol. 16, pp. 825, September-October 1968.

[3] A. G. Longley and P. L. Rice, "Prediction of Tropospheric Radio Transmission Loss Over Irregular Terrain, A Computer Method - 1968," Tech. Rep. ERL79-ITS67, ESSA Research Laboratories, Washington, D.C., 1968, US Government Printing Office.

[4] T. B. A. Senior, and J. L. Volakis, *Approximate Boundary Conditions in Electromagnetics*, IEE Press, London, 1995.

[5] F. T. Ulaby, R. K. Moore, and A. K. Fung, *Microwave Remote Sensing, Active and Passive, Vols. I, II, and III*, Artech House, Norwood, MA, 1986.

[6] P. Y. Ufimtsev, "Method of Edge Waves in the Physical Theory of Diffraction," Tech. Rep. Engl. transl. available from Nat. Tech. Inform. Serv., Springfield, VA 22161 ; #AD733203, Sovyetskoye Radio, Moscow, Russia, 1962.

[7] A. Sommerfeld, "Über die Ausbreitung der Wellen in der drahtlosen Telegraphie," *Ann. Physik*, vol. 28, pp. 665–736, 1909.

[8] H. Weyl, "Ausbreitung elektromagnetischer wellen über einem ebenen Leiter," *Ann. Physik*, vol. 60, pp. 481–500, 1919.

[9] A. Sommerfeld, "Über die Ausbreitung der Wellen in der drahtlosen Telegraphie," *Ann. Physik*, vol. 81, pp. 1135–1153, 1926.

[10] B. van der Pol and K. F. Niessen, "Über die Ausbreitung elektromagnetischer Wellen über eine ebene Erde," *Ann. Physik*, vol. 6, pp. 273–294, 1930.

[11] W. H. Wise, "The Grounded Condenser Antenna Radiation Formula," *Proceedings of the I.R.E.*, vol. 19, pp. 1684–1689, September 1931.

[12] K. A. Norton, "The Propagation of Radio Waves over the Surface of the Earth and in the Upper Atmosphere: Part I," *Proceedings of the I.R.E.*, vol. 24, no. 10, pp. 1367–1387, October 1936.

[13] K. A. Norton, "The Propagation of Radio Waves over the Surface of the Earth and in the Upper Atmosphere: Part II," *Proceedings of the I.R.E.*, vol. 25, no. 9, pp. 1203–1236, September 1937.

[14] A. Baños, *Dipole Radiation in the Presence of a Conducting Half-Space*, Pergamon, Oxford, 1966.

[15] L. B. Felsen and N. Marcuvitz, *Radiation and Scattering of Waves*, IEEE Press, Piscataway, NJ, 1994.

[16] J. R. Wait, *Electromagnetic Waves in Stratified Media*, IEEE Press, New York, 1996.

[17] P. Parhami, Y. Rahmat-Samii, and R. Mittra, "An Efficient Approach for Evaluating Sommerfeld Integrals Encountered in the Problem of a Current Element Radiating over Lossy Ground," *IEEE Trans. Antennas Propagat.*, vol. 28, no. 1, pp. 100–104, January 1980.

[18] K. A. Michalski, "On the Efficient Evaluation of Integrals Arising in the Sommerfeld Half-space Problem," *IEE Proceedings, Part H-Microwave, Antennas and Propagat.*, vol. 132, no. 5, pp. 312–318, August 1985.

[19] W. A. Johnson and D. G. Dudley, "Real Axis Integration of Sommerfeld Integrals: Source and Observation Points in Air," *Radio Sci.*, vol. 18, no. 2, pp. 313–324, March-April 1983.

[20] H. G. Booker and P. C. Clemmow, "A Relation Between the Sommerfeld Theory of Radio Wave Propagation Over a Flat Earth and the Theory of Diffraction at a Straight Edge," *IEE Proceedings*, vol. 97, Part III, no. 45, pp. 18–27, January 1950.

[21] B. van der Pol, "Theory of the Reflection of the Light from a Point Source by a Finitely Conducting Flat Mirror: With an Application to Radiotelegraphy," *Physica*, vol. 2, pp. 843–853, 1935.

[22] K. Furutsu, "On the Excitation of the Waves of Proper Solutions," *I.R.E. Trans. Antennas Propagat.*, vol. 7, Special Supplement, pp. 209–218, 1959.

[23] I. V. Lindell and E. Alanen, "Exact Image Theory for the Sommerfeld Half-Space Problem, Part I: Vertical Magnetic Dipole," *IEEE Trans. Antennas Propagat.*, vol. 32, no. 2, pp. 126–133, February 1984.

[24] I. V. Lindell and E. Alanen, "Exact Image Theory for the Sommerfeld Half-Space Problem, Part II: Vertical Electric Dipole," *IEEE Trans. Antennas Propagat.*, vol. 32, no. 8, pp. 841–847, August 1984.

[25] I. V. Lindell and E. Alanen, "Exact Image Theory for the Sommerfeld Half-Space Problem, Part III: General Formulation," *IEEE Trans. Antennas Propagat.*, vol. 32, no. 10, pp. 1027–1032, October 1984.

[26] P. C. Clemmow, "Radio Wave Propagation Over a Flat Earth Across a Boundary Separating Two Different Media," *Phil. Trans. Roy. Soc. London*, vol. 246-A, pp. 1–55, 1953.

[27] G. D. Maliuzhinets, "Excitation, Reflection, and Emission of Surface Waves from a Wedge with Given Face Impedances," *Soviet Phys. Dokl.*, vol. 3, pp. 752–755, 1958.

[28] J. Bazer and S. N. Karp, "Propagation of Plane Electromagnetic Waves Past a Shore-line," *J. Res. (Natl. Bur. Std.)*, vol. D66, pp. 319–334, 1962.

[29] J. R. Wait, "Recent Analytical Investigations of Electromagnetic Ground Wave Propagation over Inhomogeneous Earth Models," *Proceedings of the IEEE*, vol. 62, no. 8, pp. 1061–1072, August 1974.

[30] G. de Jong, "Electromagnetic Wave Propagation over an Inhomogeneous Flat Earth (Two-Dimensional Integral Equation Formulation)," *Radio Sci.*, vol. 10, no. 11, pp. 925–933, November 1975.

[31] R. H. Ott, "RING: An Integral Equation Algorithm for HF-VHF Radio Wave Propagation over Irregular, Inhomogeneous Terrain," *Radio Sci.*, vol. 27, no. 6, pp. 867–882, November-December 1992.

[32] K. Sarabandi, "Scattering from Variable Resistive and Impedance Sheets," *Journal of Electromagnetic Waves and Applications*, vol. 4, no. 9, pp. 865–891, 1990.

[33] M. I. Herman and J. L. Volakis, "High Frequency Scattering from Polygonal Impedance Cylinders and Strips," *IEEE Trans. Antennas Propagat.*, vol. 36, pp. 679–688, 1988.

[34] J. A. Kong, *Electromagnetic Wave Theory*, J. W. Wiley & Sons, New York, 1990.

[35] J. D. Murray, *Asymptotic Analysis*, Springer-Verlag, New York, 1984.

[36] V. A. Borovikov, *Uniform Stationary Phase Method*, The Institution of Electrical Engineers, London, 1994.

[37] P. C. Clemmow, "Some Extensions to the Method of Integration by Steepest Descents," *Quart. Journ. Mech. and Applied Math.*, vol. III, Pt. 2, pp. 241–256, 1950.

[38] J. Boersma and Y. Rahmat-Samii, "Comparison of Two Leading Uniform Theories of Edge Diffraction with the Exact Uniform Asymptotic Solution," *Radio Sci.*, vol. 15, no. 6, pp. 1179–1194, November-December 1980.

[39] R. J. Luebbers, "Finite Conductivity Uniform GTD Versus Knife Edge Diffraction in Prediction of Propagation Path Loss," *IEEE Trans. Antennas Propagat.*, vol. 32, no. 1, pp. 70–76, January 1984.

[40] C. A. Balanis, *Advanced Engineering Electromagnetics*, J. W. Wiley & Sons, New York, 1989.

[41] J. J. Bowman, T. B. A. Senior, and P. L. E. Uslenghi, *Electromagnetic and Acoustic Scattering by Simple Shapes*, Hemisphere, New York, 1969.

[42] J. B. Keller, "Diffraction by a Convex Cylinder," *I.R.E. Trans. Antennas Propagat.*, vol. 4, no. 3, pp. 312–321, July 1956.

[43] P. H. Pathak, "An Asymptotic Analysis of the Scattering of Plane Waves by a Smooth Convex Cylinder," *Radio Sci.*, vol. 14, no. 3, pp. 419–435, May-June 1979.

[44] P. Hussar and R. Albus, "On the Asymptotic Frequency Behavior of Uniform GTD in the Shadow Region of a Smooth Convex Surface," *IEEE Trans. Antennas Propagat.*, vol. 39, no. 12, pp. 1672–1680, December 1991.

[45] V. A. Fock, "The Field of a Plane Wave Near the Surface of a Conducting Body," *J. Phys. USSR.*, vol. X, no. 5, pp. 399–409, 1946.

[46] L. W. Pearson, "A Scheme for Automatic Computation of Fock-type Integrals," *IEEE Trans. Antennas Propagat.*, vol. 35, no. 10, pp. 1111–1118, October 1987.

[47] N. A. Logan, "General Research in Diffraction Theory, Vols. 1 & 2," Tech. Rep. LMSD-288088 & 288089, Lockheed Missiles and Space Division, Sunnyvale, CA, 1959.

[48] R. F. Harrington, *Time-Harmonic Electromagnetic Fields*, McGraw-Hill, New York, 1961.

[49] R. E. Collin, *Antennas and Radiowave Propagation*, McGraw-Hill, New York, 1985.